		/	Formatted: Font: (Asian) English (United Kingdom)
1	Simulating Precipitation-Induced Karst-Stream /		Formatted: Normal, Left, Don't add space between
2	Interactions Using a Coupled Darcy-Brinkman-Stokes	Į	style, Line spacing: Ex
3	ModelInteraction mechanism between the karst aquifer	A	Formatted: Font: (Asian) (United Kingdom)
4	and stream under precipitation infiltration recharge		Formatted: Font: (Asian) (United Kingdom)
5	Fuyun Huang <sup>1</sup> , Yuan Gao <sup>1*</sup> , Zizhao Zhang <sup>1*</sup> , Xiaonong Hu <sup>2</sup> , Xiaoguang Wang <sup>3,4</sup> ,		Formatted: Font: (Asian) (United Kingdom)
			Formatted: Font: (Asian) (United Kingdom)
6	Shengyan Pu <sup>5</sup>		Formatted: Font: (Asian) (United Kingdom)
7	- School of Geology and Mining Engineering, Xinjiang University, Urumqi, Xinjiang 830046, China		Formatted: Font: (Asian) (United Kingdom)
8	22. School of Water Conservancy and Environment, University of Jinan, Jinan, Shandong 250022,		Formatted: Font: (Asian) (United Kingdom)
9	China	$\mathbb{N}$	Formatted: Font: (Asian) (United Kingdom)
10	State Key Laboratory of Oil and Gas Reservoir Geology and Exploitation, Chengdu University of		Formatted: Font: (Asian) (United Kingdom)
11	Technology, Chengdu, Sichuan 610059, China		Formatted: Font: (Asian) (United Kingdom)
12	44. Tianfu Yongxing Laboratory, Chengdu, Sichuan 610059, China		Formatted: Left
13	State Key Laboratory of Geohazard Prevention and Geoenvironment Protection, Chengdu University		Formatted: Font: (Asian) (United Kingdom)
14	of Technology, Chengdu, Sichuan 610059, China		Formatted: Font: (Asian) (United Kingdom)
15	Correspondence to: *Correspondence to Yuan Gao (yuangao_xju@hotmail.com) and Zizhao Zhang		Formatted: Font: (Asian) English (United Kingdom)
			Formatted: Justified
16	(zhangzizhao@xju.edu.cn)		Formatted: Superscript
		$\mathbb{W}$	Formatted: Left
17	<b>1</b>	M	Formatted: Font: (Asian) English (United Kingdom)
18	Abstract. † The variation in seasonal precipitation intensity impacts the dynamic interaction between the		Formatted: Superscript
10			Formatted: Justified
19	karst aquifer and stream. However, the interaction mechanism between the karst aquifer and stream is		Formatted: Superscript Formatted: Left
20	currently still unclear, and characterizing the impact of dynamic saturation process of groundwater in		Formatted: Font: (Asian)
21	karst media on the interaction process remains a challenge. This study provides an in-depth analysis of		English (United Kingdom)  Formatted: Superscript
22	the interaction processes between karst aquifer systems and adjacent streams, along with water-air two-		Formatted: Font: (Asian) English (United Kingdom)
23	phase flow in aquifer media. Multiple water retention models were employed to characterize the soil-		Formatted: Justified
24	water characteristics of porous media and variably saturated groundwater flow. The research reveals that		Formatted: Font: (Asian) English (United Kingdom)
24	water characteristics of porous media and variably saturated groundwater flow. The research reveals that		Formatted
25	rainfall intensity variations significantly influence the interactions between karst aquifer systems and		Formatted: Font: (Asian)
26	streams. These interactive processes become increasingly complex with higher rainfall intensities,	1	Formatted: Line spacing: Formatted: Font: 10 pt,
		1	Formatted: Font: 10 pt
27	involving multi-media collaborative recharge and dynamic interactions, while the contribution	1	Formatted

matted: Font: (Asian) Times New Roman, 17 pt, lish (United Kingdom) matted: Normal, Left, Space Before: 18 pt, 't add space between paragraphs of the same le, Line spacing: Exactly 22 pt matted: Font: (Asian) Times New Roman, English ited Kingdom) matted: Font: (Asian) Times New Roman, English ited Kingdom) matted: Font: (Asian) Times New Roman, English ited Kingdom) matted: Font: (Asian) Times New Roman, English ited Kingdom) matted: Font: (Asian) Times New Roman, English ited Kingdom) matted: Font: ited Kingdom) (Asian) Times New Roman, English matted: Font: (Asian) Times New Roman, English ited Kingdom) matted: Font: (Asian) Times New Roman, English matted: Font: (Asian) Times New Roman, English ited Kingdom) matted: Font: (Asian) Times New Roman, English matted: Left matted: Font: (Asian) Times New Roman, English ited Kingdom) matted: Font: (Asian) Times New Roman, English ited Kingdom) matted: Font: (Asian) Times New Roman, 10 pt, lish (United Kingdom), Superscript matted: Justified matted: Superscript matted: Left matted: Font: (Asian) Times New Roman, 10 pt, lish (United Kingdom), Superscript matted: Superscript matted: Justified matted: Superscript matted: Left matted: Font: (Asian) Times New Roman, 10 pt, lish (United Kingdom), Superscript matted: Superscript matted: Font: (Asian) Times New Roman, 10 pt, lish (United Kingdom) matted: Justified matted: Font: (Asian) Times New Roman, 10 pt, lish (United Kingdom) matted: Font: (Asian) +Body Asian (等线) matted: Line spacing: 1.5 lines matted: Font: 10 pt, English (United Kingdom)

Formatted: Font: 10 pt

<u>...</u>

proportions of different media to streamflow also change accordingly. By comparing the modeling differences and numerical results between CFPv2 and DBS approaches in generalized models, the validity of the DBS model for groundwater modeling was verified. Under consecutive rainfall events, total rainfall intensity plays a crucial role in hydrological process variations of adjacent streams. Groundwater stored in porous media of karst systems during the first rainfall event was found to influence stream water levels during subsequent rainfall events, while conduit storage exhibited minimal impact. Multi-level conduit configurations under specific conditions, particularly during intense rainfall, can significantly affect hydrological processes in both streams and karst conduits. Uncertainty analysis demonstrates that conduit geometry, diameter, epikarst permeability, and porosity differentially influence hydrological processes in karst aquifer systems. Variations in these parameters induce corresponding changes in peak flow rates, peak timing of stream and karst spring discharges, as well as redistribution of discharge contributions among different media, ultimately affecting the overall hydrological dynamics of the coupled karst aquifer-stream system. To delve into the impacts of varying precipitation intensities, different water retention models, multi-stage conduit arrangements, and multiple precipitation events on the interaction process between the karst aquifer and stream, this study employs the multiphase Darcy-Brinkman-Stokes equation to analyze the interaction process between the karst aquifer and stream. Additionally, the Phase Indicator Function is used to capture the dynamic changes in saturation levels of various media, and the Brooks-Corey (BC) and van Genuchten-Mualem (VGM) equations are employed to characterize the soil properties of porous media. The results show that as the intensity of precipitation increases, the interaction process between the karst aquifer and stream becomes more complex, involving the synergistic recharge of multi-media and dynamic interactions with the karst aquifer. Discharges in both upper (PM I) and lower (PM II) porous media rise with precipitation intensity, but PM II shows a more significant increase and earlier peak discharge. Secondly, during the middle to late stages of precipitation, the discharge predicted by the BC model exceeds that of the VGM model. The multi-stage conduit arrangement significantly affects stream and karst conduit hydrology during heavy precipitation but has less impact on other media. Finally, multiple precipitation events with different intensities could affect the ease of recharge from media in different strata of the karst aquifer. The Darcy-Brinkman-Stokes model can effectively simulate the interaction process between the karst aquifer and stream under

28

29

30

31

32

33

34

35

36

37

38

39

40

41

42

43

44

45

46 47

48

49

50

51

52

53

54

the influence of precipitation. It can accurately depict the two-phase interactive flow between various media controlled by the dynamic saturation process, and reveal the dynamic interaction process between karst aquifers affected by the epikarst, sinkholes, and conduits under infiltration recharge and stream. Meanwhile, it can precisely explain the processes of infiltration, overflow, and recession.

Keywords: the karst aquifer and stream; precipitation recharge; two-phase flow; Darcy-Brinkman-

61 Stokes equation; interaction mechanism

1 Introduction

Karst aquifer is not only a repository of substantial freshwater resources (Li et al., 2017; Ford & Williams, 2007; Sivelle et al., 2021), but also provides drinking water for 10% to 25% of the global population (Longenecker et al., 2017; Goldscheider et al., 2020; Mahler et al., 2021). However, karst-developed areas feature intricate pore structures and fractures (Kuniansky, 2016), leading to pronounced heterogeneity and anisotropy in the movement and storage of water within them (Zhang et al., 2020). In particular, the complex coupled flow involving various flow paths such as karst conduits, sinkholes, and epikarst, along with porous media, further intensifies the nonlinear recharge and discharge processes and the formation of preferential flow paths in the karst aquifer. With seasonal variations in precipitation intensity, the heterogeneity of the groundwater flow field is further exacerbated, and water levels in the karst aquifer and stream fluctuate, leading to complex interactions between the aquifer and stream under varying precipitation intensities is crucial for assessing the storage of water resources in karst regions (Gao et al., 2021; Guo and Jiang, 2020).

The interaction process between the karst aquifer and stream is significantly influenced by karst media. In epikarst where the soil layer is shallow and dissolution weathering is pronounced, most precipitation can directly recharge the karst aquifer (Lee and Krothe, 2001; OLello et al., 2018). Karst conduits and sinkholes are important media involved in karst hydrological cycle. As rapid discharge

Formatted: b1

Formatted: Font: (Asian) Times New Roman, Font color: Black, English (United Kingdom), Kern at 三号

Formatted: b1, No bullets or numbering

Formatted: Font: 10 pt

Formatted: Line spacing: 1.5 lines

Formatted: Indent: First line: 2 ch, Line spacing: 1.5 lines

channels, the size, connectivity, and distribution of karst conduits have a significant impact on karst hydrological processes (Duran et al., 2020; Bittner et al., 2020). Surface water collected into sinkholes can directly recharge the karst aquifer (Bianchini et al., 2022), thereby regulating the water level of the aquifer and the discharge volume to the stream, which is influenced by precipitation intensity, size and distribution of sinkhole.—.\_The permeability of sinkholes and conduits typically exhibits multilevel characteristics and varies with scale (Halihan et al., 1999), meaning there are strata structures with different permeabilities, which complicates the flow of water within the karst aquifer and increases the catchment area. Therefore, the recharge items to the stream adjacent to the karst aquifer usually include direct precipitation recharge, lateral runoff from the epikarst, discharge from karst springs, and recharge through porous media base flow.

Numerical methods are commonly employed as effective means to accurately simulate karst groundwater movement and assess karst groundwater resources. Shoemaker et al. (2008) proposed a method that discretely embeds conduits, connected by nodes, into the porous media grid (MODFLOW-CFP). This method not only evaluates the water resources of the entire karst aquifer but also considers the geometric shape and distribution of karst conduits on the hydrological processes. Moreover, this methodology has been extensively applied worldwide for estimating karst groundwater flow and water resources (Chang et al., 2015; Qiu et al., 2019; Kavousi et al., 2020; Gao et al., 2020, 2024), as well as in integrated modeling studies coupling SWAT with MODFLOW to investigate groundwater-surface water interactions (Fiorese et al., 2025; Yifru et al., 2024). While MODFLOW-CFP provides robust capabilities for regional-scale karst groundwater simulations, it currently supports only single-phase groundwater flow modeling. Estimations of karst groundwater movement and storage worldwide rely on this method (Kavousi et al., 2020; Qiu et al., 2019; Gao et al., 2020, 2024). Although MODFLOW-CFP is relatively comprehensive for regional karst groundwater simulation studies, the current version of MODFLOW-CFP only supports modeling single-phase groundwater flow.

The interaction process between the karst aquifer and stream is also regulated by the dynamic saturation process within the aquifer. The degree of dynamic saturation in different media determines the path and velocity of water flow. Unsaturated aquifers gradually saturate the underlying aquifers under

the influence of gravity, while saturated underlying aquifers can cause water to overflow (Worthington, 1991; Huang et al., 2024). In addition, the dynamic saturation processes within the karst aquifer are regulated by factors such as seasonal water level fluctuations, the infiltration and flow of groundwater, and the periodic filling and draining of karst conduits (Huang et al., 2024).it is necessary to couple seepage (porous media) with free flow (conduits and stream) and to describe the dynamic saturation process of the karst aquifer. The Hydrus simulation method based on the Richards equation is capable of simulating variably saturated flow (Dam and Feddes, 2000). However, this approach lacks a built-in conduit flow solution scheme, making it difficult to adequately address the coupling requirements between rapid conduit flow and porous media seepage in karst areas.

Constructing an interaction model between the karst aquifer system and the stream under rainfall event-driven conditions requires coupling free flow and seepage processes while simultaneously supporting two-phase variably saturated flow. (1) The Navier-Stokes (N-S) equations combined with the Darcy equation can effectively couple free flow and seepage processes (Soulaine and Tchelepi, 2016; Carrillo et al., 2020). This—ean be achieved by using the Navier Stokes (N-S) equations to couple free

supporting two-phase variably saturated flow. (1) The Navier-Stokes (N-S) equations combined with the Darcy equation can effectively couple free flow and seepage processes (Soulaine and Tchelepi, 2016; Carrillo et al., 2020). This—can be achieved by using the Navier Stokes (N-S) equations to couple free flow with seepage through additional source terms (Soulaine and Tchelepi, 2016; Carrillo et al., 2020). (2) The Phase Indicator Function for two-phase flow, combined with the phase transition method, can effectively describe the variable saturation process within the karst aquifer (Huang et al., 2024; Zhai et al., 2024). The Darcy-Brinkman-Stokes equations have been utilized to couple seepage flow and free flow (Huang et al., 2024; Nillama et al., 2022; Carrillo et al., 2020). Lu et al. (2023) analyzed a model that integrates fast discharge channels in fractures and conduits with slow seepage in porous media. The results demonstrate that the Darcy-Brinkman-Stokes equations can effectively describe two-phase flow in karst aquifers, and Soulaine (2024) proposed that mixed-scale models based on the Darcy-Brinkman-Stokes equations have strong potential for simulating coupled processes in porous systems.

The karst aquifer are typically accompanied by turbulent flow. Reimann et al. (2011) conducted thorough research on turbulent flow in the karst aquifer. To reflect the dissipation of turbulent processes throughout the system, the N-S and Darcy-Brinkman-Stokes equations can be studied using the Reynolds Averaged Network System (RANS) method, where the k-ε turbulence model effectively characterizes turbulent flows in porous media, as demonstrated by del Jesus et al. (2012). The RANS method has been

progressively refined for evaluating turbulent flow in both free-flow regions and porous media (Huang et al., 2024; Zhai et al., 2024; Higuera et al., 2014).

138

139

140

141

142

143

144

145

146

147

148

149

150

151

152

153

154

155

156

157

158

159

160

161

162

163

164

165

This study aims to employ a two-phase variably saturated model capable of coupling free flow and seepage flow to reveal the interaction mechanisms between the karst aquifer system and adjacent stream under rainfall infiltration recharge-driven conditions. Specifically, it focuses on further investigating how groundwater saturation variations in different media (e.g., conduits, fractures, matrix) of the karst aquifer system influence inter-media interactions. This research addresses the gap in existing studies where current numerical methods struggle to accurately characterize the collaborative recharge processes among various media within karst aquifer systems. Currently, the interaction mechanism between the karst aquifer and stream during precipitation infiltration remains unclear, particularly how varying saturation levels in different karst media affect this interaction. Additionally, existing numerical methods fall short in accurately depicting the combined recharge processes across these diverse media within the karst aquifer. To better understand the interaction mechanisms between the karst aquifer and stream during precipitation infiltration, this This study employs the Darcy-Brinkman-Stokes equations to model the coupled processes of seepage in porous media and free flow in karst conduit and stream. The Brooks-Corey (BC) and van Genuchten-Mualem (VGM) models are used to characterize the unsaturated seepage in karst media. The Volume of Fluid (VOF) method is applied to monitor the dynamic changes in aquifer saturation. This research elucidates how saturation dynamics in different karst media impact the coordinated recharge among media during precipitation infiltration, and examines the evolving interaction between the karst aquifer and stream under such recharge conditions. Given the complexity of the interaction mechanism between the karst aquifer and stream, this study specifically investigates the impact of four factors on the interaction mechanism: (1) changes in precipitation intensity, (2) different water retention models, (3) multi-stage conduit arrangements, and (4) parameter sensitivity analysis multiple precipitation events. The research results can further reveal the interaction mechanisms between karst systems and adjacent streams under rainfall infiltration recharge, and provide an in-depth discussion on the impacts of rapid seepage, overflow, and sudden changes in spring discharge on flood control and overflow management along the stream. This study offers a scientific basis for accurately and rationally assessing karst water resources. This study elucidates the interaction mechanisms between

2 Materials and methods

166 167

168

169

170

171

172

173

174

175

176

177

178

179

180

181

182

183

184

185

186

To quantitatively characterize the interaction processes between karst aquifer systems and adjacent streams, as well as the groundwater flow through various media within karst aquifers, the Darcy-Brinkman-Stokes (DBS) method was employed to couple seepage and free flow. The Volume of Fluid (VOF) method was applied to characterize water-air two-phase flow in heterogeneous media, while different water retention models were implemented to describe unsaturated flow processes in karst groundwater systems. The study examines the interaction between karst aquifer and stream, as well as groundwater flow through various karst media, involving the coupling of seepage and free flow proc Therefore, the Darcy-Brinkman-Stokes equations are adopted as the governing equations to describe the groundwater flow between the karst aquifer and stream, as well as within the karst media. The VOF phase transition method is applied to depict the two-phase flow of water and air in the media, and different water retention models are employed to characterize the unsaturated flow process of karst groundwater.

2.1 Mathematical model for simulating interaction process

and free flow in conduit and stream.

The Darcy-Brinkman-Stokes equations are utilized to couple seepage flow in porous media with free flow in conduit and stream (Carrillo et al., 2020; Huang et al., 2024; Soulaine, 2024; Lu et al., 2023). The two phase flow is captured using a phase indicator function. Additionally, the k-c turbulence model

$$\frac{\partial \rho \alpha_t}{\partial t} + \nabla \cdot (\alpha_t v_t) + \nabla \cdot (\varphi \alpha_t \alpha_g v_{rt}) = 0 \tag{2}$$

Formatted: Font: (Asian) Times New Roman, 10 pt, Font color: Black, English (United Kingdom), Kern at 三号

Formatted: Normal, Level 1, Space Before: 24 pt, After: 12 pt, No bullets or numbering, Keep with next

Formatted: Font: 10 pt

Formatted: Indent: First line: 2 ch, Line spacing: 1.5 lines

$$\frac{\frac{1}{\varphi}\left((1+c)\frac{\partial\rho\nu_{\ell}}{\partial t} + \nabla\cdot\left(\frac{\rho}{\varphi}\nu_{\ell}\nu_{\ell}\right)\right) = \\
-\nabla p^{*} + \rho g \cdot X + \nabla\cdot\left(\mu_{eff}(\nabla\nu_{\ell} + \nabla\nu_{\ell}^{T})\right) - \mu_{eff}k^{-1}\nu_{\ell} + F_{e}.$$
(3)

where t denotes the calculation time [s] and  $\varphi$  the porosity;  $\alpha_t = \frac{\nu_t}{\nu_g + \nu_t}$  is the aqueous phase saturation,  $\alpha_g = \frac{\nu_g}{\nu_g + \nu_t}$  is the gas phase saturation, and  $V_g$  and  $V_t$  are the gas phase and the aqueous phase volumes, respectively;  $v_t$  is the fluid flow rate [m/s];  $v_{rt}$  is the relative velocity between groundwater and air [m/s];  $\mu_{eff}$  is the effective viscosity that It can be defined as  $\mu_{eff}$ ,  $\mu$  is the viscosity  $[m^2/s]$ ,  $\mu = \alpha_g \mu_g + \alpha_t \mu_t$ , and  $\mu_g$  and  $\mu_t$  are the viscosity of the gas and liquid phases, respectively;  $v_{turb}$  is the turbulent kinetic viscosity;  $\rho$  represents the average density of groundwater and air;  $p^*$  is pressure [pa]; g is the gravitational acceleration, 9.81  $[m^2/s]$ ; k is the permeability  $[m^2]$ ; and  $F_c$  is the surface tension.

197 The eddy viscosity is expressed as

$$\frac{\mu_{\ell} - \rho C_{\mu} \frac{k^2}{\varepsilon}}{(4)}$$

where k represents the turbulent kinetic energy, s is the dissipation rate of turbulent kinetic energy, and  $C_{\#}$  is a constant, equal to 0.09.

Phase Indicator Function can be expressed as:

$$\alpha_{i} = \begin{cases} 1 & \text{water} \\ 0 < \alpha < 1 & \text{two-phase zone} \\ 0 & \text{air} \end{cases}$$
 (5)

where  $\alpha_t$  represents the saturation of groundwater. Relative permeability is key to describing the migration of groundwater and gas (Kuang and Jiao, 2011). In relative permeability model for two-phase

flow, the effective saturation of the aqueous phase,  $\alpha_{t,e}$ , is given by:

$$\alpha_{l,e} = \frac{\alpha_l - \alpha_{l,e}}{1 - \alpha_{g,e} - \alpha_{l,e}} \tag{6}$$

where,  $\alpha_{t,r}$  and  $\alpha_{g,r}$  are the residual saturations of water and air, respectively. In the Brooks and Corey

(BC) model, the expression for the relative permeability  $k_r$  is given by (Brooks and Corey et al., 1964):

$$k_{r,q} = \left(1 - \alpha_{l,e}\right)^{0.5} \left(1 - \alpha_{l,e}^{1/m}\right)^{2m} \tag{7}$$

$$k_{\frac{r}{r,l}} = \alpha_{\frac{l}{l,e}}^{0.5} \left(1 - \left(1 - \alpha_{\frac{l}{l,e}}^{1/m}\right)^{m}\right)^{\frac{2}{r}}$$
 (8)

where, m is a dimensionless parameter that is determined based on the characteristics of the porous media

within the karst aquifer. The expression for relative permeability in the van Genuchten Mualem (VGM)

213 model (Parker et al., 1987) is defined as follows:

212

220

$$k_{r,g} = (1 - \alpha_{l,e})^{0.5} (1 - \alpha_{l,e}^{1/m})^{2m}$$
 (9)

$$k_{r,l} = \alpha_{l,e}^{0.5} \left(1 - \left(1 - \alpha_{l,e}^{1/m}\right)^{m}\right)^{2} \tag{10}$$

In the free and porous regions, the source term  $\mu k^{-1}$  in the Darcy-Brinkman-Stokes equation varies

in form and can be expressed as (Soulaine, 2024; Huang et al., 2024):

$$218 \qquad \mu_{eff}k^{-1} = \rho v_{turb}k^{-1} + \begin{cases} 0, & \text{free region} \\ k_{tt}^{-1} \left(\frac{k_{r,t}}{\mu_t} + \frac{k_{r,\theta}}{\mu_{\theta}}\right)^{-1}, & \text{porous region} \end{cases}$$
(11)

The permeability coefficient  $k_0$ , which is determined by the geometric structure of the porous

medium, controls both free flow and seepage. When permeability is high, the governing equation

221 (Equation 3) simplifies to the Navier-Stokes equation (Equation 12). Conversely, when permeability is

low, the equation reduces to Darcy's law (Equation 13).

223 
$$\frac{(1+\varepsilon)\frac{\partial\rho\nu_{\varepsilon}}{\partial t} + \nabla \cdot (\rho\nu_{\varepsilon}\nu_{\varepsilon}) =}{-\nabla\rho^{*} + \rho g \cdot X + \nabla \cdot \left(\mu_{eff}(\nabla\nu_{\varepsilon} + \nabla\nu_{\varepsilon}^{T})\right) + F_{\varepsilon}\text{,if }\varphi = 1.} \tag{12}$$

224 
$$0 = -\nabla p^+ + \rho g \cdot X - \mu_{eff} k^{-1} v_{\epsilon} + F_{e} \text{ if } \varphi \in ]0,1[.$$
 (13)

Meanwhile, the surface tension  $F_{\varepsilon}$  and density  $\rho$  in the free-flow and porous media regions are as follows

226 (Huang et al., 2024):

227 
$$F_{e} = \begin{cases} -\frac{\sigma}{\varphi} \nabla \cdot \left(\frac{V\alpha_{t}}{|\nabla \alpha_{t}|}\right) \nabla \alpha_{t}, & \text{free region} \\ \frac{k_{e}}{|\nabla \alpha_{t}|} \frac{k_$$

$$\rho = \begin{cases} \rho_{t}\alpha_{t} + \rho_{g}\alpha_{g}, & \text{free regions} \\ \left(\rho_{g}\frac{k_{rg}}{\mu_{g}} + \rho_{t}\frac{k_{rg}}{\mu_{t}}\right) \\ k_{\theta}\frac{k_{rg}}{\mu_{g}} + \frac{k_{rg}}{\mu_{g}}, & \text{porous regions} \end{cases}$$
(15)

where  $\sigma$  is the interfacial tension [N/m],  $p_{\sigma}$  is capillary pressure [pa].

$$k_{\vec{r},g} = \left(1 - \alpha_{t,e}\right)^{0.5} \left(1 - \alpha_{t,e}^{\frac{1}{m}}\right)^{2m} \tag{16}$$

Numerical modeling

## 2.2-1 Numerical modelling

The numerical model is developed according to the conceptual model of the karst aquifer adjacents to a stream, as depicted in Fig. 1. The model construction incorporates distinct rainfall intensities and temporal rainfall patterns (Figure 1(a)-(b)), while explicitly accounting for characteristic karst geomorphological features including sinkholes, epikarst, and karst conduits. The model incorporates the distinctive features of karst regions, including sinkholes, epikarst, and karst conduit (Fig. 1). The karst conduit is connected to the epikarst through a sinkhole. The outcrop of the karst spring is located at the end of the karst conduit, directly leading to the stream.

Recharge Pathways in a Single Recharge Event: During a single recharge event, precipitation follows two main pathways: a portion directly recharges the adjacent stream, while another portion infiltrates into the epikarst zone (shallow karst system). A fraction of the water stored in the epikarst zone discharges laterally to the stream, while the remaining water disperses vertically through porous media to recharge the deeper porous aquifer. The residual water in the epikarst zone further recharges the karst conduit system via sinkhole point infiltration (Figure 1(a.1)).

Conduit Network-Matrix Interaction: Under moderate recharge events, conduits receive water from both sinkhole point recharge and porous media recharge, rapidly transporting it to discharge at karst

Formatted: b2

Formatted: Font: 10 pt

Formatted: Indent: First line: 2 ch, Line

spacing: 1.5 lines

springs. During intense precipitation events, water in the conduits may temporarily reverse flow to recharge the porous media before returning to the conduits (Bailly-Comte et al., 2010).

249

250

251

252

253

254

255

256

257

258

259

260

261

262

263

264

265

266

267

268

269

270

271

272

273

274

275

276

Karst Aquifer-Stream Interaction: Lateral recharge from the porous aquifer to the stream requires prior vertical dispersion recharge from the overlying epikarst zone. During a single precipitation event, direct lateral recharge from the epikarst zone and rapid discharge of groundwater from karst springs to the stream cause an earlier stream stage rise. As the stream stage gradually increases, the stream begins to recharge the deeper porous media of the karst aquifer (Figure 1(a.1)). Due to the high flow velocity of the stream, its stage declines rapidly, allowing groundwater in the deeper porous media to discharge back into the stream (Figure 1(a.2)).

The precipitation influences the dynamic variation process of saturation within porous media In the karst aquifer, the saturation levels within the porous media are dynamically altered by precipitation, and the water levels in both the karst conduit and the stream experience substantial fluctuations. As a result, the interaction between the porous media and the stream displays a clear multi-scale characteristic. From a hydrological perspective of the watershed, the recharge and discharge processes of karst conduit are controlled by the saturation degree of the surrounding porous media and the water level within the conduit themselves. Based on spatial relationships, the area between the karst conduit and the epikarst is divided into Porous Medium I (PM I) above the conduit, Porous Medium II (PM II) on the sides, and Porous Medium III (PM III) directly below the conduit(Figure 1(a.1)). Based on the aforementioned dynamic interaction processes between the karst aquifer system and the adjacent stream, this study constructs the DBS numerical model and employs the CFPv2 (Shoemaker et al., 2008; Giese et al., 2018) to simulate groundwater flow. Through analyses of precipitation intensity variations, multiple precipitation events, different water retention models, multi-level permeability configurations, and parameter sensitivity analyses under repeated rainfall influences, the interaction mechanisms between the karst aquifer system and the stream are elucidated. During a single precipitation event, some of the rainfall directly replenishes the stream, while the remainder percolates down to recharge the karst aquifer. The infiltration recharge consists of two processes: (1) infiltration recharge to the epikarst, and (2) downward infiltration recharge to the aquifer through sinkhole and porous media. These two processes sequentially recharge the stream: groundwater discharges laterally through the epikarst to the stream; precipitation rapidly recharges the connected karst conduit through the sinkhole and recharges to the stream through the karst spring, while groundwater in the aquifer also discharges laterally to the stream. Compared to PM I, groundwater in the epikarst recharges the stream at a faster rate, causing the water level of stream to rise and subsequently recharging PM I and PM II. As the water level of stream gradually rises, the stream will recharge the karst aquifer. Due to the rapid flow velocity of the stream, the water level drops, allowing groundwater in the lower porous media to discharge back into the stream. This study constructs a numerical model based on the dynamic interaction process between the karst aquifer and stream, revealing the interaction mechanism between the karst aquifer and stream under the influence of precipitation intensity changes, different water retention models, multi-level permeability arrangements, and multiple precipitation events.

The upper boundary of the strata is a transient natural precipitation boundary condition. The boundary condition for precipitation infiltration recharge is adopted using the following equation (Huang et al., 2024):

$$I(t) = \frac{b}{\sqrt{2a-2}} \sum_{\ell} e^{-\frac{\left(\frac{t_{\ell}-\mu}{a}\right)^2}{2\sigma^2}} \tag{17}$$

where  $t_i$  represents the time of the *i*th precipitation event, and I(t) represents the total precipitation at that moment. According to Chang et al. (2015),  $\mu$ ,  $\sigma^2$  and a are set as constants (90, 1.5 and 20, respectively). During precipitation infiltration recharge, changes in precipitation intensity are adjusted via the dimensionless parameter b.

Some researchers have positioned the karst conduit at the bottom of the model grid (Kavousi et al., 2020; Li et al., 2023). This study employs a programming approach to dynamically generate the sinkhole and conduit grids, enabling the creation of conduit and sinkhole of varying diameters at any position within the model by adjusting parameters such as conduit radius and center coordinates. This enhances

the adaptability and practicality of the model.

300

318

319

320

321

301 Figure 2 illustrates the discretization scheme adopted by this study, clearly showing the division and 302 distribution of grids in each region. Based on the thickness of the epikarst layer and the position of the 303 am, except for the stream, sinkhole, epikarst, and karst conduit, and the remaining areas are divided 304 into porous media regions, and the grids in the free-flow regions are further refined. Given that the flow 305 in the conduit, sinkhole, and stream is free-flowing, fine grids are required to capture the microscopic 306 changes in water levels and interfaces, so the grids in these regions are locally refined. In the porous 307 media, groundwater flows in a seepage manner, with its velocity decreasing with the increase in distance 308 from the discharge end, forming a funnel-shaped pressure drop flow characteristic. Thus, a grid spacing 309 approach with gradual increments in the porous media regions is employed. The edge grids are designed 310 to be twice as long as those near the conduit. This method ensures precise simulation of flow near the 311 discharge end while significantly reducing computational resource usage in distant areas. Given the 312 olution effects near the sinkholes and epikarst, the permeability of the porous media in the karst aquifer decreases from the interior to the exterior, and it is assigned in a graded manner. The values of 313 314 the model parameters are listed in Table 1. 315 2.2 DBS model 316 2.2.1 Two-Phase Flow Parameter Definition 317 Assuming that gas and liquid fill the solid pore space, porosity is defined to characterize the

Formatted: b3, Indent: First line: 0 cm Formatted: Font: 10 pt Formatted: Indent: First line: 2 ch, Line spacing: 1.5 lines Formatted: Font: 10 pt Formatted: Font: (Default) Times New Roman, 10 Formatted: Space Before: 6 pt, After: 6 pt, Line spacing: 1.5 lines Formatted: Font: 10 pt Formatted: Indent: First line: 2 ch, Line spacing: 1.5 lines Formatted: Font: 10 pt Formatted: Font: 10 pt Formatted: Font: 10 pt

Formatted: b2

(16)

13

correspond to the volumes of the liquid phase (water) and gas phase (air), respectively [m<sup>3</sup>].

In this context,  $\varphi$  represents porosity, V denotes the total volume of the unit [m<sup>3</sup>], while  $V_L$  and  $V_{\varphi}$ 

percentage of the gas and liquid phases occupying the total pore space.

322	Hirt and Nichols (1981) introduced the Volume of Fluid (VOF) method, which employs an			
323	additional governing equation to capture fluid motion at free surfaces. Furthermore, the saturation of			
324	each phase in the fluid is defined as $\alpha_{ie}$ where:		Formatted	
325	Liquid phase saturation: $\alpha_l = \frac{v_l}{V_{ab}V_{ab}}$	/	Formatted	
326	Gas phase saturation: $\alpha_g = \frac{v_g}{v_{ab}v_{ab}}$		Formatted	
327	Here, the subscripts $l$ and $g$ denote water and air, respectively. Thus, the spatial distribution of water			
328	and gas within the porous medium is characterized by porosity $\varphi$ and phase saturation $\varphi_{ii}$		Formatted	
329	$\varphi = \begin{cases} 1 & \text{free regions} \\ 0 < \alpha < 1 & \text{porous regions} \\ 0 & \text{solid regions} \end{cases} $ (17)*		Formatted Formatted	
	solid regions	<b>/</b> <	Formatted: Space Before: 6 pt, After: 6 p Line spacing: 1.5 lines	ot,
330	$\alpha_l = \begin{cases} 1 & \text{water} \\ 0 < \alpha < 1 & \text{two-phase zone} \end{cases} $ (18)	/	Formatted	
221	and which is a state of the sta		Formatted: Font: 10 pt	
331	The average fluid density $\rho[m^3/kg]$ and viscosity $\mu[m^2/s]$ within a grid cell are calculated via		Formatted	
332	saturation-weighted averaging:	1	Formatted	
333	$\rho = \rho_0 \alpha_0 + \rho_1 \alpha_1 \tag{19}$		Formatted: Indent: First line: 2 ch, Line spacing: 1.5 lines	
	R - MANALLY MANA		Formatted	
334	$\mu = \alpha_{\theta} \mu_{\theta} + \alpha_{t} \mu_{t} \tag{20}$		Formatted: Space Before: 6 pt, After: 6 p Line spacing: 1.5 lines	
335	where $\rho_{ch}$ is the gas phase density [m <sup>3</sup> /kg] and $\rho_{L}$ is the liquid phase (water) density [m <sup>3</sup> /kg].		Formatted: Font: 10 pt	
000	where $p_{g_i}$ is the gas phase density [111] / ((g)) and $p_i$ is the right phase (where) density [111] / ((g)):		Formatted	···
336	The transport equation for saturation $a_{in}$ following Rusche (2002), is expressed as:		Formatted	
		1/1	Formatted Formatted	
337	$\frac{\partial \varphi \alpha_l}{\partial t} + \nabla \cdot (\alpha_l v_t) + \nabla \cdot (\varphi \alpha_l \alpha_g v_{rt}) = 0 \tag{21}$	1/	Formatted	
220			Formatted: Indent: First line: 0 ch, Line spacing: 1.5 lines	
338	where: $v_{t,k}$ is the fluid velocity vector $[m/s]$ , $v_{t,k}$ is the relative velocity between the gas and liquid	1	Formatted	
339	phases $[m/s]$ .	$/\!\!/$	Formatted: Indent: First line: 2 ch, Line spacing: 1.5 lines  Formatted	
340	2.2.2 Governing Equations		Formatted: Space Before: 6 pt, After: 6 ptine spacing: 1.5 lines	
241	The state of the s	/ //	Formatted	
341	To precisely describe groundwater flow through porous media in the karst aquifer system and the	1/	Formatted	
342	free-surface flow processes between conduits and the adjacent stream, this study adopts the DBS (Dual-		Formatted: Line spacing: 1.5 lines, No bu or numbering  Formatted: b3, Indent: First line: 0 cm	llets
343	domain Brinkman-Stokes) equations to characterize immiscible and incompressible two-phase flow in		Formatted: Box, indent. First line. O cm	$\longrightarrow$
344	porous media (Nillama et al., 2022; Carrillo et al., 2020; Lu et al., 2023; Huang et al., 2024; Soulaine,	\	Formatted: Indent: First line: 2 ch, Line spacing: 1.5 lines	

345	2024). The DBS model is employed to represent both Darcian flow in porous media and turbulent flow		
346	dynamics during free-surface interactions between conduits and the stream. The governing equations		
2.47			
347	include:		
348	$\nabla \cdot \overline{\nu} = 0$ (22)		Formatted
349	$\frac{\partial \varphi \alpha_l}{\partial t} + \nabla \cdot (\alpha_l \overline{\nu}) + \nabla \cdot (\varphi \alpha_l \alpha_g \overline{\nu_r}) = 0 \tag{23}$		Formatted: Normal, Indent: First line: 0.71 cm, Space Before: 6 pt, After: 6 pt, Line spacing: 1.5 lines
	$\partial t$		Formatted
350	$\frac{1}{\varphi} \left( \frac{\partial \rho \overline{v}}{\partial t} + \nabla \cdot \left( \frac{\rho}{\varphi} \overline{v} \overline{v} \right) \right) = -\nabla \overline{p} + \rho g + \nabla \cdot \left( \frac{\mu}{\varphi} \left( \nabla \overline{v} + \nabla \overline{v}^T \right) \right) + F_c + S_f. \tag{24}$	/	Formatted  Formatted: Space Before: 6 pt, After: 6 pt, Line spacing: 1.5 lines
351	Here, t represents the computational time $[T]$ , $\overline{p}$ is the velocity $[L/T]$ , $\overline{p}_{r}$ is the relative flow rate		Formatted: Font: 10 pt
			Formatted
352	of the gas phase to the liquid phase $[L/T]$ , $\rho$ is the average density of the gas and liquid phases $[M/L^3]$ ,		Formatted
353	$\bar{p}_{\underline{i}}$ is the pressure $[pa]$ , $g$ is is the acceleration due to gravity $(9.81 \ m/s_{\underline{i}}^2)$ , $\mu$ is the viscosity $[L^2/T]$ . $F_{\underline{i}}$ is		Formatted: Normal, Indent: First line: 0.71 cm, Line spacing: 1.5 lines
354	the surface tension, and $S_f$ is the resistance source term.		Formatted
355		/	Formatted
555	Conduit networks in karst aquifer systems are often associated with turbulent flow (Reimann et al.,	//	Formatted ()
356	2011). To resolve turbulence in the DBS (Dual-domain Brinkman-Stokes) equations, the Unsteady	\	Formatted
357	Reynolds-Averaged Navier-Stokes (URANS) framework is required. As demonstrated by del Jesus et al.		
358	(2012), the k-epsilon turbulence model is effective for evaluating turbulent processes within porous		
359	media. Consequently, the k-epsilon-based DBS turbulence governing equations are formulated as follows:		
360	7 0 (25)		Formatted
500	$\nabla \cdot \mathbf{v}_{t, \bullet} = 0 \tag{25}$	~	Formatted: Space Before: 6 pt, After: 6 pt,
261	$\partial \varphi \alpha_{l}$		Line spacing: 1.5 lines
361	$\frac{\partial \varphi \alpha_l}{\partial t} + \nabla \cdot (\alpha_l v_t) + \nabla \cdot (\varphi \alpha_l \alpha_g v_{rt}) = 0 \tag{26}$		Formatted
	$\frac{1}{\varphi}\bigg((1+c)\frac{\partial\rho v_t}{\partial t} + \nabla\cdot \left(\frac{\rho}{\varphi}v_tv_t\right)\bigg) =$	/	Formatted
362	/		Formatted: Font: 10 pt
	$-\nabla p^* + \rho g \cdot X + \nabla \cdot \left(\mu_{eff}(\nabla v_t + \nabla v_t^T)\right) - \mu_{eff}k^{-1}v_t + F_c. \tag{27}$	/ /,	Formatted
			Formatted
363	where, $v_0$ represents the turbulent velocity vector $[L/T]$ , $v_{rt_0}$ is the relative velocity of gas-phase and		Formatted: Normal, Indent: First line: 0.71 cm, Line spacing: 1.5 lines
364	water-phase turbulence $[L/T]$ , and $\mu_{eff}$ is the effective viscosity, which can be defined as $\mu_{eff} = \mu +$		Formatted
265			Formatted
365	$\rho p_{turb}$ where $\mu$ is the dynamic viscosity and $p_{turb}$ is the turbulent kinetic viscosity.	<	Formatted
366	The eddy viscosity is expressed as:		Formatted
			Formatted: Indent: First line: 2 ch, Line spacing: 1.5 lines, Tab stops: Not at 19 ch
367	$\mu_t = \rho C_\mu \frac{k_t^2}{46} \tag{28}$	/	Formatted
	AAA AAAAA		Formatted: Space Before: 6 pt, After: 6 pt, Line spacing: 1.5 lines
	15		

368 where:  $k_{\epsilon}$ : Turbulent kinetic energy per unit mass  $[m_{\epsilon}^2/s_{\epsilon}^2]$ ,  $\varepsilon_{\epsilon}$ : Turbulent dissipation rate per unit Formatted: Font: 10 pt Formatted 369 mass  $[m^2/s^3]$ ,  $C_u$ : Dimensionless constant with a value of 0.09 Formatted Formatted: Font: 10 pt 370 2.2.3 Subdomain Formulation Formatted: Indent: First line: 2 ch, Line spacing: 1.5 lines, No bullets or numbering Formatted 371 For the free-flow region and the porous media region, the source terms in the DBS equations adopt Formatted Formatted: b3, Indent: First line: 372 distinct forms. Specifically, the source term  $\mu k_{\perp}^{-1}$  in the two regions can be expressed as (Soulaine, 2024; Formatted: Font: 10 pt Huang et al., 2024): 373 Formatted: Indent: First line: 2 ch, Line spacing: 1.5 lines Formatted  $\mu_{eff}k^{-1} = \rho \boldsymbol{v}_{turb}k^{-1} + \begin{cases} k_{r,l} & k_{r,g} \\ k_{r,l}^{-1} & k_{r,g} & k_{r,g} \end{cases}$ 374 (29) Formatted porous region Formatted: Space Before: Line spacing: 1.5 lines 6 pt, After: 6 pt, Line spacing: 375 Here,  $k_0$  is the permeability coefficient determined by the pore structure  $[m_1^2]$ . When the Formatted Formatted 376 permeability is extremely high, this term vanishes, and the DBS equations reduce to the Navier-Stokes Formatted: Indent: First line: spacing: 1.5 lines 377 (N-S) equations (Equation 15). Conversely, as permeability decreases, the term  $\mu k_{\perp}^{-1} \overline{\nu}_{\mu}$  becomes Formatted ... 378 dominant compared to other source terms, causing the DBS equations to asymptotically approach the 379 Darcy equation incorporating gravity and surface tension (Equation 16).  $(1+c)\frac{\partial \rho v_t}{\partial t} + \nabla \cdot (\rho v_t v_t) = \\ -\nabla p^* + \rho g \cdot X + \nabla \cdot \left(\mu_{eff}(\nabla v_t + \nabla v_t^T)\right) + F_{c}if\varphi = 1.$ Formatted Formatted: Indent: First line: 2 ch, Space Before: 6 pt, After: 6 pt, Line spacing: 380 (30)lines 381  $0 = -\nabla p^* + \rho g \cdot X - \mu_{eff} k^{-1} v_t + F_{c_t} if \varphi \in ]0,1[.$ Formatted (31)382 Similarly, the surface tension force  $F_{\rho}$  and density  $\rho$  in the two regions can be expressed as (Huang Formatted: Font: 10 pt Formatted 383 et al., 2024): Formatted: Indent: First line: 2 ch, Line spacing: 1.5 lines Formatted ... free region Formatted: Space Before: 6 pt, After: 6 pt, Line spacing: 1.5 lines 384 (32) porous region free regions Formatted ... 385 (33)porous regions Formatted: Font: 10 pt Formatted Formatted 386 Here,  $\sigma$  is the interfacial tension [N/m],  $p_c$  is the capillary pressure [pa], and k Formatted: Indent: First line: 2 ch, Line spacing: 1.5 lines 387 and  $k_{r,h}$  represent the relative permeabilities of the gas phase and liquid phase, respectively. Formatted

388	2.2.4 Relative Permeability Model		Formatted: b3	
			Communication and	
389	Accurate modeling of two-phase flow in porous media is critical in geosciences. Simulating two-		Formatted: Font: 10 pt	
390	phase flow in variably saturated porous media requires precise estimation of the relationship between		Formatted: Indent: First line: 2 ch, Lin spacing: 1.5 lines	ne
391	relative permeability and saturation (Springer et al., 1995).			
392	To characterize the variation in two-phase relative permeability, the effective saturation of the liquid			
393	phase must first be defined. This is expressed as:			
394	$\alpha_{l,e} = \frac{\alpha_l - \alpha_{l,r}}{1 - \alpha_{a_{l,r}} - \alpha_{l,r}} \tag{34}$		Formatted	
	$1 - g_{gr} - g_{jr}$		Formatted: Space Before: 6 pt, After: 6 Line spacing: 1.5 lines	5 pt,
395	where: $\alpha_{l,e}$ denotes the effective water saturation, $\alpha_{l}$ and $\alpha_{l,r}$ represent the water saturation and		Formatted: Font: 10 pt	
396	residual water saturation, respectively, and $\alpha_{a.r.}$ is the residual air saturation.	1	Formatted	
570	residual water saturation, respectively, and $\alpha_{g,r}$ is the residual air saturation.	///	Formatted	
397	Relative permeability is a critical parameter in groundwater and related engineering fields (Kuang		Formatted: Indent: First line: 2 ch, Lin	
398	and Jiao, 2011). The Brooks and Corey (BC) model (Brooks and Corey, 1964) and the van Genuchten		spacing: 1.5 lines  Formatted  Formatted	ie
399	model (van Genuchten, 1980) are widely used as representative relative permeability models. The BC		(.0.11100000	(
400	model establishes a relationship between relative permeability and effective water saturation as follows:			
401	$k = (1 - \alpha_n)^n \tag{25}$		Formatted	
401	$k_{rg} = (1 - \alpha_{l,e})^{n} \tag{35}$	~	Formatted: Indent: First line: 2 ch, Spa	
401 402	$k_{T_{l_{A}}} = \left(1 - \alpha_{l_{A}e}\right)^{n} \tag{35}$ $k_{T_{l_{A}}} = \alpha_{l_{A}e}^{n} \tag{36}$	<<	Formatted: Indent: First line: 2 ch, Spa Before: 6 pt, After: 6 pt, Line spacing lines	
402			Formatted: Indent: First line: 2 ch, Spa Before: 6 pt, After: 6 pt, Line spacing lines  Formatted	
402 403	$k_n$ denotes the relative permeability, where $n$ is a dimensionless coefficient determined by the	×	Formatted: Indent: First line: 2 ch, Spa Before: 6 pt, After: 6 pt, Line spacing lines	
402		×	Formatted: Indent: First line: 2 ch, Spa Before: 6 pt, After: 6 pt, Line spacing lines  Formatted Formatted	
402 403	$k_n$ denotes the relative permeability, where $n$ is a dimensionless coefficient determined by the		Formatted: Indent: First line: 2 ch, Spa Before: 6 pt, After: 6 pt, Line spacing lines  Formatted Formatted	
402 403 404	k <sub>r</sub> denotes the relative permeability, where n is a dimensionless coefficient determined by the properties of the porous medium. The Brooks-Corey (BC) model exhibits a sharp discontinuity at the air		Formatted: Indent: First line: 2 ch, Spa Before: 6 pt, After: 6 pt, Line spacing lines  Formatted Formatted	
402 403 404 405	k <sub>r</sub> denotes the relative permeability, where n is a dimensionless coefficient determined by the properties of the porous medium. The Brooks-Corey (BC) model exhibits a sharp discontinuity at the air entry point, which can lead to poor data fitting, particularly for fine-textured soils (Assouline & Or, 2013).		Formatted: Indent: First line: 2 ch, Spa Before: 6 pt, After: 6 pt, Line spacing lines  Formatted Formatted	
402 403 404 405 406	$k_{\rm E}$ denotes the relative permeability, where $n$ is a dimensionless coefficient determined by the properties of the porous medium. The Brooks-Corey (BC) model exhibits a sharp discontinuity at the air entry point, which can lead to poor data fitting, particularly for fine-textured soils (Assouline & Or, 2013). The van Genuchten (1980) model addresses this limitation. By incorporating the parameter $m = 1$		Formatted: Indent: First line: 2 ch, Spa Before: 6 pt, After: 6 pt, Line spacing lines  Formatted Formatted	
402 403 404 405 406 407	$k_{\rm E}$ denotes the relative permeability, where $n$ is a dimensionless coefficient determined by the properties of the porous medium. The Brooks-Corey (BC) model exhibits a sharp discontinuity at the air entry point, which can lead to poor data fitting, particularly for fine-textured soils (Assouline & Or, 2013). The van Genuchten (1980) model addresses this limitation. By incorporating the parameter $m = 1 - 1/n$ proposed by Mualem (1976), the modified van Genuchten-Mualem (VGM) model (Parker et al., 1987) is formulated as:		Formatted: Indent: First line: 2 ch, Spa Before: 6 pt, After: 6 pt, Line spacing lines  Formatted Formatted	
402 403 404 405 406 407 408	$k_{\rm r}$ denotes the relative permeability, where $n$ is a dimensionless coefficient determined by the properties of the porous medium. The Brooks-Corey (BC) model exhibits a sharp discontinuity at the air entry point, which can lead to poor data fitting, particularly for fine-textured soils (Assouline & Or, 2013). The van Genuchten (1980) model addresses this limitation. By incorporating the parameter $m = 1 - 1/n$ proposed by Mualem (1976), the modified van Genuchten-Mualem (VGM) model (Parker et al., 1987) is formulated as:		Formatted: Indent: First line: 2 ch, Spa Before: 6 pt, After: 6 pt, Line spacing lines  Formatted  Formatted  Formatted: Line spacing: 1.5 lines	1.5
402 403 404 405 406 407 408	$k_{\rm E}$ denotes the relative permeability, where $n$ is a dimensionless coefficient determined by the properties of the porous medium. The Brooks-Corey (BC) model exhibits a sharp discontinuity at the air entry point, which can lead to poor data fitting, particularly for fine-textured soils (Assouline & Or, 2013). The van Genuchten (1980) model addresses this limitation. By incorporating the parameter $m = 1 - 1/n$ proposed by Mualem (1976), the modified van Genuchten-Mualem (VGM) model (Parker et al., 1987) is formulated as:		Formatted: Indent: First line: 2 ch, Spa Before: 6 pt, After: 6 pt, Line spacing lines  Formatted  Formatted: Line spacing: 1.5 lines  Formatted: Line spacing: 2 ch, Spa Formatted: Indent: First line: 2 ch, Spa Formatted: Indent: In	1.5
402 403 404 405 406 407 408	$k_{r,d}$ enotes the relative permeability, where $n$ is a dimensionless coefficient determined by the properties of the porous medium. The Brooks-Corey (BC) model exhibits a sharp discontinuity at the air entry point, which can lead to poor data fitting, particularly for fine-textured soils (Assouline & Or, 2013). The van Genuchten (1980) model addresses this limitation. By incorporating the parameter $m = 1 - 1/n$ proposed by Mualem (1976), the modified van Genuchten-Mualem (VGM) model (Parker et al., 1987) is formulated as: $k_{r,g} = (1 - \alpha_{l,e})^{0.5} (1 - \alpha_{l,e}^{1/m})^{2m} \tag{37}$		Formatted: Indent: First line: 2 ch, Spa Before: 6 pt, After: 6 pt, Line spacing lines  Formatted  Formatted: Indent: First line: 2 ch, Spa Before: 6 pt, After: 6 pt, Snap to grid	1.5
402 403 404 405 406 407 408 409	$k_{r,d}$ enotes the relative permeability, where $n$ is a dimensionless coefficient determined by the properties of the porous medium. The Brooks-Corey (BC) model exhibits a sharp discontinuity at the air entry point, which can lead to poor data fitting, particularly for fine-textured soils (Assouline & Or, 2013). The van Genuchten (1980) model addresses this limitation. By incorporating the parameter $m=1-1/n$ proposed by Mualem (1976), the modified van Genuchten-Mualem (VGM) model (Parker et al., 1987) is formulated as: $k_{r,d} = \left(1 - \alpha_{l,e}\right)^{0.5} \left(1 - \alpha_{l,e}^{1/m}\right)^{2m} \tag{37}$		Formatted: Indent: First line: 2 ch, Spa Before: 6 pt, After: 6 pt, Line spacing lines  Formatted  Formatted: Line spacing: 1.5 lines  Formatted: Line spacing: 1.5 lines  Formatted: Formatted	1.5

413 permeability (Yang et al., 2019), indicating that pore tortuosity-connectivity plays a dominant role 414 in groundwater two-phase flow. Therefore, this study conducts simulations and parameter 415 sensitivity analyses for both the Brooks-Corey (BC) and van Genuchten-Mualem (VGM) models. 416 Formatted: b2 2.3 CFPv2 model 417 The CFPv2 model, proposed by Reimann et al. (2014), is an advanced version of MODFLOW-Formatted: Font: Cambria Math, 10 pt Formatted: Indent: First line: 2 ch, Line 418 CFP (Shoemaker et al., 2008). It extends functionalities such as flow interactions between conduits spacing: 1.5 lines 419 and porous media, as well as conduit boundary conditions. CFPv2 integrates with MODFLOW-2005 420 and employs the following approaches: Laminar Flow in Conduits: Described using the Hagen-Formatted: Font: Cambria Math, 10 pt, Not Bold Formatted: Font: Cambria Math, 10 pt 421 Poiseuille equation for discrete conduits within conduit networks. Turbulent Flow: Calculated by Formatted: Font: Cambria Math, 10 pt, Not Bold Formatted: Font: Cambria Math, 10 pt 422 combining the Darcy-Weisbach equation with the Colebrook-White equation. Laminar Flow in Formatted: Font: Cambria Math, 10 pt, Not Bold 423 Fractured Rock Matrix; Simulated via a continuum approach. Detailed technical documentation for Formatted: Font: Cambria Math, 10 pt 424 MODFLOW-CFP, including groundwater flow simulation methodologies, is provided by Shoemaker 425 et al. (2008). Successful applications and evaluations of the model have been reported in studies 426 such as Gallegos et al. (2013), Reimann et al. (2014), Chang et al. (2019), Gao et al. (2020), and 427 Shirafkan et al. (2023). 428 2.4 Model Comparison and Numerical Model Construction Formatted: b2 429 2.4.1 DBS Model Conversion and Applicability Assessment 430 As illustrated in Figure 2, the Navier-Stokes (N-S) model can resolve fine-scale pore-scale Formatted: Font: Cambria Math, 10 pt Formatted: Indent: First line: 2 ch, Line spacing: 1.5 lines, No bullets or numbering 431 flows and perform high-fidelity simulations. In contrast, the CFPv2 model achieves high 432 computational efficiency and stability by discretizing one-dimensional conduits within porous 433 media. The DBS (Dual-domain Brinkman-Stokes) model combines the advantages of both 434 approaches: By incorporating additional resistance source terms into the N-S equations, it Formatted: Font: Cambria Math, 10 pt, Not Bold Formatted: Font: Cambria Math, 10 pt 435 maintains high-fidelity flow resolution in conduits. For porous media, it adopts a Darcy-type flow 436 formulation, significantly reducing computational costs. Formatted: Font: Cambria Math, 10 pt, Not Bold 437 However, the DBS model operates in three dimensions (3D), requiring grid refinement around Formatted: Font: Cambria Math, 10 pt Formatted: Indent: First line: 2 ch, Line

Formatted: Font: Cambria Math, 10 pt, Not Bold

Formatted: Font: Cambria Math, 10 pt

conduits and their vicinity to ensure accurate flow resolution. This increases computational load

compared to the 1D conduit flow framework of CFPv2. To address this challenge, all simulations in

438

Formatted: Font: Cambria Math, 10 pt 441 computational power for handling complex 3D meshes. 442 2.4.2 Model Comparison and Discretization Schemes Formatted: b3 443 To further investigate the effectiveness of the DBS model in addressing interactions between 4 Formatted: Font: Cambria Math, 10 pt Formatted: Indent: First line: 2 ch, Line 444 karst groundwater and adjacent streams, this study compares the differences between the spacing: 1.5 lines, No bullets or numbering 445 MODFLOW-CFP and DBS models. As shown in Figure 3(a.1), the comparison begins with their 446 coupling modes of conduits and porous media from the perspectives of governing equations and 447 grid discretization: MODFLOW-CFP: Groundwater exchange between conduits, porous media, and Formatted: Font: Cambria Math, 10 pt, Not Bold Formatted: Font: Cambria Math, 10 pt 448 streams relies on stable hydraulic heads between conduit-porous media and stream-porous media 449 interfaces (Figure 3(a.2)). Flow interactions between porous matrix and discrete conduits are 450 linear and driven by head differences (Barenblatt et al., 1960). DBS Model: Groundwater Formatted: Font: Cambria Math. 10 pt. Not Bold Formatted: Font: Cambria Math, 10 pt 451 interactions among conduits, streams, and porous media are governed by saturation and pressure 452 gradients between adjacent grid nodes, allowing simultaneous recharge or discharge across 453 interfaces (Figure 3(a.3)). However, this requires calculating flux variations across all grids. 454 Comparison of Stream-Porous Media Interaction Modes; MODFLOW-CFP; Streams are Formatted: Font: Cambria Math, 10 pt, Not Bold Formatted: Font: Cambria Math, 10 pt 455 discretized into single grid cells, with exchange fluxes determined by head differences. Fluctuating Formatted: Font: Cambria Math, 10 pt, Not Bold Formatted: Font: Cambria Math, 10 pt 456 stream stages are simplified to a uniform water level, and "dry zones" cannot be simulated in 457 porous media (Figure 3(a.4)). DBS Model; Media properties (e.g., porosity, permeability) are Formatted: Font: Cambria Math, 10 pt, Not Bold Formatted: Font: Cambria Math, 10 pt 458 assigned at grid nodes, and interface values are interpolated. Direct conduit-stream interactions 459 eliminate the need for porous media as an intermediary. Stream geometry can be defined as regular 460 (rectangular) or irregular (Figure 3(a.5)). The DBS model employs the Volume of Fluid (VOF) and 461 Front-tracking methods to reconstruct dynamic water-air interfaces, enabling simulation of 462 fluctuating interfaces under sufficiently refined grids. 463 Discretization Schemes: This study adopts a dynamic programming approach to generate Formatted: Font: Cambria Math, 10 pt, Not Bold Formatted: Font: Cambria Math, 10 pt 464 sinkhole and conduit grids, allowing flexible placement of conduits with adjustable diameters and Formatted: Indent: First line: 2 ch, Line spacing: 1.5 lines 465 coordinates, enhancing model adaptability (contrasting fixed conduit positioning in studies like Formatted: Font: Cambria Math, 10 pt, Not Bold 466

Formatted: Font: Cambria Math, 10 pt, Not Bold

Formatted: Font: Cambria Math, 10 pt

Formatted: Indent: First line: 2 ch, Line spacing: 1.5 lines, No bullets or numbering

Kavousi et al., 2020; Pardo-Igúzquiza et al., 2018; Li et al., 2023).

this study were executed on a Lenovo ThinkSystem SR665 server, which provides the necessary

440

468	Regions are divided into free-flow zones (streams, sinkholes, conduits) and porous media. Free-			
469	flow zones use locally refined grids to capture micro-scale variations in water levels and interfaces.			
470	$\underline{Porous\ media\ zones\ adopt\ gradually\ coarsening\ grids\ (edge\ cells\ twice\ the\ size\ of\ conduit-adjacent}$			
471	cells), balancing accuracy and computational efficiency. Permeability is graded, decreasing			
472	outward from conduits to reflect dissolution effects.			
473	CFPv2 Discretization (Figure 3(c)): Conduits are embedded in porous media and directly		Formatted	···
474	connected to streams. Domain dimensions: 200 m $\times$ 200 m $\times$ 30 m (length $\times$ width $\times$ thickness).			
475	Groundwater flows from porous media to conduits and discharges into streams (Figure 11(a.1)).			
476	Porous media: Homogeneous, initial head = 10 m, no-flow boundaries. Conduits: Diameter =		Formatted	(
477	1  m, roughness = $0.01  m$ , wall interaction parameter = $25  m/s$ , outlet collocated with stream grid.			
478	<u>Initial conditions</u> ; <u>Spring discharge = 0, conduit node elevation = 1 m, water temperature = 20°C.</u>	//		
479	Boundary conditions; Rainfall recharge at the top, total simulation time = 45,000 s, MODFLOW-			
480	<u>CFP stress periods = 1 min.</u>			
481	2.5 Rainfall Infiltration Recharge Boundary		Formatted: b2	
482	The upper boundaries of both the DBS and CFPv2 models are defined as transient natural.	_	Formatted: Font: Cambria Math, 10 pt	
483	precipitation boundary conditions. In this study, the rainfall infiltration recharge boundary		Formatted: Indent: First line: 2 ch, Li spacing: 1.5 lines	ne
484	condition is formulated as follows (Huang et al., 2024; Chang et al., 2015):			
			Formatted	
485	$I(t) = \frac{b}{\sqrt{2\pi\sigma^2}} \sum_{n=0}^{\infty} e^{-\frac{\left(\frac{t_n}{a} - \mu\right)^2}{2\sigma^2}} $ (39)		rormatted	(
486	Here, $t_{i,i}$ denotes the time of the $i$ -th rainfall event, and $I(t)$ , represents the total rainfall amount.		Formatted: Font: Cambria Math, 10 pt	
487	at that time. According to Chang et al. (2015), the parameters $\mu_{N}$ $\sigma_{n}^{2}$ and $\alpha_{n}$ are set as constants (90,		Formatted	(
	at that time. According to change that, (2013), the parameters u. V. and u. are set as constants (70.	$\mathcal{N}$	Formatted	
488	1.5, and 20, respectively). Variations in rainfall intensity during the infiltration recharge process		Formatted	
489	are controlled by adjusting the value of the dimensionless parameter $p_{\mathbf{z}}$		Formatted: Indent: First line: 2 ch, Li spacing: 1.5 lines	
1		1/	Formatted: Font: (Default) Cambria Math, Formatted	10 pt
		1/	<u> </u>	<u> </u>
		\	Formatted	

#### 3. Results

490

493

494

495

496

497

498

499

500

501

502

503

504

505

506

507

508

509

510

511

512

513

514

515

516

517

3.1 Interaction process between the karst aquifer and stream under precipitation infiltration recharge

## 3.1.1 Karst Aquifer-Stream Interactions Under Varying Precipitation Intensities

The changes in hydrological process curves, water level fluctuations, and their differences during the interaction between karst media and stream under different precipitation intensities are shown in Fig. 3Fig. 4. In the early stage of precipitation, the flow in the stream primarily originates from direct precipitation recharge and lateral groundwater recharge from epikarst (Fig. 3Fig. 4(a)). As the water level in the stream gradually rises, the flow not only continues downstream but also begins to recharge the karst aquifer, particularly the PM II. The peak recharge to PM II coincides with the peaks of epikarst recharge to the stream (Epikarst in Fig. 3Fig. 4) and direct precipitation recharge (P-River in Fig. 3Fig. 4). Therefore, the interaction process between the karst aquifer and stream during the early precipitation stage is significantly influenced by lateral groundwater discharge from the epikarst and the direct precipitation recharge. As groundwater recharge from epikarst to the stream declines (Fig. 3Fig. 4 (a)), groundwater moves downward through the epikarst to PM  $_{\mbox{\scriptsize A}}$ I  $_{\mbox{\scriptsize A}}$  and begins to gradually recharge the stream. Due to the low permeability of the epikarst, lateral discharge from PM, I to the stream will be delayed. During this process, the discharge volume of PM, I exhibits two distinct peaks. The first peak is due to the recharge of groundwater from the epikarst, while the second peak is caused by the gradual saturation of PM\_II, and the karst conduit, with a proportion of groundwater overflowing from PM I and discharging laterally to the stream. After the end of precipitation recharge, the hydrological process curve of PM I rapidly declined, and the discharge volume of the karst conduit, PM III and PM\_II\_gradually increase, causing the water level in the stream to rise (Fig. 3Fig. 4 (d)). When the water level in the stream gradually exceeds that of  $PM_{\ A}I_{\ A}$  the stream begins to gradually recharge PM, I, The karst conduit, PM, II, and PM, III, continue to discharge to the stream during this stage due to higher internal water pressure, forming a local hydrological cycle with the upper layer. In the late stage of precipitation, the hydrological process of the stream primarily shows a gradual decline in baseflow.

Formatted: Font: (Asian) Times New Roman, 10 pt, Font color: Black, English (United Kingdom), Kern at 三号

Formatted: Level 1, Space Before: 24 pt, After: 12 pt, Line spacing: single, Widow/Orphan control, Keep with next

Formatted: b2

Formatted: Font: (Default) Cambria Math, 10 pt
Formatted: Indent: First line: 2 ch, Line

Formatted: Font: (Default) Cambria Math, 10 pt
Formatted: Font: (Default) Cambria Math, 10 pt

(Default) 宋体, 10 pt Formatted: Font: Formatted: Font: (Default) Cambria Math, 10 pt Formatted: Font: (Default) 宋体, 10 pt Formatted: Font: (Default) Cambria Math. Formatted: Font: (Default) Cambria Math, 10 nt Formatted: Font: (Default) Cambria Math, 10 pt Formatted: Font: (Default) 宋体, 10 pt Formatted: Font: (Default) Cambria Math, 10 pt Formatted: Font: (Default) 宋体, 10 pt Formatted: Font: (Default) Cambria Math, 10 pt Formatted: Font: (Default) 宋体, 10 pt Formatted: Font: (Default) Cambria Math, 10 pt Formatted: Font: (Default) 宋体, 10 pt

(Default) Cambria Math, 10 pt

(Default) Cambria Math, 10 pt

(Default) 宋体, 10 pt

(Default) 宋体, 10 pt

Formatted: Font: (Default) Cambria Math, 10 pt

Formatted: Font: (Default) Cambria Math, 10 pt

Formatted: Font: (Default) 宋体, 10 pt

Formatted: Font:

Formatted: Font:

Formatted: Font:

Formatted: Font:

Formatted: Font: (Default) 宋体, 10 pt
Formatted: Font: (Default) Cambria Math. 10 pt

As depicted in Figs. 3b and 3c, the recharge and discharge dynamics between the karst aquifer and stream across different media shift notably with escalating precipitation intensity. The recharge volumes from the stream to PM II and PM III both decrease. The reduction in the recharge to PM\_II\_from the stream is primarily due to the acceleration of groundwater movement downward as precipitation intensity increases, causing groundwater to move more rapidly to the bottom of the karst aquifer, thereby recharging PM II. Consequently, part of pore space that should have been recharged by the stream is instead recharged from PM I downward. The decrease in the recharge to PM, I, can be attributed to its high internal saturation level and the rise in water level. On the other hand, the water level in the stream does not significantly exceed that of the upper aquifer, making it difficult for the stream to effectively recharge the aquifer. Due to the reduced recharge volume to the aquifer, the discharge from the stream is partially lower than the discharge from the epikarst during the early stage of the hydrological process.

518

519

520

521

522

523

524

525

526

527

528

529

530

531

532

533

534

535

536

537

538

539

540

541

542

543

544

545

With changes in precipitation intensity (b = 3, 5, and 7), the water level variations and their differences between the karst aquifer and stream exhibit complex dynamic characteristics (Figs. 3d, 3e and 3f). During the early stage of precipitation, despite the increasing water level difference, the discharge from the stream to the aquifer is gradually decreasing (as shown by the negative values for PM I and PM II in Fig. 3Fig. 4a, 3b and 3c). This phenomenon indicates that water level is not the only factor controlling the interaction between the karst aquifer and stream; changes in the degree of saturation also play a significant role. As shown in Fig. 3Fig. 4d, under low precipitation intensity, the water level difference between the karst aquifer and stream is often greater than the water level of the stream during the middle and later stages of precipitation. However, as precipitation intensity increases, the water level difference tends to decrease (Fig. 3Fig. 4b and 3c). This change is primarily due to the increased precipitation intensity leading to a faster saturation of the karst aquifer, thereby limiting the ability of the stream to recharge the aquifer. After the middle stage of precipitation, the interaction between the stream and the upper part of the aquifer gradually intensifies, while the lower part of the aquifer discharges to the stream (Fig. 3Fig. 4a). Due to the gradual decrease in water level difference, it is difficult for the stream to effectively recharge the aquifer. In this process, the interaction between the aquifer and stream is

Formatted: Font: (Default) 宋体, 10 pt Formatted: Font: (Default) Cambria Math, 10 pt Formatted: Font: (Default) 宋体, 10 pt Formatted: Font: (Default) Cambria Math, 10 pt Formatted: Font: (Default) 宋体, 10 pt Formatted: Font: (Default) Cambria Math, 10 pt

Formatted: Font: (Default) 宋体, 10 pt Formatted: Font: (Default) Cambria Math, 10 pt

Formatted: Font: 10 pt Formatted: Font: (Default) Cambria Math, 10 pt Formatted: Font: 10 pt Formatted: Font: (Default) Cambria Math, 10 pt

Formatted: Font: 10 pt

Formatted: Font: (Default) Cambria Math, 10 pt

controlled by the dynamic changes in saturation.

Based on the comparison between DBS and Modflow-CFPv2 results in Figs 4(a), (b), and (c), the CFPv2 model exhibits a single-peak hydrograph with exponential recession characteristics, failing to capture flow process line disturbances caused by multi-media interactions. Under precipitation intensities b=3 and 5, the CFPv2 model shows an immediate rapid increase in stream discharge during early stages rather than gradual enhancement, though total discharge and baseflow during later stages remain comparable (as shown in Table 3). Specifically, for b=3, the peak stream discharge in Modflow-CFPv2 occurs at 2520 s, earlier than in the DBS model. This discrepancy arises because the precipitation recharge package in CFPv2 directly elevates water levels, whereas the DBS model simulates a gradual vertical infiltration process along the Z-axis. Lower precipitation intensity reduces groundwater infiltration rates and prolongs water table replenishment time, consequently delaying lateral discharge timing. At b=7, both models exhibit comparable first discharge peaks, but the DBS model generates a secondary peak through overflow effects that rapidly recedes after overflow cessation. In contrast, CFPv2 demonstrates smooth exponential recession without secondary features due to its simplified vertical stratification that neglects multi-component interactions.

The comparable results between DBS and Modflow-CFPv2 models under variable recharge conditions demonstrate the reliability and stability of DBS in simulating karst aquifer systems. Although the DBS model captures more interaction details, it requires greater computational resources. The absence of overflow mechanisms and multi-media interactions in CFPv2 leads to simplified discharge recession patterns that fail to reflect intense component interactions within the system. This comparative analysis highlights the DBS model's advantages in characterizing complex conduit-stream-aquifer interactions while acknowledging its computational demands.

It is self-evident that changes in precipitation intensity significantly affect the recharge and discharge processes between the karst aquifer and stream. The water levels and saturation degrees of the respective media act as core controlling factors that jointly influence the interactive dynamics between the aquifer and stream. To gain a deeper understanding of these influencing

factors and their interaction mechanisms, and to further elucidate the interaction process mechanisms between the karst aquifer and stream, this study focuses on the hydrological interaction process between the two during the early stage of precipitation.

574

575

576

577

578

579

580

581

582

583

584

585

586

587

588

589

590

591

592

593

594

595

596

597

598

599

600

601

## 3.1.2 Interaction process between the karst aquifer and stream during early stage of precipitation

Figure 4Figure 5 illustrates how the interaction volume between the epikarst, porous media, and stream varies under different precipitation intensities. As shown in Fig. 4Fig. 5a, at a precipitation intensity, b=3, the contribution ratios of the epikarst, PM I and PM II to the recharge of the stream are similar. This indicates that during the early stage of precipitation, the recharge effects of each medium on the stream are relatively balanced. Since groundwater vertically recharges the underlying aquifer through the epikarst, the discharge peak of PM II is relatively delayed compared to the epikarst and PM I

As the precipitation intensity increases (b = 5), the contribution ratios of the epikarst, PM  $_{\bullet}$ I and PM II to the recharge of stream experience significant changes (Fig. 4Fig. 5b). Upon comparing Fig. 4Fig. 5a and 4b, it is evident that an increase in precipitation intensity leads to higher discharge volumes for both PM I and PM II, with PM II experiencing a more pronounced rise. Additionally, the peaks of their discharges occur earlier. The first peak of PM, I is primarily caused by infiltration recharge from precipitation. With the increase in precipitation intensity, the infiltration velocity accelerates and the recharge volume increases, leading to a larger discharge volume and an earlier peak for PM I (vertical recharge peak). Groundwater continues to move downward from PM, I, and the saturation of PM, II, rises, allowing more groundwater to overflow and discharge through PM, I, thereby generating the second peak (overflow peak), For PM II, as discussed in Section 3.1, increase in saturation reduces the recharge from stream, but the discharge volume increases gradually after the middle stage of precipitation, and its contribution to the recharge of the stream becomes dominant among the three. This is due to the increased precipitation intensity, which allows PM II to receive more vertical recharge, enhancing its discharge capacity. When the precipitation intensity continues to increase (b = 7, Fig. 4Fig. 5c), PM II gradually reaches saturation. According to the analyses in Section 3.1, the ability of PM II to receive recharge is limited by its own saturation level, making it difficult to receive vertical recharge.

```
Formatted: b3
```

Formatted: Font: (Default) Cambria Math, 10 pt
Formatted: Indent: First line: 2 ch, Line
spacing: 1.5 lines

Formatted: Font: 10 pt

Formatted: Font: (Default) Cambria Math, 10 pt

Formatted: Font: (Default) 宋体, 10 pt

Formatted: Font: (Default) Cambria Math, 10 pt

Formatted: Font: (Default) 宋体, 10 pt

Formatted: Font: (Default) Cambria Math, 10 pt

Formatted: Font: (Default) 宋体, 10 pt

Formatted: Font: (Default) Cambria Math, 10 pt

Formatted: Font: (Default) 宋体, 10 pt

Formatted: Font: (Default) Cambria Math, 10 pt

Formatted: Font: 10 pt

Formatted: Font: (Default) Cambria Math, 10 pt

Formatted: Font: (Default) 宋体, 10 pt

Formatted: Font: (Default) Cambria Math, 10 pt

Formatted: Font: (Default) 宋体, 10 pt

Formatted: Font: (Default) Cambria Math, 10 pt

Formatted: Font: (Default) 宋体, 10 pt

Formatted: Font: (Default) Cambria Math, 10 pt

Formatted: Font: (Default) 宋体, 10 pt

Formatted: Font: (Default) Cambria Math, 10 pt

Formatted: Font: (Default) 宋体, 10 pt

Formatted: Font: (Default) Cambria Math, 10 pt

Formatted: Font: (Default) 宋体, 10 pt

Formatted: Font: (Default) Cambria Math, 10 p

Formatted: Font: (Default) Cambria Math, 10 p

Formatted: Font: (Default) Cambria Math, 10 pt

Formatted: Font: 10 pt

Formatted: Font: (Default) Cambria Math, 10 pt

Therefore, despite the increased precipitation intensity, the discharge volume of  $PM_{a}II_{a}$  does not increase significantly. Conversely, due to the influence of the saturation state of the underlying aquifer medium, the second peak (overflow peak) of  $PM_{a}I_{a}$  is more pronounced, indicating a more evident overflow phenomenon. Under higher precipitation intensity, the recharge contribution of  $PM_{a}I_{a}$  to the stream dominates.

Thus, variations in precipitation intensity notably influence the interaction volume between the karst media and stream. As precipitation intensity increases, the discharge volume and peak values of each medium are altered. Specifically, the two peaks of PM I show sequential changes in intensity, which are modulated by the saturation levels of the adjacent media.

3.1.3 Interaction process between the karst aquifer and stream during early stage of precipitation

The DBS model, leveraging its fine grid resolution and two-phase flow simulation capability, can accurately capture the interactive processes between various media (e.g., saturated-unsaturated zones, conduit-stream systems) influenced by dynamic saturation processes during precipitation infiltration recharge. As the interactions between adjacent media are governed by variations in saturation levels, the numerical results under rainfall intensity b=5 are selected for further analysis of dynamic inter-media interactions. For instance: How does the threshold attainment of storage capacity in the lower porous media affect the hydrological processes of the upper porous media?

As shown in Fig. 12Fig. 6, the Darcy-Brinkman-Stokes model clearly demonstrates the changes in the saturation levels of epikarst, porous media, and the karst spring; the saturation fields and the interaction between various media at 4000 s, 6105 s, and 7363 s; the interaction amounts between epikarst, porous media I, II, III, and the stream. From Fig. 12Fig. 6 (a.1), it can be seen that the saturation level of epikarst rises and declines earliest, but the saturation level is relatively low, and it is in a completely unsaturated flow state. Porous media I and III rise synchronously before 5000 s, while porous media II and the karst spring rise rapidly at 4611 s. At 7409 s, the karst spring and porous media I successively enter the decline stage. Due to the rapid drainage of the conduit, the saturation level decreases. The saturation level of the karst spring decreases faster than that of porous media I and intersects with porous media I at 9670 s.

Formatted: Font: (Default) 宋体, 10 pt

Formatted: Font: (Default) Cambria Math, 10 pt

Formatted: Font: (Default) 宋体, 10 pt

Formatted: Font: (Default) Cambria Math, 10 pt

Formatted: Font: (Default) 宋体, 10 pt

Formatted: Font: (Default) Cambria Math, 10 pt

Formatted: b3, Indent: First line: 0 cm

Formatted: Font: (Default) Cambria Math, 10 pt

Formatted: Indent: First line: 2 ch, Line

spacing: 1.5 lines

Formatted: Font: (Default) Cambria Math, 10 pt

Combining Fig. 12Fig. 6 (a.2) with other sub-figures, the stages with obvious interactions among porous media can be divided into the infiltration stage (green), the overflow stage (red), and the recession stage (blue). During the infiltration stage from 4000 s to 4611 s, as shown in Fig. 12 Fig. 6 (a.2.1), epikarst vertically replenishes porous medium I and infiltrates downward. However, the infiltrating water does not reach the lower media. Meanwhile, the saturation levels of porous media II, III, and the conduit gradually increase (see Fig. 12 Fig. 6 (a.1)). Combining with Fig. 12Fig. 6 (a.3), it can be seen that epikarst laterally replenishes the stream, and quickly drops to the bottom of the riverbed due to gravity. At this time, the lower aquifer system (porous media II, III, and the conduit) is in a dry state, so the stream replenishes the lower aquifer. The amount of recharge received by porous medium III and the conduit is less than that of porous medium II (analyzed by combining Fig. 12Fig. 6 (a.3) and (a.4)), but their saturation levels increase faster. There are two reasons for this situation: First, the bottom elevation of the conduit is 1 m, and the water level of the stream needs to submerge the 1 m water level before it can recharge the conduit. Second, porous medium III is not only replenished by the stream, but also the sinkhole diverts the groundwater in epikarst and porous medium I to the conduit (the sinkhole flow velocity and saturation as shown in Fig. 12Fig. 6 (a.2.1)), and then replenishes porous medium III. As the lower aquifer media gradually tends to be saturated with rainfall recharge, as shown in Fig. 12Fig. 6 (a.2.2), porous media II and III tend to be saturated (see Fig. 12Fig. 6 (a.2.1)). Due to the weak compressibility of water, after the upper part infiltrates and replenishes porous medium I, it tends to laterally replenish the stream from the interface between porous medium II and stream. As the saturation level of porous medium I gets higher, the lateral recharge to the stream becomes more significant, showing an obvious overflow state. The depression between the two peaks is caused by the rapid rise of the stream water level. During the flood peak stage, the discharge from porous media to stream decreases. At the same time, the rise of the stream water level makes it difficult for the lower porous media to replenish the stream, and porous medium II tends to be saturated, making it difficult to replenish porous medium I. During this stage, the flow between porous media I and II is in a dynamic equilibrium state. As shown in Fig. 12 Fig. 6 (a.2.3), during the recession stage, the rainfall infiltration intensity decreases rapidly. Under the action of gravity, the

630

631

632

633

634

635

636

637

638

639

640

641

642

643

644

645

646

647

648

649

650

651

652

653

654

655

656

groundwater vertically replenishes porous medium I, the conduit, and porous medium II successively recedes. And the water level of the stream drops rapidly (see Fig. 3 (e)). The groundwater tends to be discharged to the stream through porous medium I and the karst spring. Porous medium I is replenished by porous medium II on the one hand and discharges to the stream on the other hand. Therefore, during a single rainfall event, during the infiltration stage, part of the amount of water replenished from epikarst to the stream is discharged, and other part is redirected to replenish the lower porous media; during the overflow stage, the stream is mainly replenished through the karst conduit and porous medium II. Porous medium I and the stream are in a dynamic equilibrium state. During the recession stage, the porous media act as the main medium to replenish the stream.

As shown in Fig. 12Fig. 6 (a.4), the karst spring reaches its peak at 7409 s. This is due to the rainfall infiltration, the recharge from porous medium I, and the subsequent discharge to the stream. As the storage volume decreases, the amount of recharge from the karst spring to the stream decreases. A trough appears at 11642 s. This is because as the water level of the stream drops, groundwater is more easily discharged into the stream. However, as the overall storage volume continues to decline, after a peak appears at 13057 s, it enters a complete recession stage. Affected by the decline of the stream water level, the discharge from porous medium III to the stream gradually increases during the recession stage. Combining with Fig. 12Fig. 6 (a.1), it can be seen that while porous medium III is discharging, its saturation remains at level I continuously, indicating that the conduit continuously supplies water vertically to porous medium III.

Under the recharge of rainfall infiltration, the interaction process between the karst aquifer affected by epikarst, sinkholes, conduit and the stream shows dynamic changes in terms of staged characteristics, main interaction media, and the dynamic equilibrium process among different media. The accurate simulation of the above complex processes depends on the support of a three-dimensional two-phase numerical model (Darcy-Brinkman-Stokes model).

3.3 Impact of different water retention characteristics on the interaction process between the karst

## aquifer and stream

685

686

687

688

689

690

691

692

693

694

695

696

697

698

699

700

701

702

703

704

705

Figure 5 illustrates the changes in saturation of water retention curves based on two different retention equation for karst aquifer: the BC model (equations (12)-(13)) and the VGM model (equations (14)-(15)). For the same infiltration periods, the water content predicted by BC model is generally higher than that predicted by the VGM model. The BC model may focus more on the static retention of groundwater in the medium, while the VGM model may emphasize the dynamic transport and distribution of groundwater within the medium. Moreover, the VGM model predicts a greater distance of groundwater movement compared to the BC model, indicating that the VGM model may have higher sensitivity in simulating infiltration processes of groundwater in the medium. This difference is of significant importance for the dynamic process of unsaturated two phase flow in the karst aquifer and for accurately predicting the advancement path of groundwater. In addition, there are differences between the BC model and the VGM model in simulating the saturation changes of the water retention curve (Fig. 5). Not only do they differ in the degree of saturation change at the same time and location, but their simulation results for the distance of groundwater Therefore, it is crucial to select the appropriate model based on specific lithological conditions, as this can more accurately describe and predict the two-phase flow of karst groundwater. The impact of different water retention models on the interaction process between the karst aquifer and stream is shown in Fig. 6. Compared to the BC model, the VGM model generally calculates lower discharge volumes from the stream. Therefore, under the simulation conditions of the VGM model, more groundwater is retained in the porous medium rather than being discharged through the stream. This

reflects the differences between the two water retention models in simulating the movement and storage

of groundwater in the porous medium. During the early stage of precipitation recharge, VGM model results show that the stream is more likely to recharge the karst conduit (Fig. 6b). Although the karst conduit receives more recharge from stream, their discharge to stream is relatively low. This indicates that the karst conduit derived from the VGM model receive relatively lower recharge intensities from the porous medium and sinkhole. As shown in Fig. 6c, due to the shorter distance of groundwater movement derived from the VGM model within the same time, the vertical infiltration capacity of the epikarst is reduced, thereby increasing the discharge volume of the epikarst to the stream. This indicates that the interaction process between stream and the epikarst is significantly influenced by the water retention characteristics. In the VGM model, the difficulty of groundwater moving vertically through the epikarst increases, leading to a decrease in the discharge volume of PM I (Fig. 6d). Since PM I receives limited recharge from the epikarst, its saturation remains at a low level, making it more favorable to receive recharge from stream (see Section 3.1). The VGM model results suggest that the stream predominantly recharges PM II (as seen in Figs and 6c). However, during the middle and later stages, the stream recharge volume calculated by the BC model surpasses that of the VGM model. Figure 6f illustrates that the groundwater in the porous medium beneath the karst conduit primarily originates from conduit recharge. Meanwhile, Fig. 6b shows an increase in the discharge volume from the karst conduit, as estimated by the BC model. This increase subsequently affects the discharge volume of the porous medium below the karst conduit. Therefore, different water retention models have a significant impact on the interaction process between the karst aquifer and stream. These impacts are not only reflected in the changes of discharge and recharge volumes but also involve the movement and storage mechanisms of groundwater in

706

707

708

709

710

711

712

713

714

715

716

717

718

719

720

721

722

723

724

725

different media. In practical applications, selecting an appropriate water retention model based on the

corresponding lithology can more accurately simulate and predict the interaction process between the

karst aquifer and stream.

727

728

729

730

731

732

733

734

735

736

737

738

739

740

741

742

743

744

745

746

747

748

749

750

751

752

753

3.25. Impact of multiple precipitation events on the interaction process between the karst aquiferent and stream

Rainy seasons typically experience multiple precipitation events, during which differences in precipitation peaks, durations, and cumulative precipitation events can all impact the interaction process between the karst aquifer and stream. Does the groundwater stored in the porous media of the karst aquifer system during the initial rainfall event influence the interactions between multi-component media during subsequent precipitation episodes?

Based on understanding the interaction mechanism of a single precipitation event, this study further analyzes the impact of multiple precipitation events on the interaction process. Figure 8-7 shows the changes in water level of stream under continuous precipitation events. When the intensities of two consecutive precipitation events remain constant, the water level of stream reaches both the highest and the lowest points, indicating that the water level is related to the total precipitation intensity. Even with different intensities of the first precipitation event ( $b_{14}$  = 3 and  $b_{14}$ =5), the trend of the water level changes in stream is consistent (Fig. 871) and 4). After the first precipitation event, the karst aquifer receives infiltration recharge from the precipitation and can store part of the water, so the water level of stream will be higher during the second precipitation event, and the greater the intensity of the second precipitation event, the higher the water level of stream (Fig. §7(1) and (2), or (3) and (4)). This indicates that the intensity of the second precipitation event determines the amount of recharge from each medium to stream. Therefore, when the intensity of the first precipitation event is the same, the amplitude of the water level change in stream during the second precipitation event is only related to the intensity of the second precipitation event. When the intensity of the second precipitation event is the same, the storage capacity of the karst aquifer during the first precipitation event determines the amplitude of the water level change in stream during the second precipitation event. When the total precipitation Formatted: b2

Formatted: Font: (Default) Cambria Math, 10 pt

Formatted: Indent: First line: 2 ch, Line

spacing: 1.5 lines

Formatted: Font: 10 pt

Formatted: Font: 10 pt

Formatted: Font: (Default) Cambria Math, 10 pt

Formatted: Font: 10 pt
Formatted: Font: 10 pt

Formatted: Font: (Default) Cambria Math, 10 pt

intensity is the same (Fig. 8-7.2) and 3), if the intensity of the first precipitation event is lower than that of the second one, the amplitude of the water level change in stream is higher, and vice versa. This is because, in the case of two consecutive precipitation events, part of the precipitation infiltrates and recharge the storage during the first event, and the other part is discharged to stream through the aquifer. Combining Fig. 3d-4d and 3ee, during the first precipitation event, the water level in the porous medium rises and stores a proportion of water, but the discharge volume to stream is greater when the precipitation intensity is higher ( $b_{11} = 5$ ) compared to when it is lower ( $b_{11} = 3$ , Fig. 3a-4a and b). When the second precipitation event occurs, due to the similar saturation levels of the karst aquifer, the greater the intensity of the second precipitation event, the larger the amount of groundwater recharged to stream through the aquifer, and the more pronounced the amplitude of the water level in stream.

754

755

756

757

758

759

760

761

762

763

764

765

766

767

768

769

770

771

772

773

774

775

776

777

778

779

780

781

Figure 9-8 illustrates the hydrological process curves of the stream during two consecutive precipitation events, as well as the interaction processes between the various media of the karst aquifer and stream. Under different precipitation intensities, the various media of the karst aquifer recharge the stream with varying intensities, resulting in significant fluctuations in the water level of stream. Based on Fig. 8(a) and Fig. 7 (2) and 4), it can be observed that under two consecutive precipitation events, when the intensity of the second precipitation event is equal to or greater than the first, the stream hydrograph exhibits more pronounced fluctuations. The comparison between the DBS model and MODFLOW-CFPv2 model under different b<sub>1</sub> parameter combinations demonstrates distinct characteristics in streamflow hydrographs: the DBS model shows higher peak discharge with greater fluctuations, while the MODFLOW-CFPv2 model displays relatively smoother discharge variations. Notably, under the second precipitation event, the MODFLOW-CFPv2 model exhibits delayed peak elevation timing. Furthermore, its recession phase still follows an exponential decay pattern, failing to capture the rapid interactive response between multimedia systems during successive precipitation events. Combining Fig. 9a and Fig. 8 (2) and 4), it can be concluded that during two consecutive precipitation events, when the intensity of the second precipitation is greater than or equal to that of the first one, the amplitude of the hydrological process of stream is larger. As shown in Fig. 9b8b, the epikarst discharges quickly and Formatted: Font: 10 pt
Formatted: Font: 10 pt
Formatted: Font: 10 pt
Formatted: Font: (Default) Cambria Math, 10 pt
Formatted: Font: (Default) Cambria Math, 10 pt

Formatted: Font: 10 pt

Formatted: Font: (Default) Cambria Math, 10 pt

Formatted: Font: 10 pt

Formatted: Font: (Default) Cambria Math, 10 pt

is not easily affected by multiple precipitation events. However, when the intensity of the first precipitation is high and the intensity of the second precipitation is the same (1) and 3), the discharge volume of the epikarst to stream during the second precipitation period is slightly larger. When the intensity of the first precipitation is different and the intensity of the second precipitation is the same (Fig. 9c.8c 2) and 4), the discharge volume of groundwater through karst conduit to stream during the second precipitation period is almost the same. This is because karst conduit discharge quickly, and the storage volume of the conduit during the first precipitation period has little impact on the storage volume during the second precipitation period. Therefore, combining with Fig. 87, it is known that the storage effect of the karst aquifer mainly occurs in the porous medium, and it also indicates that relying solely on changes in the water level of stream makes it difficult to clearly determine the storage volume of the porous medium and conduit during the first precipitation event, and their respective impacts on the second precipitation period (Fig. 87). When the intensity of the second precipitation is higher (Fig. 9c.8c 2), 3 and 4), the discharge volume of the porous medium (PM II) to stream does not increase significantly. This is because the intensity of the second precipitation is larger, causing the water level of stream to rise (Fig. 87), making it difficult for the porous medium (PM II) to recharge stream.

782

783

784

785

786

787

788

789

790

791

792

793

794

795

796

797

798

799

800

801

802

803

804

805

806

807

808

809

Therefore, under the influence of two consecutive precipitation events, the greater the total precipitation intensity, the larger the discharge volume of the karst aquifer to stream. The storage effect of the karst aquifer occurs in the porous medium and affects subsequent precipitation processes. The lower-level porous medium (PM II), due to the high water level and large fluctuations of stream, is more difficult to recharge stream, and the recharge from stream mostly comes from overflow supply from the media in other layers.

## 3.3. Effects of Water Retention Characteristics on Karst Aquifer-Stream Interactions

The external recharge of the system significantly influences the interaction processes among different media. This study further investigates how the inherent hydrogeological properties of karst systems affect these interactive processes. Variable saturated flow in the karst vadose zone plays a critical role (Dvory et al., 2018), where the water retention characteristics of porous media govern unsaturated flow dynamics. However, the CFPv2 model struggles to simulate variable saturation processes. This

Formatted: Font: (Default) Cambria Math, 10 pt Formatted: Font: (Default) Cambria Math, 10 pt

Formatted: b2

Formatted: Font: 10 pt

Formatted: Indent: First line: 2 ch, Line

spacing: 1.5 lines

810 paper compares the DBS model results with two distinct experimental datasets to elucidate the 811 advantages and limitations of the DBS approach in simulating variable saturated flow. 812 Case 1: A typical unsaturated-unsteady seepage problem in sandy clay loam (Warrick et al., 1985), 813 where the soil hydraulic properties are provided by the international UNSODA database (Leij et al., 814 1996). Key parameters include:  $k = 1 \times 10 - 6$  m/s,  $\alpha_n = 0.363$ ,  $\alpha_n = 0.186$ , and n = 1.53. The model 815 consists of a vertical soil column (1 m thickness) with an initial pressure head of -8 m across the domain. 816 The top boundary is set to a pressure head of 0 m to simulate free surface infiltration. 817 Case 2: A 2D laboratory infiltration experiment by Vauclin et al. (1979), widely used for evaluating 818 saturated-unsaturated unsteady seepage models. The soil slab measures 2.00 m in height, 6.00 m in 819 width, and 0.05 m in thickness, with an impermeable base and free drainage boundaries on both sides. 820 <u>Initially</u>, the water table is set at 0.65 m. A central 1.00 m section of the top boundary receives uniform 821 precipitation at 0.148 m/h for 8 hours, during which free surface evolution is monitored. Soil hydraulic 822 properties are described using the van Genuchten-Mualem model with parameters:  $k = 0.35 \, \text{m/h}$ ,  $\alpha_{\text{su}} =$ 823 0.30,  $\alpha_{\rm ph} = 0.01$ . Due to symmetry, the DBS model simulates the right half of the domain. 824 As shown in Fig. 9, the DBS model demonstrates strong agreement with both experimental datasets, 825 highlighting its capability to capture spatiotemporal variations in water-air two-phase flow. Comparative 826 analysis between DBS simulations and experimental data not only validates model reliability but also 827 enhances understanding of soil moisture transport mechanisms. This provides critical support for 828 simulating interactions between karst aquifers and adjacent streams. 829 Based on the well-validated two-phase flow DBS model, this study analyzes the impacts of different 830 water retention models on interactive flow between media. Fig. 10 presents the hydrograph curves under 831 different water retention model parameters (BCn=3, 2.5, 2 and VGMm=0.85, 0.8) for (a) stream, (b) 832 karst spring, (c) epikarst, (d) PM I, (e) PM II, and (f) PM III. Fig. 10(c.1) illustrates the parameter effects 833 on porous media morphology, where n≥2 and higher n values indicate more heterogeneous pore space 834 and complex structures. Fig. 10(d.1) compares water retention curves between BC and VGM models. 835 Combining Figs. 10(a) and (b), in the BC model, increasing n values progressively reduce

Formatted: Indent: First line: 2 ch, Line spacing: 1.5 lines

Formatted: Font: 10 pt

Formatted: Font: 10 pt

Formatted: Font: 10 pt
Formatted: Font: 10 pt
Formatted: Font: 10 pt
Formatted: Font: 10 pt
Formatted: Font: 10 pt
Formatted: Font: 10 pt
Formatted: Font: 10 pt
Formatted: Font: 10 pt
Formatted: Font: 10 pt
Formatted: Font: 10 pt
Formatted: Font: 10 pt
Formatted: Font: 10 pt
Formatted: Font: 10 pt
Formatted: Indent: First line: 2 ch, Line spacing: 1.5 lines

hydrograph curves of stream and karst spring, attributed to irregular pore media impeding groundwater

flow and reducing discharge. In the VGM model, decreasing m values (equivalent to increasing n)

836

838 enhance pore structure irregularity, similarly lowering hydrograph curves. As shown in Fig. 10(c), 839 epikarst discharge increases with higher n values due to its low permeability (K0) during relative 840 permeability correction, facilitating enhanced groundwater discharge through epikarst to the stream. 841 From Figs. 10(d) and (e), larger n values correspond to decreased epikarst-stream discharge and 842 increased downward recharge to porous media, thereby enhancing stream recharge from PM I and II. 843 Integrating Figs. 10(c) and (e), reduced epikarst-stream hydrographs with higher n values lead to 844 diminished stream-porous media recharge. Fig. 10(f) demonstrates that PM III is primarily influenced by 845 conduit flow and shows minimal sensitivity to n and m parameters. 846 Fig. 10(d.1) displays saturation variations derived from two karst groundwater retention models: 847 Brooks-Corey (BC) model (Equations (20)-(21)) and van Genuchten-Mualem (VGM) model (Equations 848 (22)-(23)). For identical infiltration periods, BC model predicts higher moisture retention than VGM. 849 The BC model emphasizes static water retention in karst media, while VGM prioritizes dynamic 850 groundwater transport and distribution. The VGM model predicts longer groundwater migration 851 distances, suggesting greater sensitivity in simulating karst groundwater diffusion and infiltration 852 processes. These differences hold significance for unsaturated two-phase flow dynamics and accurate 853 prediction of groundwater migration paths in karst aquifer systems. 854 Furthermore, discrepancies exist between BC and VGM models in simulating saturation variations 855 (Fig. 10(d.1)), manifesting as distinct saturation degrees and groundwater migration distances under 856 identical conditions. Therefore, selecting appropriate models based on lithological characteristics is 857 crucial for precise description and prediction of two-phase flow in karst groundwater systems. 858

3.4. Impact of multi-stage permeability and porosity arrangement on the interaction processbetween the karst aquifer and stream

859

860

861

862

863

864

865

By comparing the effects of multi-level versus single-level conduit configurations on interactive processes, the adoption of both multi-level and single-level conduits in the karst conduit system and underlying media did not induce significant changes in the hydrological processes of the epikarst and porous media (I, II) (Fig. 11). By comparing the effects of multi-level and single conduit arrangements on the interaction process, it is found that using multi-level and single conduit arrangements in underlying media does not cause significant changes in the hydrological processes of the epikarst and porous media

Formatted: b2

Formatted: Font: 10 pt

Formatted: Indent: First line: 2 ch, Line spacing: 1.5 lines, Use Asian rules to control first and last character

(PM I and PM II, Fig. 7). As shown in Fig. 7Fig. 11a, when multi-level conduit arrangements are adopted, the peak of stream hydrological process increases, indicating that multi-level conduit arrangements enhance the recharge volume of stream. However, during the recession phase, the flow under multi-level conduit arrangements is relatively low. This is because multi-level conduit collects a proportion of the flow that should have been contributed by the later stage matrix recession and discharge it to stream, thereby affecting the peak of the recession process. As shown in Fig. 7Fig. 11b, under multi-level conduit arrangements, sinkhole can absorb more water and discharge it through karst conduit. This indicates that multi-level conduit arrangements can more effectively play their roles in water absorption and discharge during heavy precipitation events. However, in the case of lower precipitation intensity in the early stage, the water absorption priority of multi-level conduit is not fully manifested. By comparing Figs. 7e11c, 7d11d, and 7e11e, it is found that multi-level conduit arrangements have no significant impact on the hydrological processes of the epikarst and porous media (PM I and PM II). This suggests that multilevel conduit arrangements mainly affect the interaction between the karst conduit and stream, with relatively little impact on other media. The hydrological responses of the karst conduit and PM II under multi-level conduit arrangements are shown in Figs. 7f-11f and 7b11b. Under multi-level conduit arrangements, the discharge volume of the karst conduit significantly increases. At the same time, due to the increase in karst conduit flow, PM II also receives more recharge, leading to a corresponding increase in the discharge volume of this portion of porous media to stream. This further indicates that multi-level conduit configurations can notably influence the hydrological processes of stream and karst conduit under specific precipitation intensities, with minimal effects on other media.

# 4- Uncertainty Analysis and Discussion

866

867

868

869

870

871

872

873

874

875

876

877

878

879

880

881

882

883

884

885

886

887

888

889

890

891

The multi-level conduit configuration inherently affects multi-media interactions by simultaneously altering permeability, conduit diameter, and porosity parameters. This study will further conduct sensitivity analyses on individual variables to investigate their impacts on the vulnerability of karst aquifer systems.

Formatted: Font: (Asian) Times New Roman, 10 pt, Font color: Black, English (United Kingdom), Kern at 三号

Formatted: Level 1, Space Before: 24 pt, After: 12 pt, Line spacing: single, Widow/Orphan 12 pt, Line spacing: scontrol, Keep with next

Formatted: Font: 10 pt

Formatted: Indent: First line: 2 ch, Line spacing: 1.5 lines

893 and Geometry on Interactions Between Karst Aquifer Systems and Streams 894 Fig. 12 presents hydrographs under conditions of circular conduits with varying radii (r=0.2, 0.3, 895 0.3, and 0.5 m) and square-section conduits (r=0.5 m) for (a) stream-connected flow, (b) karst spring 896 discharge, (c) epikarst flow, (d) porous medium I (PM I), (e) PM II, and (f) PM III. Fig. 12(c.1) illustrates 897 different conduit cross-sectional shapes to analyze their impacts on the interactive flow between karst 898 aquifer systems and adjacent streams. 899 As shown in Fig. 12(a), larger conduit radii correspond to higher initial discharge peaks and shorter 900 peak arrival times, indicating enhanced porous medium recharge and faster fluid transmission through 901 larger conduits. Notably, the square-section conduit (s-r<sub>a</sub>=0.5) exhibits higher peak discharge than its 902 circular counterpart (rc=0.5) due to its surplus cross-sectional area accommodating greater fluid 903 discharge under identical nominal radii. 904 Fig. 12(b) demonstrates that karst spring peak discharge increases with conduit radius. At r=0.5 m, 905 the square-section conduit (s-r<sub>0</sub>=0.5) achieves higher peak discharge than the circular conduit (r<sub>0</sub>=0.5), 906 but displays lower recession flow. This occurs because identical precipitation infiltration recharge leads 907 to greater porous medium storage depletion during peak periods in square conduits, subsequently 908 reducing porous medium-to-conduit recharge during baseflow recession. 909 Combined analysis of Figs. 12(c), (d), and (e) reveals that conduit radius variations do not 910 significantly affect epikarst hydrographs or PM I/II hydrographs. However, square-section sinkholes 911 modify flow patterns: epikarst hydrographs show lower values under square conduits, while PM I/II 912 hydrographs exhibit higher values due to enhanced epikarst groundwater collection in square cross-913 sections, increasing recharge to PM I/II. 914 Fig. 12(e) indicates that larger conduit radii correspond to lower negative values. Combined with 915 Fig. 12(a), this demonstrates that increased stream recharge through larger conduits elevates both stream 916 peak discharge and water levels, thereby enhancing porous medium-stream interactions. Similarly, Fig. 917 12(f) shows that larger conduit radii increase karst spring discharge and PM III hydrograph elevation 918 through enhanced gravity-driven groundwater recharge. 919 Conduit geometry (radius and shape) constitutes a critical factor in karst aquifer hydrological

4.1 Comparison with the simulation results of MODFLOW - CFP4.1 Impacts of Conduit Diameter

892

Formatted: b2

Formatted: Font: 10 pt, Not Bold

Formatted: Indent: First line: 2 ch, Line spacing: 1.5 lines, Don't use Asian rules to control first and last character

Formatted: Font: 10 pt, Not Bold, Subscript

Formatted: Font: 10 pt, Not Bold

Formatted: Font: 10 pt, Not Bold, Subscript

Formatted: Font: 10 pt, Not Bold

Formatted: Font: 10 pt, Not Bold, Subscript

Formatted: Font: 10 pt, Not Bold

modeling. Larger circular conduits accelerate peak discharge arrival and amplify stream-connected flow peaks and karst spring discharge. Square-section conduits outperform circular equivalents in peak discharge capacity under identical nominal radii due to cross-sectional area advantages. Enlarged conduits intensify porous medium-stream interactions and amplify PM III recharge through gravitational effects. Comprehensive consideration of conduit geometry impacts on hydrological elements is essential for improving model accuracy and reliability in simulating karst aquifer-stream interaction processes.

920

921

922

923

924

925

926

927

928

929

930

931

932

933

934

935

936

937

938

939

940

941

942

943

944

945

946

947

4.2 Influence of Permeability on the Interaction Processes Between Karst Aquifer Systems and Streams

The permeability of the epikarst directly controls the ease of fluid infiltration from the surface intothe conduit system. Fig. 13 illustrates the hydrological process curves under different epikarst
permeability coefficients ( $K_E=10^{-6}$ ,  $10^{-7}$ ,  $10^{-8}$ ,  $10^{-9}$ ; when  $K_E=10^{-9}$ , the permeability matches that of
porous media, rendering the epikarst incapable of rapid groundwater leakage) for: (a) stream, (b) karst
spring, (c) epikarst, (d) PM I, (e) PM II, and (f) PM III. This aims to reveal how epikarst permeability
regulates groundwater flow patterns in complex conduit systems and intermedia interactions.

As shown in Fig. 13(a), under high epikarst permeability ( $K_{\rm F}=10^{-6}$ ): the discharge curve rises rapidly to a peak of ~4.5  $m^3/s$ , followed by a sharp decline. This indicates that high permeability enables rapid groundwater leakage from the epikarst to the stream, causing swift flow increases. Peak stream discharge diminishes with decreasing permeability. High permeability reduces flow resistance, facilitating faster fluid entry into the conduit system and generating sharp discharge peaks, while low permeability increases resistance, resulting in gradual fluid release and broader, lower discharge curves.

Fig. 13(b) demonstrates that epikarst permeability differences from porous media have minimal impact on conduit flow. However, when epikarst permeability equals that of porous media ( $K_E=10^{-9}$ ), the peak discharge at the karst spring decreases while maintaining identical baseflow recession characteristics. Combining Figs. 13(c) and (c.1), higher epikarst permeability enhances lateral discharge to the stream. At  $K_E=10^{-9}$ , gravitational forces dominate vertical recharge to lower media without lateral discharge.

Fig. 13(d) reveals decreasing discharge from Porous Medium I to the stream with reduced epikarst permeability. Cross-referencing Figs. 13(a) and (e), lower epikarst permeability reduces both stream

Formatted: b2

Formatted: Font: 10 pt, Not Bold

Formatted: Indent: First line: 2 ch, Line spacing: 1.5 lines, Don't use Asian rules to control first and last character

Formatted: Font: 10 pt, Not Bold, Subscript

Formatted: Font: 10 pt, Not Bold

Formatted: Font: 10 pt, Not Bold, Subscript

Formatted: Font: 10 pt, Not Bold

Formatted: Font: 10 pt, Not Bold, Subscript

Formatted: Font: 10 pt, Not Bold

Formatted: Font: 10 pt

Formatted: Font: 10 pt, Not Bold

Formatted: Font: 10 pt, Not Bold, Subscript

Formatted: Font: 10 pt, Not Bold

Formatted: Font: 10 pt, Not Bold, Subscript

Formatted: Font: 10 pt, Not Bold

discharge and water level, limiting recharge to Porous Medium II. Fig. 13(f) shows negligible epikarst permeability influence on Porous Medium III's hydrograph.

948

949

950

951

952

953

954

955

956

957

958

959

960

961

962

963

964

965

966

967

968

969

970

971

972

973

974

975

Epikarst permeability constitutes a critical factor in hydrological modeling of karst aquifer systems. Highly permeable epikarst produces rapid streamflow peaks followed by sharp declines, reflecting efficient groundwater leakage to the stream. Conversely, low permeability yields diminished peaks and broader discharge curves. While karst spring discharge remains relatively stable when epikarst permeability differs from porous media, proper characterization of epikarst permeability is essential for accurately simulating hydraulic interactions between media, regulating groundwater flow pathways and velocities. This enhances model reliability in capturing complex flow dynamics within karst conduitstream systems.

## 4.3 Influence of Porosity on the Interaction Between Karst Aguifer Systems and Adjacent Streams

Fig. 14 presents the hydrographic process curves under different porosity conditions ( $\varphi$ =0.4,  $\varphi$  =0.3.  $\varphi = 0.2$ ,  $\varphi = 0.1$ ) for (a) stream, (b) karst spring, (c) epikarst, (d) PM I, (e) PM II, and (f) PM III. Fig. 14(c.1) illustrates the schematic diagram of groundwater flow under different pore sizes. The study aims to elucidate how porosity regulates fluid flow patterns in complex conduit systems.

As shown in Fig. 14(a), lower porosity results in higher flow peaks and earlier peak times. This occurs because reduced pore space limits groundwater storage capacity, forcing excess water to discharge rapidly and elevating the stream hydrograph. Fig. 14(b) demonstrates that lower porosity drives groundwater to preferentially flow through karst conduits and discharge at springs. In Fig. 14(c), the peak discharge of epikarst at  $\varphi = 0.4$  slightly exceeds those at  $\varphi = 0.3$ ,  $\varphi = 0.2$ , and  $\varphi = 0.1$ .

Fig. 14(d) reveals that at  $\varphi$  =0.1, the storage capacity of porous medium I reaches critical limits. Groundwater recharged from epikarst to porous medium I is rapidly discharged, resulting in significantly higher discharge rates compared to  $\varphi = 0.3$ ,  $\varphi = 0.2$ , and  $\varphi = 0.1$ . Fig. 14(e) indicates increased discharge from porous media to the stream as porosity decreases. Combined with Fig. 14(a), reduced porosity enhances stream stage and discharge but diminishes the stream's ability to recharge porous media due to limited storage capacity. Fig. 14(f) shows negligible porosity effects on the hydrograph of porous medium III, as its behavior is primarily governed by conduit flow.

In hydrological modeling, porosity parameters must be calibrated to accurately simulate

Formatted: b2

Formatted: Font: 10 pt

Formatted: Indent: First line: 2 ch, Line spacing: 1.5 lines, Don't use Asian rules to control first and last character

groundwater flow paths and storage-release dynamics. For low-porosity regions, models should emphasize rapid drainage capacity of conduit systems and transient flow variations. In high-porosity areas, considerations should include fluid retention risks, stream-porous media interactions, and their long-term impacts on geological stability and water resource allocation. Proper porosity parameterization enhances simulation accuracy for diverse hydrological processes, enabling improved prediction and management of karst water resources.

Karst hydrological vulnerability manifests prominently through rapid infiltration, epikarst runoff, groundwater table fluctuations, and abrupt spring discharge variations. The DBS model effectively simulates multi-media interactions during extreme recharge events, enabling temporal analysis of media-stream exchanges, identification of peak interaction values, and applications in coupled conduit flow-seepage processes for two-phase flow systems.

To better assess the applicability of the Darcy-Brinkman-Stokes model in simulating the interaction between the karst aquifer and stream, this study compares its simulation outcomes with those from MODFLOW CFP. As depicted in Fig. 10(a.1), the study contrasts the coupling approaches of conduits and porous media in both MODFLOW CFP and the Darcy-Brinkman-Stokes model, focusing on control equations and grid discretization. In the MODFLOW-CFP model, the groundwater flow during the interaction process is determined by the stable water levels between the conduit-porous media and stream-porous media interfaces (Fig. 10(a.2)). In the Darcy-Brinkman-Stokes model, however, the groundwater interaction among the conduit, the stream, and the porous media depends on the saturation and pressure differences between adjacent grid points. It allows the groundwater interaction among the conduit, the stream, and the porous media to be recharged or discharged simultaneously at different positions. However, this also requires calculating the changes in all grid fluxes (Fig. 10(a.3)).

This study further compares the interaction modes between the stream and porous media in MODFLOW-CFP and Darcy Brinkman Stokes. In MODFLOW-CFP, the stream is discretized among single grid cells. The interaction volume between the stream and porous media depends on the water level difference between them. The fluctuating water surface of the stream is generalized to a unified water level value, and the "dry area" cannot be simulated in the porous media area (as shown in Fig. 10(a.4)). In Darcy-Brinkman-Stokes, the modeling of each medium is completed by specifying the specific porosity and permeability at each grid node. At the interface, the values are interpolated to the average grid cell value based on the values between nodes. Therefore, the interaction interface where the conduit is directly connected to the stream does not need the porous

Formatted: Font: (Asian) Times New Roman, 10 pt, Bold, Font color: Black, English (United Kingdom), Kern at 三号

Formatted: Level 1, Space Before: 24 pt, After 12 pt, Line spacing: single, Widow/Orphan control, Keep with next

media as an intermediate. On this basis, the shape of the stream can be established as a regular rectangle or an irregular channel. The Darcy-Brinkman-Stokes simulates the free flow by reconstructing the water-vapor interface tracer through the VOF (Volume of Fluid) and Front-tracking methods. Therefore, when the grid is fine enough, it can simulate the fluctuating water-vapor interface (as shown in Fig. 10(a.5)).

1009

1010

1011

1012

1013

1014

1015

1016

1017

1018

1019

1020

1021

1022

1023

1024

1025

1026

1027

1028

1029

1030

1031

1032

1033

1034

1035

1036

1037

1038

1039

1040

1041

1042

1043

1044

1045

1046

This study further reveals the interaction mode of groundwater between the conduit and stream in the Darcy-Brinkman-Stokes model and the differences from the simulation results of MODFLOW-CFP through a generalized karst aquifer. As shown in Fig. 11, the karst conduit is surrounded by porous media and are directly connected to the stream. The aquifer is 200 m long, 200 m wide, and 30 m thick. As shown in Fig. 11(a.1), groundwater is replenished from the porous media to the conduit and discharged into the stream. The model parameters are as follows: assume that the porous media is a homogeneous medium with a hydraulic conductivity of 0.65 m/s. The interaction parameter of the conduit wall is 25 m/s, the conduit diameter is 1 m, the conduit roughness is 0.01 m, and the conduit outlet and the stream are in the same grid cell, and the interaction is simulated through the porous media. The initial spring flow is set to zero, the initial head of the porous media is also set to 10 m, and the vertical height of the conduit node is 1 m. The groundwater temperature in the conduit is set to 20 °C, and the surrounding boundaries are noflow boundaries. The upper boundary is a rainfall boundary (Equation 16), where b = 5. According to Huang et al. (2024),  $\mu$ ,  $\sigma^2$ , and  $\alpha$  are set as constants (90, 1.5, and 20) respectively. The total simulation period is 25000 s. In the MODFLOW-CFP model, each stress period is set to 1 minute, and in the Darcy-Brinkman-Stokes model, due to the Courant number limitation, each time step is less than 0.1 s.

Through a comparative analysis of the simulations of MODFLOW-CFP and Darcy-Brinkman-Stokes (the simulated hydrograph of the stream in the Darcy-Brinkman-Stokes model in Fig. 3(b)), as shown in Fig. 11(a.2), there are three differences in the simulation results between the MODFLOW-CFP model and the Darcy-Brinkman-Stokes model: (1) The hydrograph of the stream in the MODFLOW-CFP model lags behind the Darcy-Brinkman-Stokes model in terms of rising. This is because in the Darcy-Brinkman-Stokes model, the rapid lateral runoff of epikarst eauses the hydrograph of the stream to rise rapidly. (2) The peak discharge of the Darcy-Brinkman-Stokes model is slightly lower. This is because a part of the storage capacity of the porous medium has been drained by the rapid lateral runoff of epikarst. By using the rainfall directly infiltrating into the stream (P -River) to represent the time nodes of the rainfall peak and comparing it with the time nodes of the peak discharge of the stream simulated by MODFLOW-CFP and Darcy-Brinkman-Stokes, it is found that both MODFLOW-CFP and Darcy-Brinkman-Stokes exhibit a lag of 2000 s in the rainfall peak. (3) In the Darcy-Brinkman-Stokes model, the rapid lateral runoff of epikarst reduces the storage capacity of the upper porous medium. Therefore, during the initial base flow recession stage, the discharge of the stream in the Darcy-Brinkman-Stokes model is lower than the simulated value of MODFLOW-CFP. As the storage

capacity of the porous medium gradually decreases, the influence of epikarst gradually weakens, and the recession amounts of the two tend to be the same.

4.2 Dynamic interaction processes among various media

Through a comparative analysis of the hydrographs of the stream simulated by MODFLOW-CFP4 model and the Darcy-Brinkman-Stokes model, it is found that the two models have similar effects in simulating the interaction between the karst aquifer and stream under rainfall infiltration recharge. However, with its fine grid and two phase flow simulation capabilities, the Darcy-Brinkman-Stokes model can accurately capture the interaction processes among various media, such as between the saturated and unsaturated zones at various stages under the influence of the dynamic saturation process, and between the conduit and the stream, under rainfall infiltration recharge.

As shown in Fig. 12, the Darcy-Brinkman-Stokes model clearly demonstrates the changes in the saturation levels of epikarst, porous media, and the karst spring; the saturation fields and the interaction between various media at 4000 s, 6105 s, and 7363 s; the interaction amounts between epikarst, porous media I, II, III, and the stream. From Fig. 12 (a.1), it can be seen that the saturation level of epikarst rises and declines earliest, but the saturation level is relatively low, and it is in a completely unsaturated flow state. Porous media I and III rise synchronously before 5000 s, while porous media II and the karst spring rise rapidly at 4611 s. At 7409 s, the karst spring and porous media I successively enter the decline stage. Due to the rapid drainage of the conduit, the saturation level decreases. The saturation level of the karst spring decreases faster than that of porous media I and intersects with porous media I at 9670 s.

Combining Fig. 12 (a.2) with other sub-figures, the stages with obvious interactions among porous media can be divided into the infiltration stage (green), the overflow stage (red), and the recession stage (blue). During the infiltration stage from 4000 s to 4611 s, as shown in Fig. 12 (a.2.1), epikarst vertically replenishes porous medium Land infiltrates downward. However, the infiltrating water does not reach the lower media. Meanwhile, the saturation levels of porous media II, III, and the conduit gradually increase (see Fig. 12 (a.1)). Combining with Fig. 12 (a.3), it can be seen that epikarst laterally replenishes the stream, and quickly drops to the bottom of the riverbed due to gravity. At this time, the lower aquifer system (porous media II, III, and the conduit) is in a dry state, so the stream replenishes the lower aquifer. The amount of recharge received by porous medium III and the conduit is less than that of porous medium II (analyzed by combining Fig. 12 (a.3) and (a.4)), but their saturation levels increase faster. There are two reasons for this situation: First, the bottom elevation of the conduit is 1 m, and the water level of the stream needs to submerge the 1 m water level before it can recharge the conduit. Second, porous medium III is not only replenished by the stream, but also the sinkhole diverts the groundwater in epikarst and porous medium I to the conduit (the sinkhole flow velocity and saturation as shown in Fig. 12 (a.2.1)), and then replenishes porous medium III. As the lower aquifer media gradually tends to be saturated

Formatted: Normal, Level 1, Space Before: 24 pt, After: 12 pt, Keep with next

Formatted: Level 1, Indent: First line: 0 ch, Space Before: 24 pt, After: 12 pt, Line spacing: single, Widow/Orphan control, Keep with next

with rainfall recharge, as shown in Fig. 12 (a.2.2), porous media II and III tend to be saturated (see Fig. 12 (a.2.1)). Due to the weak compressibility of water, after the upper part infiltrates and replenishes porous medium I, it tends to laterally replenish the stream from the interface between porous medium II and stream. As the saturation level of porous medium I gets higher, the lateral recharge to the stream becomes more significant, showing an obvious overflow state. The depression between the two peaks is caused by the rapid rise of the stream water level. During the flood peak stage, the discharge from porous media to stream decreases. At the same time, the rise of the stream water level makes it difficult for the lower porous media to replenish the stream, and porous medium II tends to be saturated, making it difficult to replenish porous medium I. During this stage, the flow between porous media I and II is in a dynamic equilibrium state. As shown in Fig. 12 (a.2.3), during the recession stage, the rainfall infiltration intensity decreases rapidly. Under the action of gravity, the groundwater vertically replenishes porous medium I, the conduit, and porous medium II successively recedes. And the water level of the stream drops rapidly (see Fig. 3 (e)). The groundwater tends to be discharged to the stream through porous medium I and the karst spring. Porous medium I is replenished by porous medium II on the one hand and discharges to the stream on the other hand. Therefore, during a single rainfall event, during the infiltration stage, part of the amount of water replenished from epikarst to the stream is discharged, and other part is redirected to replenish the lower porous media; during the overflow stage, the stream is mainly replenished through the karst conduit and porous medium II. Porous medium I and the stream are in a dynamic equilibrium state. During the recession stage, the porous media act as the main medium to replenish the stream.

1084

1085

1086

1087

1088

1089

1090

1091

1092

1093

1094

1095

1096

1097

1098

1099

1100

1101

1102

1103

1104

1 105

1106

1107

1108

1109

1110

1111

1112

1113

1114

1115

1116

1117

As shown in Fig. 12 (a.4), the karst spring reaches its peak at 7409 s. This is due to the rainfall infiltration, the recharge from porous medium I, and the subsequent discharge to the stream. As the storage volume decreases, the amount of recharge from the karst spring to the stream decreases. A trough appears at 11642 s. This is because as the water level of the stream drops, groundwater is more easily discharged into the stream. However, as the overall storage volume continues to decline, after a peak appears at 13057 s, it enters a complete recession stage. Affected by the decline of the stream water level, the discharge from porous medium III to the stream gradually increases during the recession stage. Combining with Fig. 12 (a.1), it can be seen that while porous medium III is discharging, its saturation remains at level I continuously, indicating that the conduit continuously supplies water vertically to porous medium III.

Under the recharge of rainfall infiltration, the interaction process between the karst aquifer affected by epikarst, sinkholes, conduit and the stream shows dynamic changes in terms of staged characteristics, main interaction media, and the dynamic equilibrium process among different

media. The accurate simulation of the above complex processes depends on the support of a threedimensional two phase numerical model (Dayer Brinkman Stakes model).

## 5. Conclusions

1118 1119

1120

1121

1122

1123

1124

1125

1126

1127

1128

1129

1130

1131

1132

1133

1134

1135

1136

1137

1138

1139

1140

1141

1142

1143

1144

1 145

This study employed the Darcy-Brinkman-Stokes equation to characterize groundwater flow in the karst aquifer and stream, as well as within the karst media. The VOF phase change method was used to illustrate the two-phase flow of water and air in porous media, while various water retention models were applied to describe the unsaturated flow processes in the karst aquifer. The results indicate that changes in precipitation intensity have a significant impact on the interaction between the karst aquifer and stream. As the precipitation intensity increases, the interaction process between the two becomes more complex, involving multi-media synergistic recharge and dynamic interaction with the karst aquifer. The contribution ratios of the epikarst, upper layer, and PM II to the stream change with increasing precipitation intensity. In the early stages of precipitation, the recharge effects of each medium on the stream are relatively balanced; as the precipitation intensity increases, the discharge volumes of PM I and PM II both increase, especially the increase in PM II is more significant, and the timing of its discharge peak advances; when the precipitation intensity further increases, PM II gradually reaches saturation, limiting its discharge capacity; and during this process, the double peak intensity of PM I changes with the precipitation intensity; at the same time, due to the saturation of PM II, a more pronounced overflow phenomenon occurs in PM I, which dominates the contribution of recharge volume to the stream. Therefore, the change in precipitation intensity not only affects the discharge volume and discharge peak of each medium in the karst aquifer but also is influenced by the dynamic saturation process of adjacent media. By analyzing the modeling differences between MODFLOW-CFPv2 and DBS for the conceptualized model of this study and conducting comparative validation through stream hydrographs, results demonstrate that the DBS model can effectively simulate the interaction process between karst aquifer systems and adjacent streams under precipitation influences, while refining twophase interactive flows between different media subjected to dynamic saturation processes. Under two consecutive precipitation events, total rainfall intensity directly governs stream water level variations. Different rainfall intensities induce distinct changing trends in stream water levels.

Formatted: Font: 10 pt

Formatted: Indent: First line: 2 ch, Line

pacing: 1.5 lines

which subsequently influences stream water level changes in the second rainfall period. Due to the rapid drainage characteristics of karst conduits, the storage capacity of conduits during the first rainfall period shows negligible impact on storage during the second rainfall period. When the first rainfall intensity exceeds the second, stream water level fluctuations exhibit smaller amplitudes, and vice versa. Variations in stream water levels can alter the recharge potential from different layered media in the karst aquifer system to the stream. Different water retention models also demonstrate significant impacts on hydrological processes in both the stream and various media. The accuracy of two-phase flow simulation in the DBS model was validated against benchmark experiments from two literature sources. The VGM model causes greater water retention in porous media, thereby reducing stream discharge.

1 173

During heavy rainfall events, multi-level conduit configurations significantly affect interaction processes between karst aquifer systems and adjacent streams, demonstrating higher drainage efficiency. However, such configurations exhibit relatively minor impacts on other media, indicating that multi-level conduit arrangements primarily influence hydrological processes by regulating interactions between karst conduits and the stream.

In uncertainty analysis: For circular conduits, larger diameters result in higher initial peak discharge in streams and shorter time-to-peak, with corresponding increases in peak discharge from karst springs.

Under identical diameters, square-section conduits demonstrate higher peak stream discharge and karst spring discharge than circular counterparts due to surplus space advantages. Epikarst permeability significantly influences hydrological processes in karst aquifer systems. High-permeability epikarst produces rapid stream discharge peaks followed by steep recessions. With decreasing permeability, peak stream discharge diminishes and hydrographs become lower and broader. Concurrently, karst spring peak discharge decreases, with epikarst only vertically recharging underlying media without lateral discharge. Reduced epikarst permeability decreases discharge from porous media to streams.

Porosity proves crucial in governing hydrological processes of karst aquifer systems: Lower porosity leads to higher and earlier discharge peaks in both streams and karst springs, as reduced pore spaces limit groundwater storage and force faster drainage. Higher porosity results in lower peaks and broader hydrographs. Decreasing porosity increases discharge from porous media to streams but reduces the stream's recharge capacity to porous media due to diminished storage space. Hydrological modeling

Formatted: Indent: First line: 2 ch, Line spacing: 1.5 lines, No bullets or numbering

should prioritize rapid drainage and transient flow variations in conduit systems for low-porosity areas, while high-porosity regions require consideration of fluid retention risks, interactive flows between streams and porous media, along with long-term impacts on geological stability and water resource allocation.

The impact of different water retention models on the hydrological processes of the stream

and various media is also quite significant. The VGM model leads to more water being retained in the porous media, thereby reducing the discharge volume of the stream. In the early stage of precipitation, the VGM model enhances the recharge effect of the stream on the karst conduit, but the discharge volume of the karst conduit to the stream is relatively low in the middle and later stages. Additionally, the VGM model predicts shorter movement distances of karst groundwater, weakening the vertical infiltration capacity of the epikarst, resulting in an increase in the discharge volume of the epikarst to the stream. At the same time, based on the VGM model, the discharge volume of PM-I decreases, but due to the smaller recharge volume, lower saturation level, and water level, the stream is more likely to recharge it. The porous media located below the karst conduit mainly rely on the recharge from the conduit, and based on the BC model, the discharge volume of the karst conduit is larger. Ultimately, based on the VGM model, it is found that the stream is more likely to recharge PM-II in the early stage of precipitation; in the middle to late stages of precipitation, the discharge volume predicted by the BC model exceeds that of the VGM model.

Formatted: Font: Bold

interaction process between the karst aquifer and stream, and exhibit higher discharge

During heavy precipitation events, multi-level conduit arrangements can significantly impact

efficiency. However, this arrangement has relatively little impact on other media, indicating that multi-level conduit arrangements primarily influence the hydrological process by regulating the interaction between the karst conduit and stream.

For two consecutive precipitation events, the total precipitation intensity directly affects the changes in water level of stream. Different precipitation intensities result in different trends of water level changes in stream. The porous media of the karst aquifer store a proportion of groundwater during the first precipitation period, which affects the water level changes of stream during the second precipitation period. Due to the rapid discharge characteristics of the karst conduit, the storage volume of the conduit during the first precipitation period has little impact on the storage volume during the second precipitation period. When the intensity of the first precipitation is higher than that of the second, the amplitude of water level changes in stream is smaller, and vice versa. The changes in water level of stream can affect the ease of recharge from different layer media of the karst aquifer to the stream.

Through the generalized karst aquifer, the interaction mode of groundwater between the conduit and stream in the Darcy Brinkman-Stokes model and the differences from the simulation results of MODFLOW-CFP were further revealed. Moreover, a comparative analysis of the two types of models was carried out through the hydrograph of the stream. The results show that the Darcy Brinkman-Stokes model can effectively simulate the interaction process between the karst aquifer and stream under the influence of rainfall, and refine the two-phase interactive flow among various media affected by the dynamic saturation process. At the same time, the Darcy-Brinkman-Stokes model can represent the dynamic interaction process affected by epikarst, sinkholes,

1217	conduit and the stream under the recharge of rainfall infiltration, and refine and explain the	
1218	significant infiltration process, overflow process and recession process.	
1219	Acknowledgments	Formatted: Font: Bold, English (United Kingdom)
		Formatted: English (United Kingdom) Formatted: b1
1220	aThis research was partially funded by the Doctoral Scientific Research Startup Foundation of Xinjiang	 Formatted: Font: 10 pt
1221	University grant 620321004, and the Natural Science Foundation of Xinjiang Uygur Autonomous Region	
1222	grant 2022D01C40.	
1223		
1024	Determined by the All constants and the second state of the second	
1224	Data availability. All raw data can be provided by the corresponding author upon request.	
1225		
1223		
1226	Author contributions. FH: conceptualization, methodology, formal analysis, visualization, writing	
1227	original draft. YG: conceptualization, methodology, formal analysis, visualization, review and editing.	
1228	ZZ: methodology, formal analysis, visualization, review and editing. XH: visualization, review and	 Formatted: Font: 10 pt
1229	alities VVV. mothedalars, arriver and alities CD, matrice anichal des the advantage and alities	
1229	editing. XW: methodology, review and editing. SP: writing original draft and review and editing.	
1230		
1231	Competing interests. The authors declare that they have no conflict of interest.	
1232		
1233	Deferences	Formatted: Font: (Asian) Times New Roman, 10 pt.
1233	References	Bold, Font color: Black, English (United
1234	Z. Li, X. Xu, M. Liu, et al.State-space prediction of spring discharge in a karst catchment in Southwest	Kingdom), Kern at 三号 Formatted: Normal, Level 1, Space Before: 24 pt,
1235	China I Hydral 540 (2017) pp. 264 276 10 1016/Fibral 2017 04 001	After: 12 pt, Keep with next
	ChinaJ. Hydrol., 549 (2017), pp. 264-276, 10.1016/j.jhydrol.2017.04.001	
1236	Ford, D., & Williams, P. (2007). Karst hydrogeology and geomorphology. West Sussex, England: John	
1237	Wiley & Sons Ltd. https://doi.org/10.1002/9781118684986	
I		

V. Sivelle, H. Jourde, D. Bittner, N. Mazzilli, Y. Tramblay. Assessment of the relative impacts of climate 1239 changes and anthropogenic forcing on spring discharge of a Mediterranean karst system. J. Hydrol., 598 1240 (2021), Article 126396, 10.1016/j.jhydrol.2021.126396 1241 J. Longenecker, T. Bechtel, Z. Chen, et al. Correlating global precipitation measurement satellite data 1242 with karst spring hydrographs for rapid catchment delineation. Geophys. Res. Lett., 44 (10) (2017), pp. 1243 4926-4932, 10.1002/2017gl073790 1244 Goldscheider, N., Chen, Z., Auler, A.S., Bakalowicz, M., Broda, S., Drew, D., Hartmann, J., Jiang, G., 1245 Moosdorf, N., Stevanovic, Z., Veni, G., 2020. Global distribution of carbonate rocks and karst water 1246 resources. Hydrgeol. J. 28 (5), 1661–1677. 1247 B.J. Mahler, Y. Jiang, J. Pu, J.B. Martin. Editorial: advances in hydrology and the water environment in 1248 the karst critical zone under the impacts of climate change and anthropogenic activities. J. Hydrol., 595 1249 (2021), Article 125982, 10.1016/j.jhydrol.2021.125982 1250 Kuniansky, E.L., 2016. Simulating groundwater flow in karst aquifers with distributed parameter 1251 models - Comparison of porous-equivalent media and hybrid flow approaches: U.S. Geological Survey 1252 Scientific Investigations Report 2016-5116, pp. 14. doi:https://doi.org/10.3133/sir20165116 1253 L. Zhang, M. Luo, Z. Chen. Identification and estimation of solute storage and release in Karst water 1254 systems, south China. Int. J. Environ. Res. Public Health, 17 (2020), pp. 1-13, 10.3390/ijerph17197219 1255 Bonacci, O., 2015. Surface Waters and Groundwater in Karst. Z. Stevanović (ed.), Karst Aquifers -1256 Characterization and Engineering, Professional Practice in Earth Science. Springer International 1257 Publishing Switzerland.153-155. 1258 F. Guo, G. Jiang. Hydro-ecological processes of hyporheic zone in a karst spring-fed pool: Effects of 1259 groundwater decline and river backflow. J. Hydrol., 587 (2020), Article 124987, 1260 10.1016/j.jhydrol.2020.124987 1261 Gao, Y., Yao, L., Chang, N.-B., and Wang, D.: Diagnosis toward predicting mean annual runoff in 1262 ungauged basins, Hydrol. Earth Syst. Sci., 25, 945-956, https://doi.org/10.5194/hess-25-945-2021, 2021.

1238

1263

1264

E. Lee, N. Krothe. A four-component mixing model for water in a karst terrain in south-central Indiana,

USA. Using solute concentration and stable isotopes as tracers. Chem. Geol., 179 (2001), pp. 129-143

- 1265 A.M.L.S. Okello, S. Uhlenbrook, G.P.W. Jewitt, I. Masih, E.S. Riddell, V.D.Z. Pieter. Hydrograph
- 1266 separation using tracers and digital filters to quantify runoff components in a semi-arid mesoscale
- 1267 <u>catchment. Hydrol. Process., 32 (10) (2018), pp. 1334-1350</u>
- 1268 L. Duran, N. Massei, N. Lecoq, M. Fournier, D. Labat Analyzing multi-scale hydrodynamic processes
- 1269 in karst with a coupled conceptual modeling and signal decomposition approach J. Hydrol., 583 (2020),
- 1270 Article 124625, 10.1016/j.jhydrol.2020.124625.
- 1271 Bittner, D., Parente, M. T., Mattis, S., Wohlmuth, B., & Chiogna, G. (2020). Identifying relevant
- 1272 <u>hydrological and catchment properties in active subspaces: An inference study of a lumped karst aquifer</u>
- 1273 model. Advances in Water Resources, 135, 103472. https://doi.org/10.1016/j.advwatres.2019.103472
- 1274 S. Bianchini, P. Confuorto, E. Intrieri, P. Sbarra, D. Di Martire, D. Calcaterra, R. Fanti. Machine learning
- 1275 for sinkhole risk mapping in Guidonia-Bagni di Tivoli plain (Rome). Italy. Geocarto International, 37
- 1276 (27) (2022), pp. 16687-16715
- 1277 Halihan, T., R.E. Mace, and J.M. Sharp Jr., 1999. Interpreting flow using permeability at multiple scales.
- 1278 <u>Karst Modeling, Special Publication, 5.</u>
- 1279 Shoemaker, W. B., E. L. Kuniansky, S. Birk, S. Bauer, and E. D. Swain (2008), Documentation of a
- 1280 Conduit Flow Process (CFP) for MODFLOW-2005, US Department of the Interior, US Geological
- 1281 <u>Survey, Reston, Va.</u>
- 1282 A. Kavousi, T. Reimann, R. Liedl, E. Raeisi Karst aquifer characterization by inverse application of
- 1283 MODFLOW-2005 CFPv2 discrete-continuum flow and transport model. J. Hydrol., 587 (2020).
- 1284 <u>10.1016/j.jhydrol.2020.124922</u>
- 1285 Y. Chang, J. Wu, L. Liu Effects of the conduit network on the spring hydrograph of the karst aquifer J.
- 1286 Hydrol., 527 (2015), pp. 517-530.
- 1287 H. Qiu, J. Niu, B.X. Hu Quantifying the integrated water and carbon cycle in a data-limited karst basin
- 1288 <u>using a process-based hydrologic model Environ. Earth Sci., 78 (11) (2019), p. 328</u>
- 1289 Gao, Y., Libera, D., Kibler, K., Wang, D\*, Chang, N.B., 2020. Evaluating the performance of BAM-
- 1290 <u>based blanket filter on nitrate reduction in a karst spring. Journal of Hydrology, 591, 125491. Doi:</u>
- 1291 <u>10.1016/j.jhydrol.2020.125491.</u>

- 1292 Gao, Y., Huang, F., Wang, D. Evaluating physical controls on conduit flow contribution to spring
- 1293 <u>discharge. Journal of Hydrology, 2024. Doi:10.1016/j.jhydrol.2024.130754.</u>
- 1294 G.D. Fiorese, G. Balacco, G. Bruno, N. Nikolaidis. Hydrogeological modelling of a coastal karst aquifer
- 1295 using an integrated SWAT-MODFLOW approach. Environ. Model. Softw., 183 (2025), Article 106249,
- 1296 <u>10.1016/j.envsoft.2024.106249</u>
- 1297 B.A. Yifru, S. Lee, S. Bak, J.H. Bae, H. Shin, K.J. Lim. Estimating exploitable groundwater for
- 1298 agricultural use under environmental flow constraints using an integrated SWAT-MODFLOW model.
- 1299 Agric. Water Manag., 303 (2024), p. 109024
- 1300 Worthington, S. R. (1991), Karst Hydrogeology of the Canadian Rocky Mountains, 227 pp., McMaster
- 1301 Univ., Hamilton, Ont., Canada.
- Huang, F., Gao, Y., Hu, X., Wang, X., & Pu, S. (2024). Influence of precipitation infiltration recharge
- 1303 on hydrological processes of the karst aquifer system and adjacent river. Journal of Hydrology, 639,
- 1304 <u>131656. https://doi.org/10.1016/j.jhydrol.2024.131656</u>
- 1305 J. Dam, R.A. Feddes. Numerical simulation of infiltration, evaporation and shallow groundwater levels
- 1306 with the Richards equation. J. Hydrol., 233 (1–4) (2000), pp. 72-85
- 1307 Soulaine, C., Tchelepi, H.A. Micro-continuum Approach for Pore-Scale Simulation of Subsurface
- 1308 Processes. Transp Porous Med 113, 431–456 (2016). https://doi.org/10.1007/s11242-016-0701-3
- Nillama L.B.A., Yang J., Yang L.An explicit stabilised finite element method for Navier-Stokes-
- 1310 Brinkman equations J. Comput. Phys., 457 (2022), Article 111033, 10.1016/j.jcp.2022.111033
- 1311 F.J. Carrillo, I.C. Bourg, C. Soulaine. Multiphase flow modeling in multiscale porous media: An open-
- 1312 source micro-continuum approach J. Computat. Phys.: X, 8 (2020), Article 100073,
- 1313 <u>10.1016/j.jcpx.2020.100073</u>
- 1314 Yanyan Zhai, David R. Fuhrman, Erik Damgaard Christensen, Numerical simulations of flow inside a
- 1β15 stone protection layer with a modified k-ω turbulence model, Coastal Engineering, Volume
- 1316 <u>189,2024,104469,ISSN 0378-3839,https://doi.org/10.1016/j.coastaleng.2024.104469.</u>
- 1317 A. Nahlieli, T. Svoray, E. Argaman. Piping formation and distribution in the semi-arid Northern Negev
- 1318 environment: a new conceptual model. Catena, 213 (2022), Article 106201,
- 1319 <u>10.1016/j.catena.2022.106201</u>

- 1320 S.-F. Lu, Y.-X. Wang, M.-Y. Ma, L. Xu. Water seepage characteristics in porous media with various
- 1321 <u>conduits: Insights from a multi-scale Darcy-Brinkman-Stokes approach. Computers and Geotechnics,</u>
- 1322 <u>157 (2023), p. 105317</u>
- 1323 Soulaine, C. (2024). Micro-continuum modeling: An hybrid-scale approach for solving coupled
- 1324 processes in porous media. Water Resources Research, 60, e2023WR035908.
- 1325 https://doi.org/10.1029/2023WR035908.
- 1326 T. Reimann, C. Rehrl, W.B. Shoemaker, T. Geyer, S. BirkThe significance of turbulent flow
- representation in single-continuum models Water Resour. Res., 47 (9) (2011), p. W09503
- 1328 del Jesus, M., Lara, J.L., Losada, I.J., 2012. Three-dimensional interaction of waves and porous coastal
- 1329 structures: Part I: numerical model formulation. Coast. Eng. 64, 57–72.
- 1330 <u>https://doi.org/10.1016/j.coastaleng.2012.01.008.</u>
- Higuera, P., Lara, J.L., Losada, I.J., 2014. Three-dimensional interaction of waves and porous coastal
- 1332 structures using OpenFOAM®. Part I: formulation and validation. Coast. Eng. 83, 243-258.
- 1333 <u>https://doi.org/10.1016/j.coastaleng.2013.08.010.</u>
- Bailly-Comte, V., et al., 2010. Water exchange and pressure transfer between conduits and matrix and
- 1\(\beta\)35 their influence on hydrodynamics of two karst aquifers with sinking streams. J. Hydrol. 386 (1-4), 55-
- 1336 <u>66. https://doi.org/10.1016/j.jhydrol.2010.03. 005.</u>
- 1337 Giese, M., Reimann, T., Bailly-Comte, V., Maréchal, J.-C., Sauter, M., Geyer, T., 2018. Turbulent and
- 1338 <u>laminar flow in karst conduits under unsteady flow conditions: in terpretation of pumping tests by</u>
- 1339 discrete conduit-continuum modeling. Water Resour. Res. 54 (3), 1918–1933.
- 1340 https://doi.org/10.1002/2017WR020658.
- 1341 Kuang, X., and J. J. Jiao (2011), A new model for predicting relative nonwetting phase permeability from
- 1342 <u>soil water retention curves, Water Resources Research, 47, W08520, doi:10.1029/2011WR010728.</u>
- 1343 R. Brooks, A. Corey, Hydraulic properties of porous media, Hydro Paper 3, Colorado State University,
- 1344 <u>1964, p. 27.</u>
- Hirt, C.W., Nichols, B.D., 1981. Volume of fluid (VOF) method for the dynamics of free boundaries. J.
- 1346 <u>Comput. Phys. 39, 201–225.</u>

- Rusche, H., 2002. Computational Fluid Dynamics of Dispersed Two-Phase Flows at High Phase
- 1348 Fractions (Ph.D. thesis). Imperial College, London, URL: http://powerlab.fsb.
- 1349 <u>hr/ped/kturbo/OpenFOAM/docs/HenrikRuschePhD2002.pdf.</u>
- 1350 Springer, D. S., Cullen, S. J., & Everett, L. G. (1995). Laboratory studies on air permeability. In L. G.
- 1351 Wilson, L. G. Everett, & S. J. Cullen, Eds., Handbook of Vadose Zone Characterization & Monitoring
- 1352 (pp. 217–247). Boca Raton, FL: CRC Press.
- 1353 Assouline, S., & Or, D. (2013). Conceptual and parametric representation of soil hydraulic properties: A
- 1354 review. Vadose Zone Journal, 12(4), 1–20. https://doi.org/10.2136/vzj2013.07.0121.
- 1355 van Genuchten, M. T. (1980). A closed-form equation for predicting the hydraulic conductivity of
- 1356 <u>unsaturated soils. Soil Science Society of America Journal, 44(5), 892–898.</u>
- 1357 https://doi.org/10.2136/sssaj1980.03615995004400050002x.
- 1358 Mualem, Y. (1976). A new model for predicting the hydraulic conductivity of unsaturated porous
- 1359 media. Water Resources Research, 12(3), 513–522. https://doi.org/10.1029/WR012i003p00513.
- 1360 Parker, J. C., Lenhard, R. J., & Kuppusamy, T. (1987). A parametric model for constitutive properties
- 1361 governing multiphase flow in porous media. Water Resources Research, 23(4), 618–624.
- 1362 Yang, Z., Mohanty, B.P., Tong, X., Kuang, X., Li, L., 2021. Effects of water retention curves and
- 1363 permeability equations on the prediction of relative air permeability. Geophys. Res. Lett. 48 (10)
- 1364 https://doi.org/10.1029/2021GL092459.
- 1365 Reimann, T., Giese, M., Geyer, T., Liedl, R., Maréchal, J.C., Shoemaker, W.B., 2014. Representation of
- 1366 water abstraction from a karst conduit with numerical discrete continuum models. Hydrol. Earth Syst.
- 1367 <u>Sci. 18 (1), 227–241. https://doi.org/10. 5194/hess-18-227-2014.</u>
- 1368 J.J. Gallegos, B.X. Hu, H. Davis. Simulating flow in karst aquifers at laboratory and sub-regional scales
- 1369 <u>using MODFLOW-CFP. Hydrgeol. J., 21 (8) (2013), pp. 1749-1760</u>
- 1370 Y. Chang, J. Wu, G. Jiang, L. Liu, T. Reimann, M. Sauter. Modelling spring discharge and solute
- 1371 <u>transport in conduits by coupling CFPv2 to an epikarst reservoir for a karst aquifer. J. Hydrol., 569 (2019),</u>
- 1372 pp. 587-599, 10.1016/j.jhydrol.2018.11.075

13/3	M. Shiratkan, Z. Mohammadi, A. Kavousi, V. Sivelle, D. Labat, T. Reimann. Toward the estimation of
1374	the transfer coefficient in karst systems: Using baseflow recession coefficient under matrix-restrained
1375	flow regime. J. Hydrol., 620 (2023), Article 129441, 10.1016/j.jhydrol.2023.129441
1376	Barenblatt, G.I., Zheltov, I.P., Kochina, I.N., 1960. Basic concepts in the theory of seepage of
1377	homogeneous liquids in fissured rocks. J. Appl. Math. Mech. 24 (5), 1286–1303.
1378	https://doi.org/10.1016/0021-8928(60)90107-6.
1379	E. Pardo-Igúzquiza, P. Dowd, A.P. Bosch, J.A. Luque-Espinar, J. Heredia, J.J. Durán-Valsero. A
1380	parsimonious distributed model for simulating transient water flow in a high-relief karst aquifer.
1381	Hydrogeol. J. (2018), 10.1007/s10040-018-1825-z
1382	Li, Y.X., Shu, L.C., Wu, P.P., Zou, Z., Lu, C.P., Liu, B., Niu, S.Y., Yin, X.R., 2023. Influence of the
1383	karst matrix hydraulic conductivity and specific yield on the estimation accuracy of karstic water storage
1384	variation. J. Hydrol. 626 (Part A) https://doi.org/10.1016/j.jhydrol.2023.130186. ISSN 0022-1694.
1385	N.Z. Dvory, M. Kuznetsov, Y. Livshitz, G. Gasser, I. Pankratov, O. Lev, E. Adar, A. Yakirevich.
1386	Modeling sewage leakage and transport in carbonate aquifer using carbamazepine as an indicator. Water
1387	Res., 128 (2018), pp. 157-170, 10.1016/j.watres.2017.10.044
1388	Z. Li, X. Xu, M. Liu, et al. State-space prediction of spring discharge in a karst catchm
1389	ent in Southwest ChinaJ. Hydrol., 549 (2017), pp. 264-276, 10.1016/j.jhydrol.201
1390	7.04.001
1391	Ford, D., & Williams, P. (2007). Karst hydrogeology and geomorphology. West Susse
1392	x, England: John Wiley & Sons Ltd. https://doi.org/10.1002/9781118684986
1393	V. Sivelle, H. Jourde, D. Bittner, N. Mazzilli, Y. Tramblay. Assessment of the relative i
1394	mpacts of climate changes and anthropogenic forcing on spring discharge of a M
1395	editerranean karst system. J. Hydrol., 598 (2021), Article 126396, 10.1016/j.jhydr
1396	<del>01.2021.126396</del>
1397	J. Longenecker, T. Bechtel, Z. Chen, et al. Correlating global precipitation measureme

398	nt satellite data with karst spring hydrographs for rapid catchment delineation. Ge
899	ophys. Res. Lett., 44 (10) (2017), pp. 4926-4932, 10.1002/2017gl073790
100	Goldscheider, N., Chen, Z., Auler, A.S., Bakalowicz, M., Broda, S., Drew, D., Hartma
101	nn, J., Jiang, G., Moosdorf, N., Stevanovic, Z., Veni, G., 2020. Global distributio
102	n of carbonate rocks and karst water resources. Hydrgeol. J. 28 (5), 1661–1677.
103	B.J. Mahler, Y. Jiang, J. Pu, J.B. Martin. Editorial: advances in hydrology and the wate
104	r environment in the karst critical zone under the impacts of climate change and a
105	nthropogenic activities. J. Hydrol., 595 (2021), Article 125982, 10.1016/j.jhydrol.
106	<del>2021.125982</del>
107	Kuniansky, E.L., 2016. Simulating groundwater flow in karst aquifers with distributed
804	parameter models Comparison of porous equivalent media and hybrid flow ap
109	proaches: U.S. Geological Survey Scientific Investigations Report 2016 5116, p
110	p. 14. doi:https://doi.org/10.3133/sir20165116
111	L. Zhang, M. Luo, Z. Chen. Identification and estimation of solute storage and release
112	in Karst water systems, south China. Int. J. Environ. Res. Public Health, 17 (202
113	0), pp. 1-13, 10.3390/ijerph17197219
114	Bonacci, O., 2015. Surface Waters and Groundwater in Karst. Z. Stevanović (ed.), Kars
115	t Aquifers — Characterization and Engineering, Professional Practice in Earth Scie
116	nce. Springer International Publishing Switzerland. 153-155.
117	F. Guo, G. Jiang. Hydro-ecological processes of hyporheic zone in a karst spring-fed p
118	ool: Effects of groundwater decline and river backflow. J. Hydrol., 587 (2020), A

419	rtiele 124987, 10.1016/j.jhydrol.2020.124987
420	Gao, Y., Yao, L., Chang, N. B., and Wang, D.: Diagnosis toward predicting mean annu
421	al runoff in ungauged basins, Hydrol. Earth Syst. Sci., 25, 945–956, https://doi.or
122	g/10.5194/hess 25-945-2021, 2021.
423	E. Lee, N. Krothe. A four component mixing model for water in a karst terrain in sout
124	h central Indiana, USA. Using solute concentration and stable isotopes as tracers.
125	-Chem. Geol., 179 (2001), pp. 129-143
426	A.M.L.S. Okello, S. Uhlenbrook, G.P.W. Jewitt, I. Masih, E.S. Riddell, V.D.Z. Pieter.
127	Hydrograph separation using tracers and digital filters to quantify runoff compon
428	ents in a semi-arid mesoscale catchment. Hydrol. Process., 32 (10) (2018), pp. 13
129	<del>34-1350</del>
430	L. Duran, N. Massei, N. Lecoq, M. Fournier, D. Labat Analyzing multi-scale hydrody
431	namic processes in karst with a coupled conceptual modeling and signal decompo
432	sition approach J. Hydrol., 583 (2020), Article 124625, 10.1016/j.jhydrol.2020.12
433	<del>4625.</del>
434	Bittner, D., Parente, M. T., Mattis, S., Wohlmuth, B., & Chiogna, G. (2020). Identifyin
435	g relevant hydrological and catchment properties in active subspaces: An inferenc
436	e study of a lumped karst aquifer model. Advances in Water Resources, 135, 1034
437	72. https://doi.org/10.1016/j.advwatres.2019.103472
438	S. Bianchini, P. Confuorto, E. Intrieri, P. Sbarra, D. Di Martire, D. Calcaterra, R. Fanti.
439	Machine learning for sinkhole risk mapping in Guidonia Bagni di Tivoli plain (R

140	ome). Italy. Geocarto International, 37 (27) (2022), pp. 16687-16715
441	Halihan, T., R.E. Mace, and J.M. Sharp Jr., 1999. Interpreting flow using permeability
142	at multiple scales. Karst Modeling, Special Publication, 5.
143	Worthington, S. R. (1991), Karst Hydrogeology of the Canadian Rocky Mountains, 22
144	7 pp., McMaster Univ., Hamilton, Ont., Canada.
145	Huang, F., Gao, Y., Hu, X., Wang, X., & Pu, S. (2024). Influence of precipitation infilt
146	ration recharge on hydrological processes of the karst aquifer system and adjacen
147	t river. Journal of Hydrology, 639, 131656. https://doi.org/10.1016/j.jhydrol.2024.
148	<u>131656</u>
149	Shoemaker, W. B., E. L. Kuniansky, S. Birk, S. Bauer, and E. D. Swain (2008), Docum
450	entation of a Conduit Flow Process (CFP) for MODFLOW 2005, US Department
451	of the Interior, US Geological Survey, Reston, Va.
452	A. Kavousi, T. Reimann, R. Liedl, E. Raeisi Karst aquifer characterization by inverse a
453	pplication of MODFLOW 2005 CFPv2 discrete continuum flow and transport m
154	odel. J. Hydrol., 587 (2020), 10.1016/j.jhydrol.2020.124922
455	H. Qiu, J. Niu, B.X. Hu Quantifying the integrated water and carbon cycle in a data-li
456	mited karst basin using a process-based hydrologic model Environ. Earth Sci., 78
457	<del>(11) (2019), p. 328</del>
458	Gao, Y., Libera, D., Kibler, K., Wang, D*., Chang, N.B., 2020. Evaluating the perform
159	ance of BAM based blanket filter on nitrate reduction in a karst spring. Journal of
460	Hydrology, 591, 125491. Doi: 10.1016/j.jhydrol.2020.125491.

461	Gao, Y., Huang, F., Wang, D. Evaluating physical controls on conduit flow contributio
462	n to spring discharge. Journal of Hydrology, 2024. Doi:10.1016/j.jhydrol.2024.13
463	<del>0754.</del>
464	Soulaine, C., Tchelepi, H.A. Micro-continuum Approach for Pore-Scale Simulation of
465	Subsurface Processes. Transp Porous Med 113, 431–456 (2016). https://doi.org/1
466	<u>0.1007/s11242 016 0701 3</u>
467	Nillama L.B.A., Yang J., Yang L.An explicit stabilised finite element method for Navi
468	er-Stokes-Brinkman equations J. Comput. Phys., 457 (2022), Article 111033, 10.1
169	016/j.jcp.2022.111033
470	F.J. Carrillo, I.C. Bourg, C. Soulaine. Multiphase flow modeling in multiscale porous
471	media: An open-source micro-continuum approach J. Computat. Phys.: X, 8 (202
472	0), Article 100073, 10.1016/j.jcpx.2020.100073
473	Yanyan Zhai, David R. Fuhrman, Erik Damgaard Christensen, Numerical simulations o
174	f flow inside a stone protection layer with a modified k ω turbulence model,Coas
475	tal Engineering, Volume 189,2024,104469,ISSN 0378-3839,https://doi.org/10.101
476	6/j.coastaleng.2024.104469.
177	A. Nahlieli, T. Svoray, E. Argaman. Piping formation and distribution in the semi-arid-
478	Northern Negev environment: a new conceptual model. Catena, 213 (2022), Artic
179	le 106201, 10.1016/j.catena.2022.106201
480	S. F. Lu, Y. X. Wang, M. Y. Ma, L. Xu. Water seepage characteristics in porous media
481	with various conduits: Insights from a multi-scale Darcy-Brinkman-Stokes appro

1482	ach. Computers and Geotechnics, 157 (2023), p. 105317
1483	Soulaine, C. (2024). Micro-continuum modeling: An hybrid-scale approach for solvin
1484	g coupled processes in porous media. Water Resources Research, 60, e2023WR0
1485	35908. https://doi.org/10.1029/2023WR035908.
1486	T. Reimann, C. Rehrl, W.B. Shoemaker, T. Geyer, S. BirkThe significance of turbulent
1487	flow representation in single continuum models Water Resour. Res., 47 (9) (201
1488	1), p. W09503
1489	del Jesus, M., Lara, J.L., Losada, I.J., 2012. Three-dimensional interaction of waves an
1490	d porous coastal structures: Part I: numerical model formulation. Coast. Eng. 64,
1491	57 72. https://doi.org/10.1016/j.coastaleng.2012.01.008.
1492	Higuera, P., Lara, J.L., Losada, I.J., 2014. Three-dimensional interaction of waves and
1493	porous coastal structures using OpenFOAM®. Part I: formulation and validation.
1494	Coast. Eng. 83, 243–258. https://doi.org/10.1016/j.coastaleng.2013.08.010.
1495	R. Brooks, A. Corey, Hydraulic properties of porous media, Hydro Paper 3, Colorado
1496	State University, 1964, p. 27.
1497	Kuang, X., and J. J. Jiao (2011), A new model for predicting relative nonwetting phase
1498	permeability from soil water retention curves, Water Resources Research, 47, W
1499	<del>08520, doi:10.1029/2011WR010728.</del>
1500	Parker, J. C., Lenhard, R. J., & Kuppusamy, T. (1987). A parametric model for constitu
1501	tive properties governing multiphase flow in porous media. Water Resources Res

1502	earch, 23(4), 618-624.
1503	Y. Chang, J. Wu, L. Liu Effects of the conduit network on the spring hydrograph of the
1504	karst aquifer J. Hydrol., 527 (2015), pp. 517-530.
1505	Li, Y.X., Shu, L.C., Wu, P.P., Zou, Z., Lu, C.P., Liu, B., Niu, S.Y., Yin, X.R., 2023. Infl
1506	uence of the karst matrix hydraulic conductivity and specific yield on the estimati
1507	on accuracy of karstic water storage variation. J. Hydrol. 626 (Part A).
1508	

Table 1: Variable Definition Table

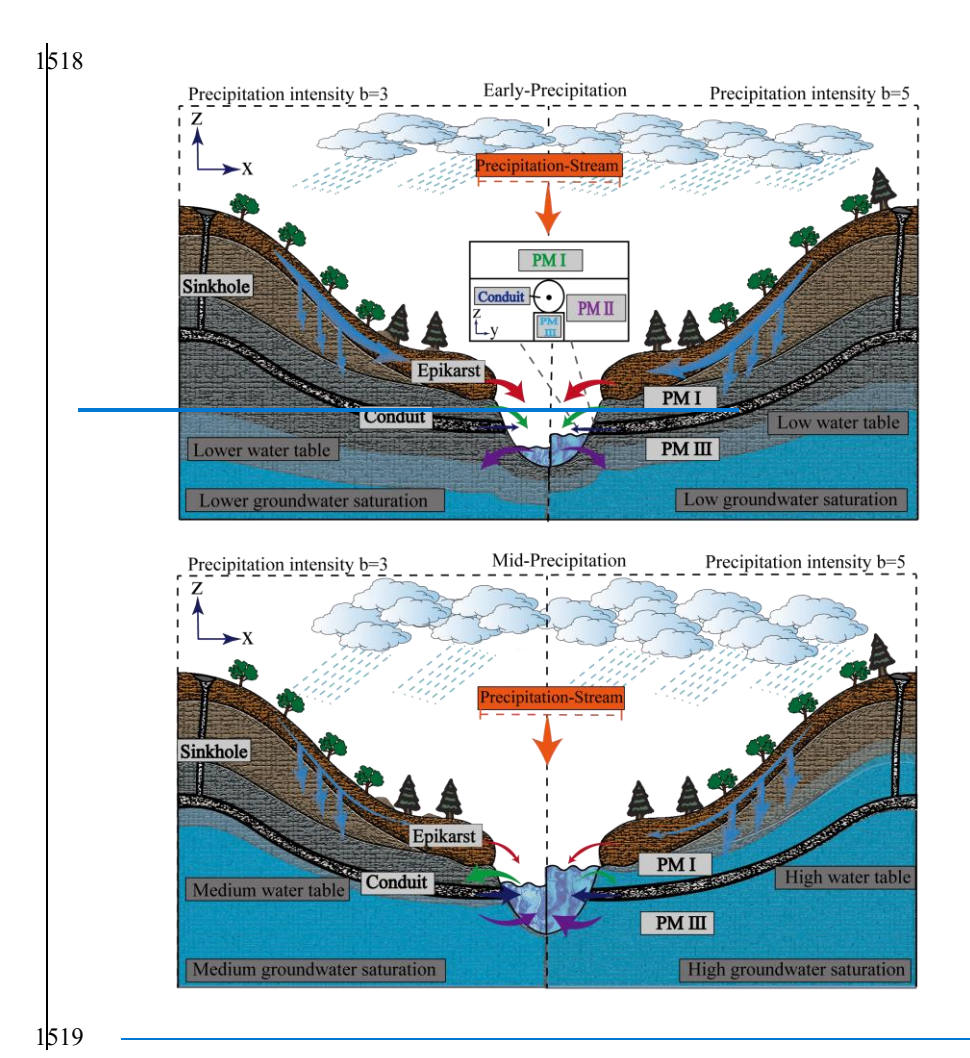
<u>Variable</u>	<b>Description</b>	<u>Unit</u>
φ	Porosity field	
V	Volume of the averaging-volume	$m^3$
$V_l$	Water Volume	$m^3$
$V_g$	Gas Volume	$m^3$
$lpha_l$	Water Saturation	
$\alpha_g$	Gas Saturation	
$\alpha_{l,\mathrm{e}}$	Effective Saturation	
ρ	Average Fluid Density	$kg/m^3$
$ ho_g$	Gas Density	$kg/m^3$
$\rho_l$	Water Density	$kg/m^3$
μ	Viscosity	$Pa \cdot s$
$\mu_g$	Gas Viscosity	$Pa \cdot s$
$\mu_l$	Water Viscosity	$Pa \cdot s$
$\mu_{eff}$	effective viscosity	$Pa \cdot s$
$\overline{v}$	<u>velocity</u>	m/s
$\overline{v_r}$	relative flow rate of the gas phase to the liquid phase	m/s
$v_t$	turbulent velocity vector	m/s
$v_{rt}$	relative velocity of gas-phase and water-phase turbulence	m/s
$oldsymbol{v}_{turb}$	turbulent kinetic viscosity	$m^2/s$
$ar{p}$	<u>pressure</u>	<u>Pa</u>
$p^*$	<u>pressure</u>	<u>Pa</u>
$F_c$	Surface tension force	<u>N</u>
$S_f$	<u>Drag Source Term</u>	$N/m^3$
$\mathcal{C}_{\mu}$	<u>Dimensionless Constant</u>	
$k_t$	Turbulent Kinetic Energy	$m^2/s^2$
ε	<u>Turbulent Dissipation</u>	$m^2/s^3$
$\boldsymbol{k}$	Apparent permeability	$\underline{\mathbf{m}^2}$
$k_0$	Absolute permeability	$\underline{\mathbf{m}^2}$
$k_{rg}$	Gas Relative Permeability	
$k_{rl}$	Water Relative Permeability	
$\boldsymbol{g}$	Gravitational Acceleration	$m/s^2$
X	position vectors in Cartesian	
σ	<u>Interfacial tension</u>	N/m
$p_c$	<u>Capillary pressure</u>	<u>Pa</u>
<u>n</u>	Brooks and Corey Coefficient	
<u>m</u>	Van Genuchten Coefficient	

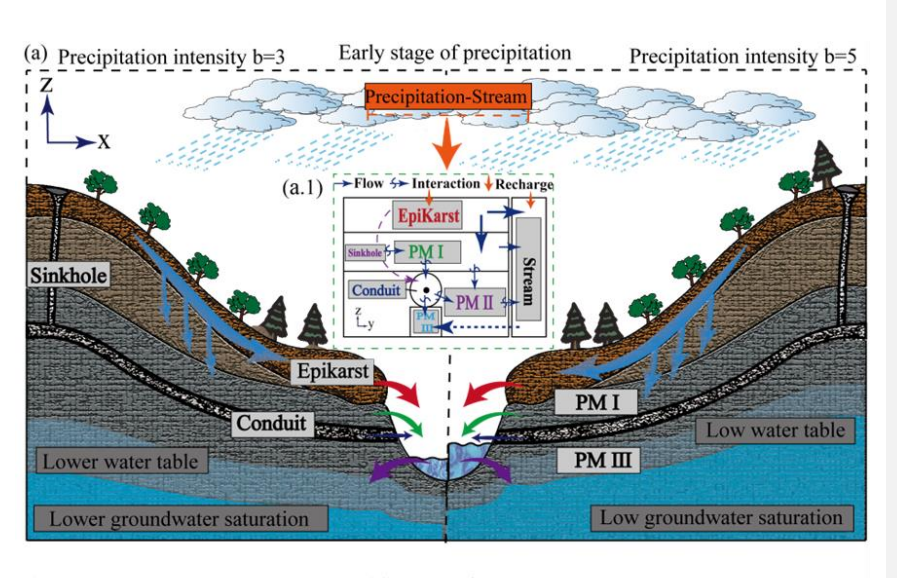
Table 2: Different parameter used in Models

<u>Parameters</u>	<u>Unit</u>	<u>Value</u>
Conduit radius $r_c$	<u>m</u>	0.5
Sinkhole radius $r_s$	<u>m</u>	<u>0.5</u>
Conduit height $h_S$	<u>m</u>	$\frac{0.5}{0.5}$
River width $L_r$	<u>m</u>	<u>2</u> <u>4</u>
EpiKarst thickness	<u>m</u>	<u>4</u>
Porous medium I thickness	<u>m</u>	<u>13</u>
Porous medium II thickness	<u>m</u>	<u>3</u>
Porous medium III thickness	<u>m</u>	<u>3</u> <u>1</u>
Porous medium length $L_{py}$	<u>m</u>	<u>200</u>
Porous media width $L_{px}$	<u>m</u>	<u>200</u>
Gravitational acceleration g	$m/s^2$	9.81
Porous medium Porosity $\varphi$	/	<u>0.4</u>
Porous medium Permeability coefficient $k_0$	$m^2$	$\frac{0.4}{10^{-9}}$
Gas phase viscosity $\mu_a$	$m^2/s$	1.48*10-5
Gas phase density $\rho_a$	$Kg/m^3$	<u>1.29</u>
<u>Liquid phase viscosity</u> $\mu_w$	$m^2/s$	<u>10<sup>-6</sup></u>

Table 3: Comparing DBS and MODFLOW results for key variables

Numerical	Peak Lag Time (s)		Peak Flow $(m^3/s)$			Total Outflow (m <sup>3</sup> )			
Model	b = 3	<i>b</i> = 5	<b>b</b> = 7	b = 3	b = 5	<b>b</b> = 7	b = 3	<i>b</i> = 5	<b>b</b> = 7
DBS Model	3242. 96	1870. 18	<u>2985.</u> <u>31</u>	4.50	12.14	21.96	65984 .49	15415 8.46	27294 5.87
MODFLOW -CFPv2	2 <u>520.</u>	1 <u>920.</u> 00	1860. 00	4.31	11.87	18.87	63916 15	15754 3.65	24551 9.26





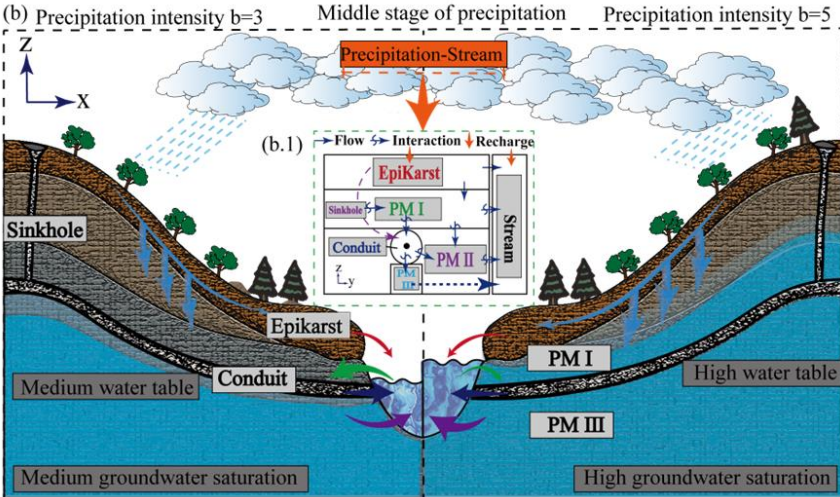


Figure 1. Schematic diagrams of the modelling of the interaction between the karst aquifer (epikarst, sinkhole, sarst conduit, PM | 1, PM | 1, and PM | 11) and stream under dimensionless precipitation intensities (b = 3 and b = 5). (a) and (a.1) Schematic diagram of the interaction flow between each medium and stream in the early stage of a precipitation event; (b) and (b.1) Schematic diagram of the interaction flow between each medium and stream in the middle stage of a precipitation event. The size of the arrows represents the magnitude of the flow rate, and the direction of the arrows represents the direction of interaction between the two.

Formatted: Font: 小五, Bold
Formatted: Justified
Formatted: Font: 小五, Bold
Formatted: Font: 小五, Bold

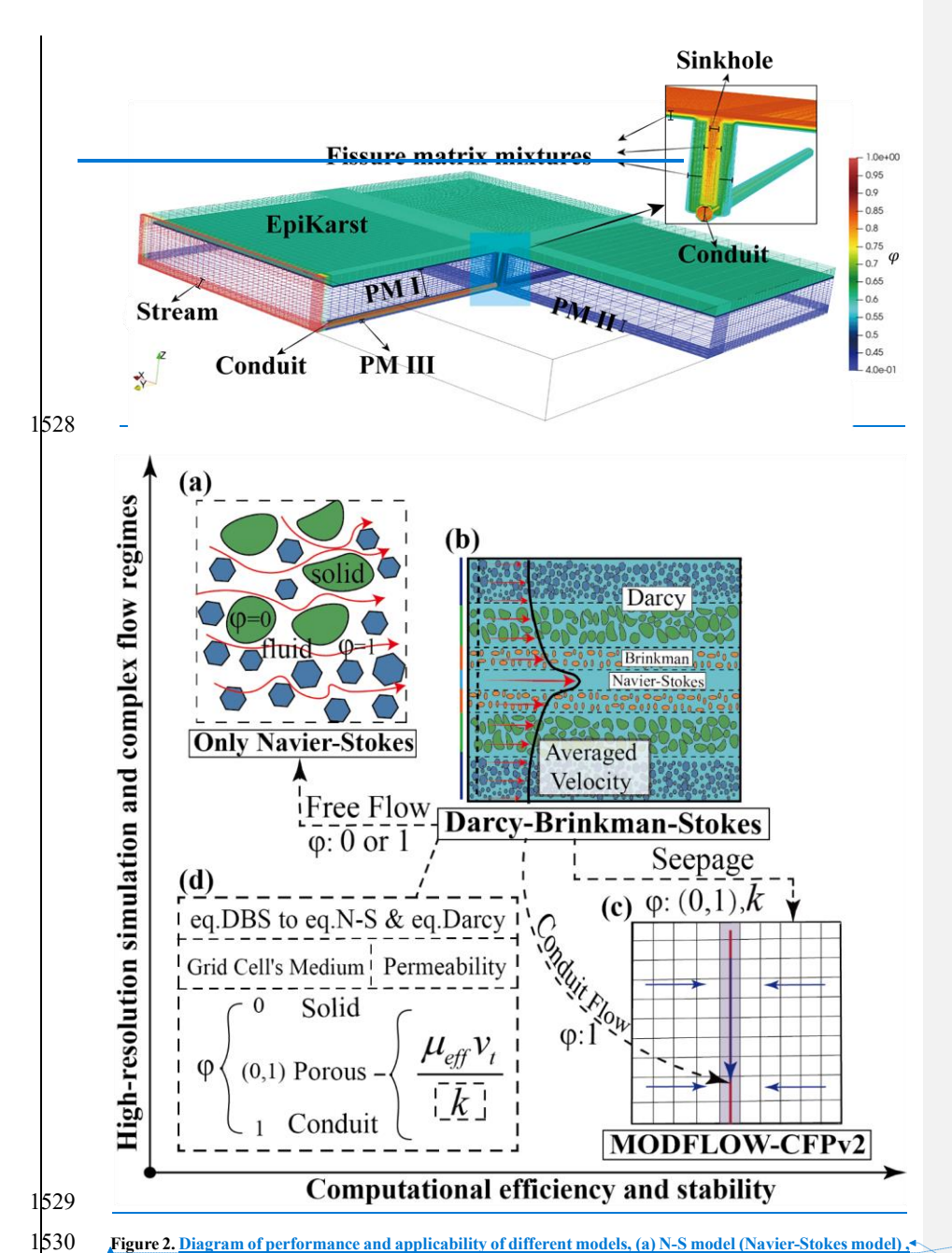


Figure 2. Diagram of performance and applicability of different models, (a) N-S model (Navier-Stokes model), (b) DBS model, (c) Schematic diagram of MODFLOW-CFP model solution, (d) Conversion method from DBS equations to N-S equations and Darcy equations. Discrete scheme for the karst aquifer and stream model,

1532

1533

**Formatted:** Font: 小五, Bold

Formatted: Justified, Indent: First line: 0 ch, Line spacing: single, Widow/Orphan control

Formatted: Default Paragraph Font, Font: (Asian) 黑体, 小五, Bold, Font color: Auto, Pattern: Clear

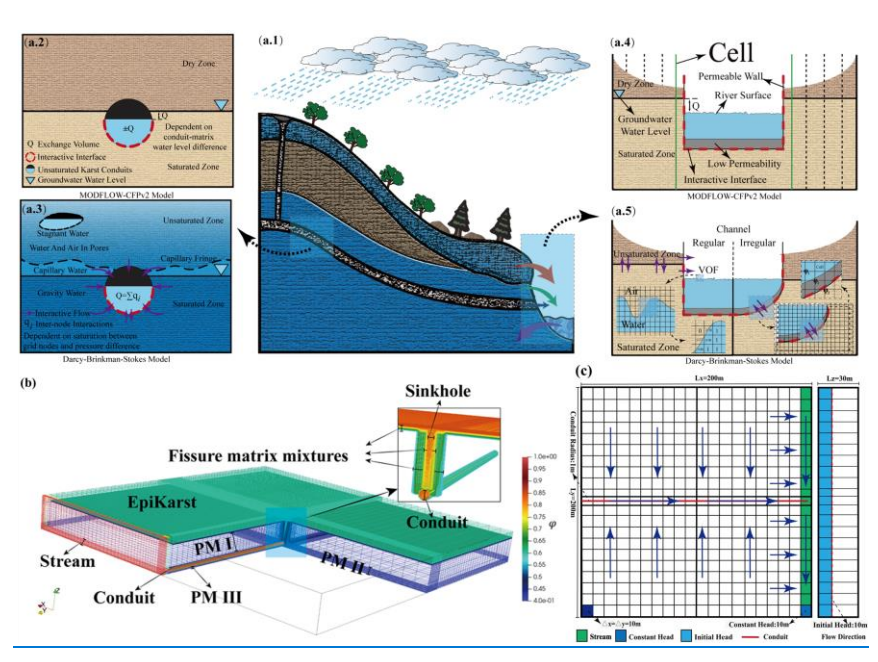


Figure 3. (a) Schematic comparison of conduit and porous media coupling modes between MODFLOW\_CFPv2 and DBS, (b) DBS model and (c) CFPv2 discretization schemes for karst aquifer systems with riverside models,

Formatted: Font: 小五, Bold

Formatted: Justified, Indent: First line: 0 ch, Line spacing: single, Widow/Orphan control

**Formatted:** Default Paragraph Font, Font: (Asian) 黑体,10 pt, Font color: Auto, Pattern: Clear

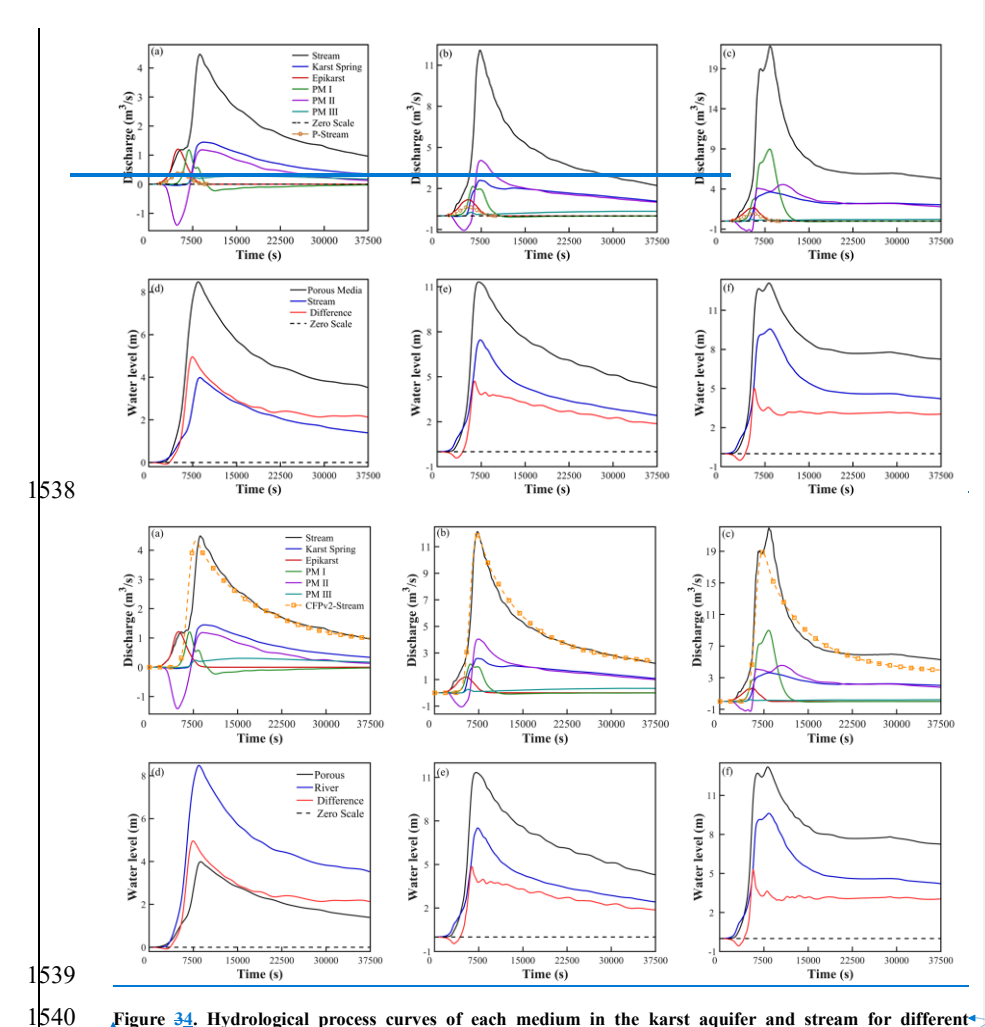


Figure 34. Hydrological process curves of each medium in the karst aquifer and stream for different precipitation intensities: (a)  $b = 3_a$  (b)  $b = 5_a$  (c)  $b = 7_a$  Water level changes and differences in water levels in the karst aquifer and stream for different precipitation intensities: (d)  $b = 3_a$  (e)  $b = 5_a$  (f)  $b = 7_a$ 

Formatted: Font: 小五, Bold

Formatted: Justified

Formatted: Font: 小五

Formatted: Font: 小五, Bold

Formatted: Font: 小五, Bold

Formatted: Font: 小五

Formatted: Default Paragraph Font, Font: (Asian)

黒体, 小五

Bold

Formatted: Default Paragraph Font, Pont: (Asian)

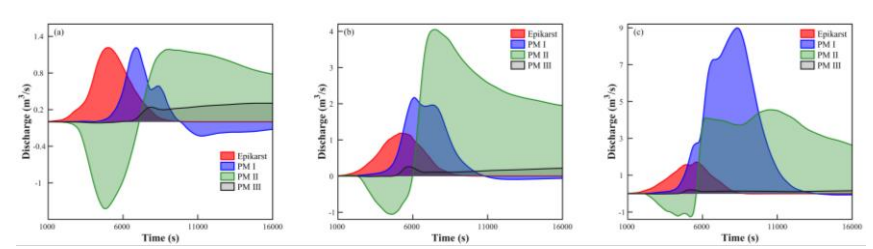
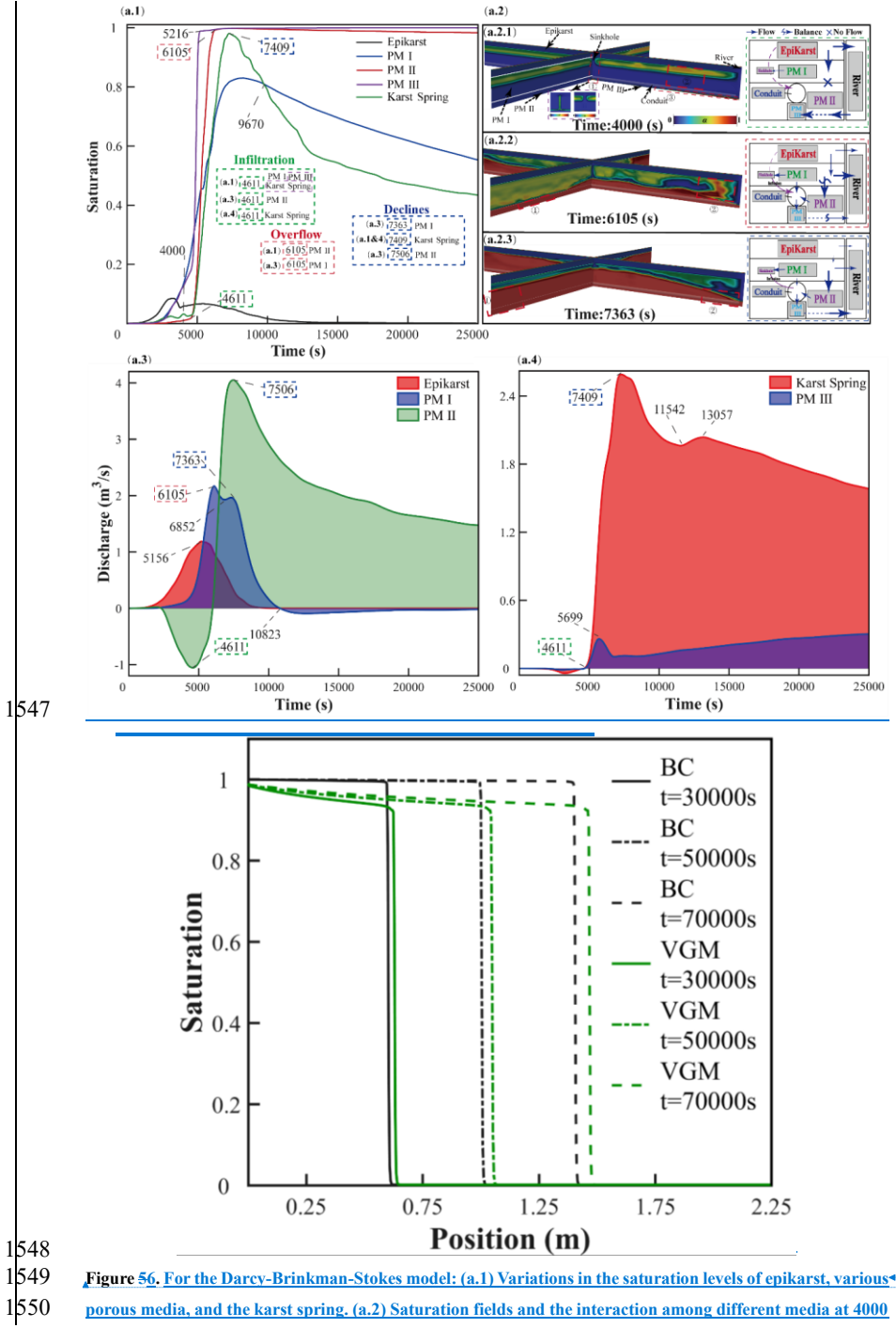


Figure 4Figure 5. Interaction process of epikarst, porous media, and stream for different precipitation intensities: (a)  $b = 3_a$  (b)  $b = 5_a$  (c)  $b = 7_a$ 

Formatted: Font: 小五, Bold
Formatted: Justified
Formatted: Font: 小五
Formatted: Font: 小五, Bold



porous media, and the karst spring. (a.2) Saturation fields and the interaction among different media at 4000

Formatted: Font: 小五, Bold

Formatted: Justified

- 1551 1552 1553 s, 6105 s, and 7363 s. (a.3) Interaction volumes between epikarst, porous media I, II, and the stream. (a.4)
- Interaction volumes among the karst spring, porous media III, and the stream. Water retention curves
- obtained using BC and VGMM water retention equations.

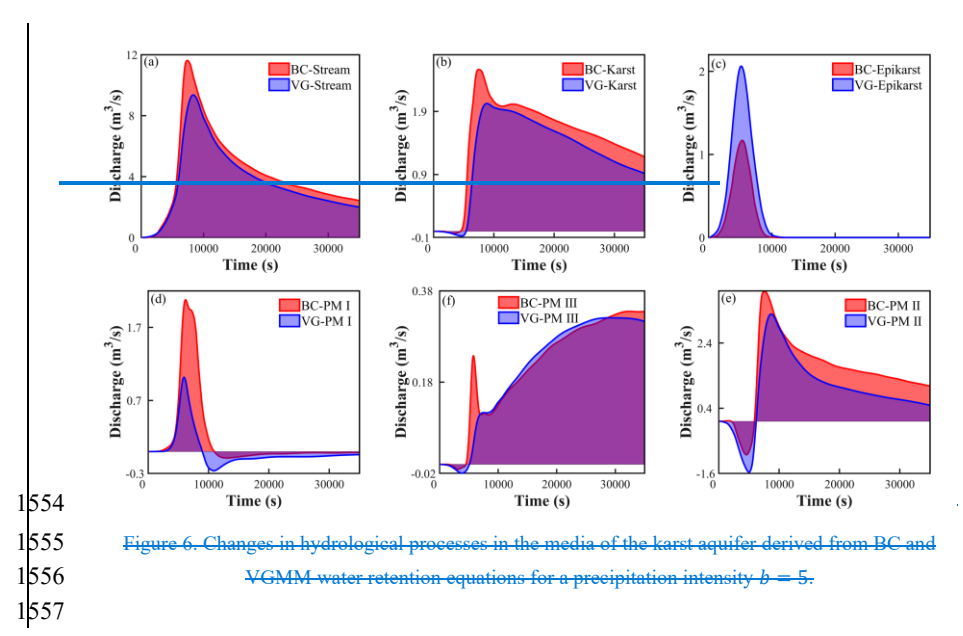


Figure 6. Changes in hydrological processes in the media of the karst aquifer derived from BC and

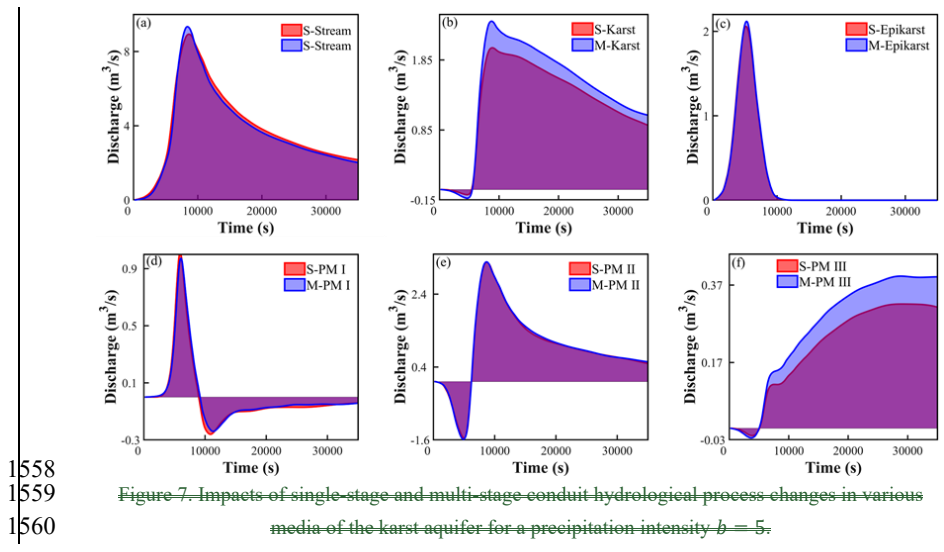


Figure 7. Impacts of single-stage and multi-stage conduit hydrological process-changes in various media of the karst aquifer for a precipitation intensity b = 5.

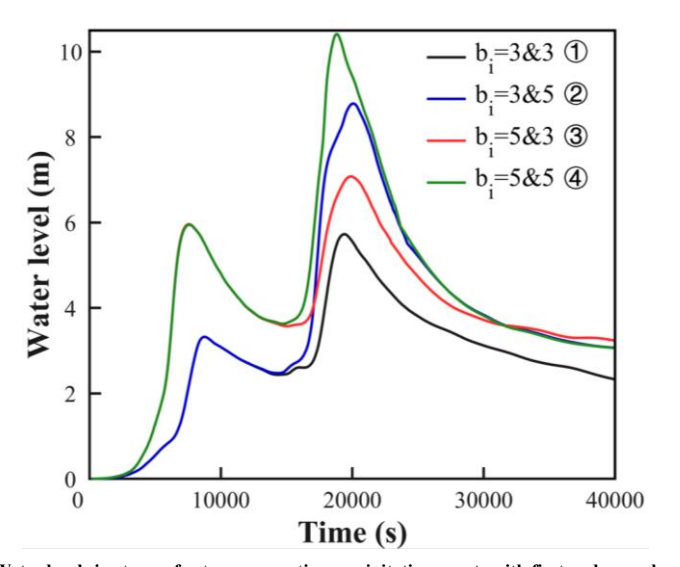


Figure \$7. Water levels in stream for two consecutive precipitation events with first and second precipitation intensities  $\textcircled{0}_{*}b_{1*}=3$  and  $b_{2*}=3$ ;  $\textcircled{2}_{*}b_{1*}=3$  and  $b_{2*}=5$ ;  $\textcircled{3}_{*}b_{1*}=5$  and  $b_{2*}=3$ ;  $\textcircled{4}_{*}b_{1*}=5$  and  $b_{2*}=5$ , respectively,

1562

1563

Formatted: Font: 小五, Bold Formatted: Justified **Formatted:** Font: (Default) Times New Roman, (Asian) 黑体,小五,Bold Formatted: Font: 小五, Bold Formatted: Font: 小五 Formatted: Font: 小五 Formatted: Font: 小五 Formatted: Font: 小五, Bold Formatted: Font: 小五 Formatted: Font: 小五 Formatted: Font: 小五 Formatted: Font: 小五, Bold Formatted: Font: (Default) Times New Roman, (Asian) 黑体,小五,Bold Formatted: Font: 小五, Bold Formatted: Font: 小五 Formatted: Font: 小五 Formatted: Font: 小五 Formatted: Font: 小五, Bold Formatted: Font: 小五 Formatted: Font: 小五 Formatted: Font: 小五 Formatted: Font: 小五, Bold **Formatted:** Font: (Default) Times New Roman, (Asian) 黑体,小五,Bold Formatted: Font: 小五, Bold Formatted: Font: 小五 Formatted: Font: 小五 Formatted: Font: 小五 Formatted: Font: 小五, Bold Formatted: Font: 小五 Formatted: Font: 小五 Formatted: Font: 小五 Formatted: Font: 小五, Bold **Formatted:** Font: (Default) Times New Roman, (Asian) 黑体,小五,Bold Formatted: Font: 小五, Bold Formatted: Font: 小五 Formatted: Font: 小五 Formatted: Font: 小五 Formatted: Font: 小五, Formatted: Font: 小五 Formatted: Font: 小五 Formatted: Font: 小五

Formatted: Font: 小五, Bold

**Formatted:** Default Paragraph Font, Font: (Asian) 黑体, 小五, Bold, Font color: Auto, Pattern: Clear

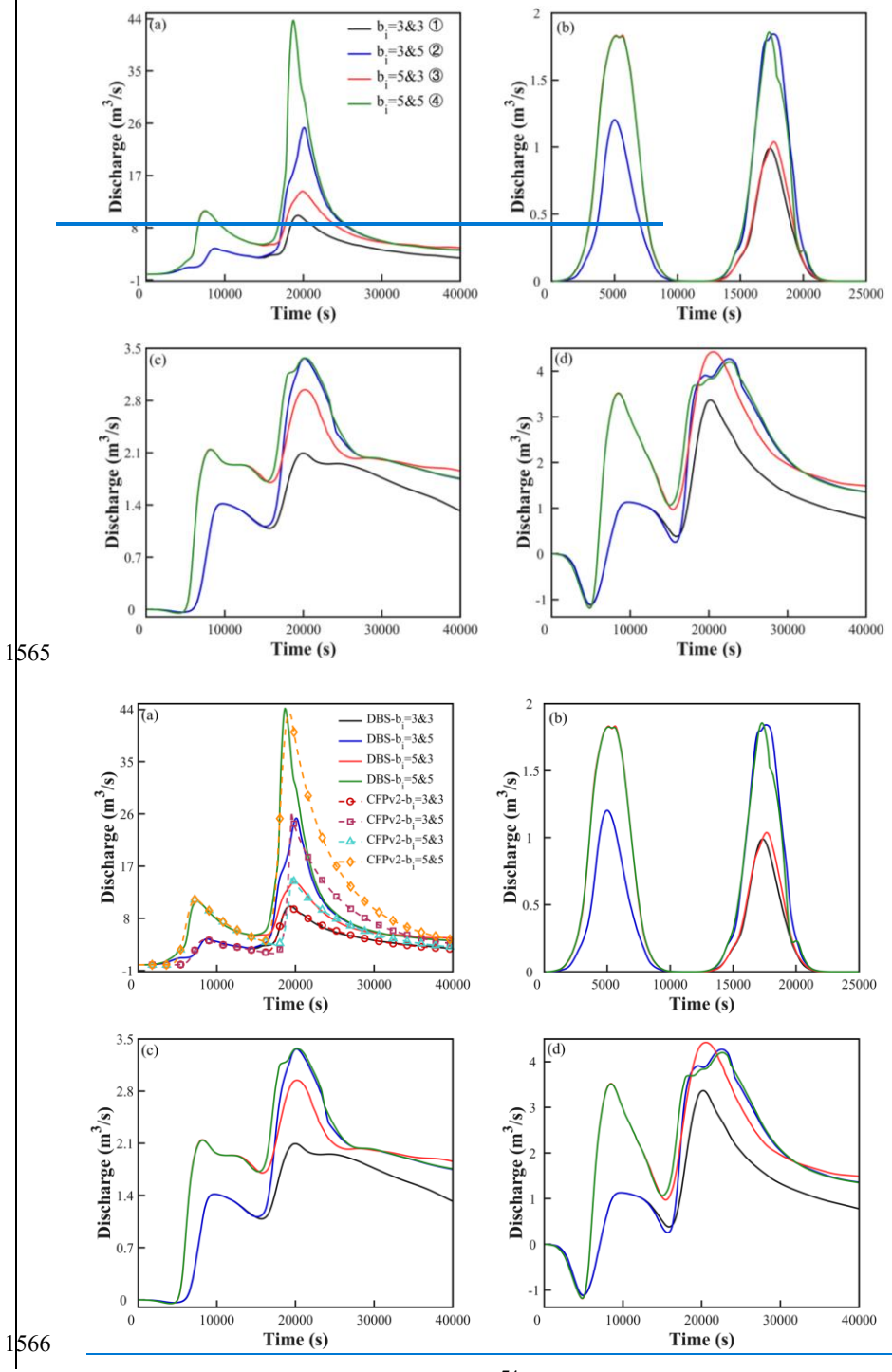


Figure 98. (a) Hydrological process curves of the stream; (b) Discharge process of groundwater through the epikarst to the stream; (c) Discharge process of groundwater through the karst conduit to the stream; (d) Discharge process of porous media (PM II) to the stream, for two consecutive precipitation events with first and second precipitation intensities  $\textcircled{0}_{a}b_{1a} = 3_{a}$  and  $b_{2a} = 3_{b}$  and  $b_{2a} = 5_{b}$  and  $b_{2a} = 5_{b}$  and  $b_{2a} = 5_{b}$  and  $b_{2a} = 5_{b}$  respectively.

1567

1568

1569

1570

Formatted: Font: (Default) Times New Roman, (Asian) 黑体,小五,Bold Formatted: Font: 小五, Bold Formatted: Font: 小五 Formatted: Font: 小五 Formatted: Font: 小五 Formatted: Font: 小五, Bold Formatted: Font: 小五 Formatted: Font: 小五 Formatted: Font: 小五 Formatted: Font: 小五, Bold **Formatted:** Font: (Default) Times New Roman, (Asian) 黑体,小五,Bold Formatted: Font: 小五, Bold Formatted: Font: 小五 Formatted: Font: 小五 Formatted: Font: 小五 Formatted: Font: 小五, Bold Formatted: Font: 小五 Formatted: Font: 小五 Formatted: Font: 小五 Formatted: Font: 小五, Bold Formatted: Font: (Default) Times New Roman, (Asian) 黑体,小五,Bold Formatted: Font: 小五, Bold Formatted: Font: 小五 Formatted: Font: 小五 Formatted: Font: 小五 Formatted: Font: 小五, Bold Formatted: Font: 小五 Formatted: Font: 小五 Formatted: Font: 小五 Formatted: Font: 小五, Bold Formatted: Font: (Default) Times New Roman, (Asian) 黑体, 小五, Bold Formatted: Font: 小五, Bold Formatted: Font: 小五 Formatted: Font: 小五 Formatted: Font: 小五 Formatted: Font: 小五, Bold Formatted: Font: 小五 Formatted: Font: 小五 Formatted: Font: 小五 Formatted: Font: 小五, Bold

Formatted: Font: 小五, Bold

Formatted: Justified

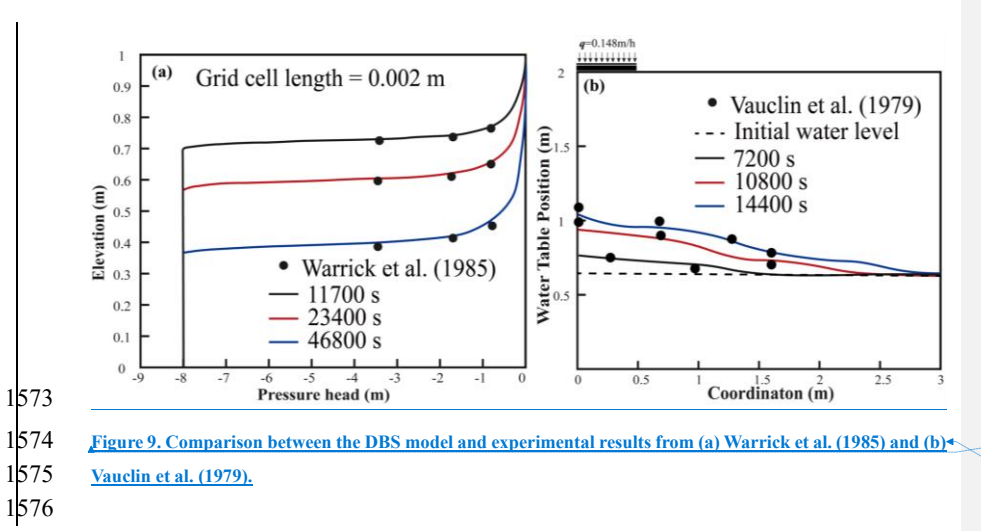


Figure 9. Comparison between the DBS model and experimental results from (a) Warrick et al. (1985) and (b) Vauclin et al. (1979).

Formatted: Font: 小五, Bold

Formatted: Indent: First line: 0 ch, Line spacing: single, Widow/Orphan control

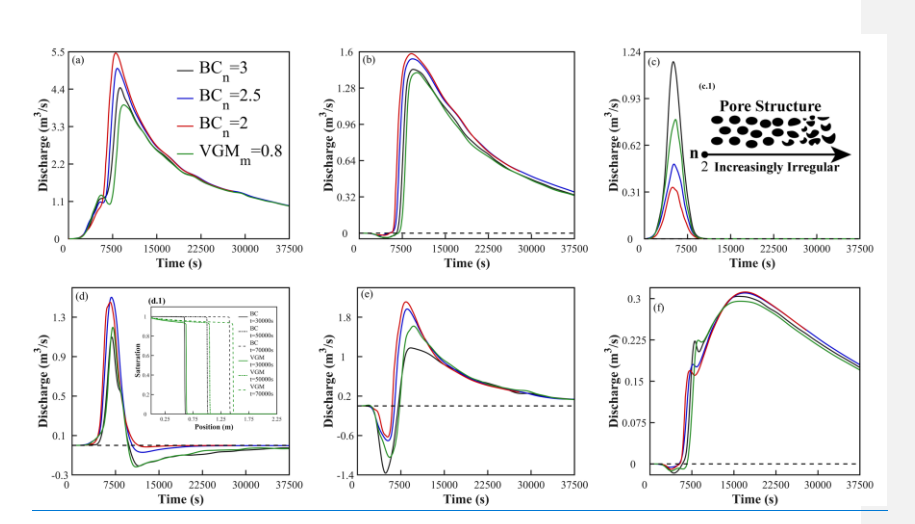


Figure 10. Hydrological process curves under different water retention model parameters (BCn = 3, 2.5, 2 and VGMm = 0.85, 0.8) for (a) stream, (b) karst spring, (c) epikarst, (d) PM I, (e) PM II, and (f) PM III. Subplots (c.1) and (d.1) show the schematic diagram of parameter effects on porous media morphology and the water retention curves of the BC and VGM models, respectively.

 Formatted: Font: 小五, Bold

Formatted: Indent: First line: 0 ch, Line spacing: single, Widow/Orphan control

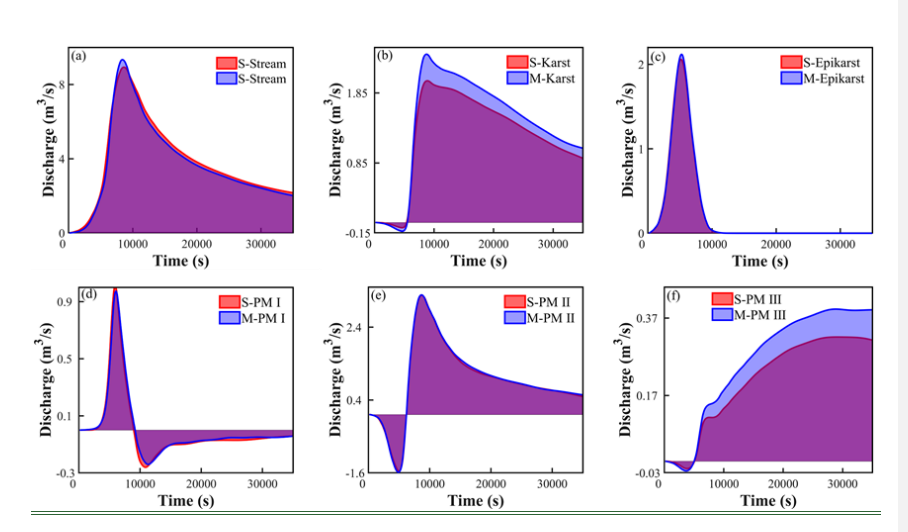


Figure 711. Impacts of single-stage and multi-stage conduit hydrological process changes in various media of the karst aquifer for a precipitation intensity b = 5.

Formatted: Font: 小五, Bold
Formatted: Justified
Formatted: Font: 小五
Formatted: Font: 小五, Bold

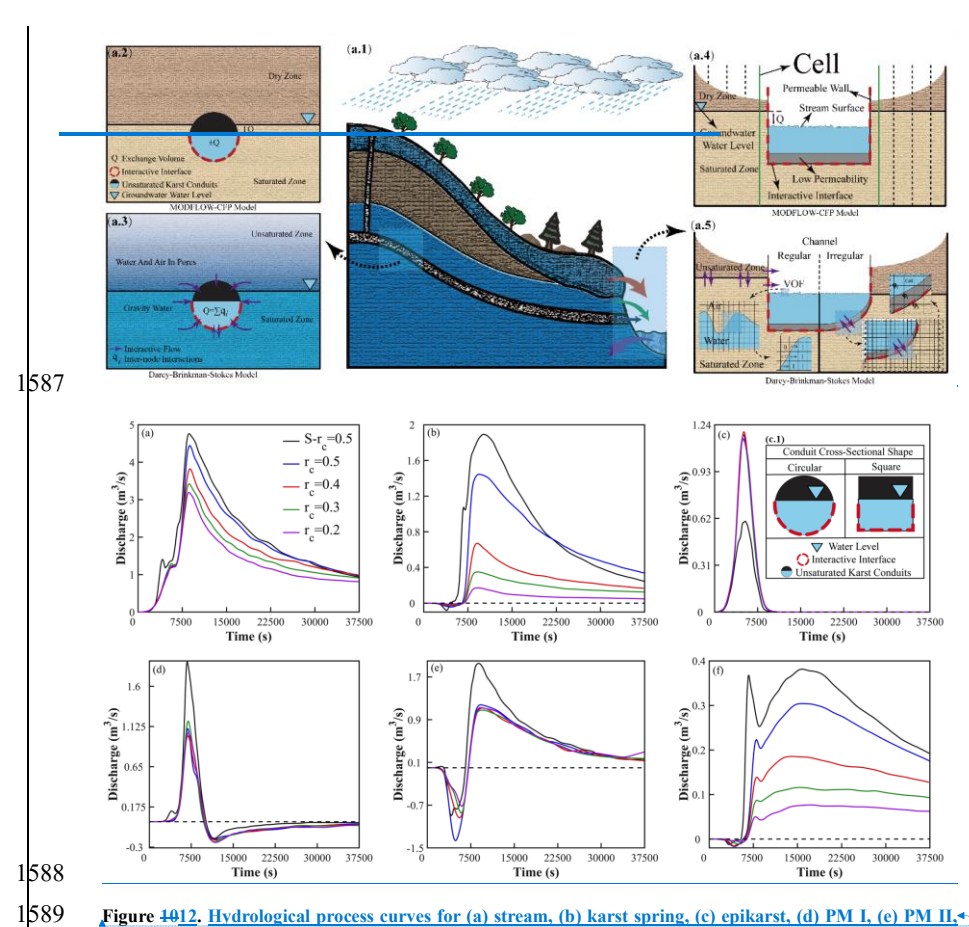


Figure 4012. Hydrological process curves for (a) stream, (b) karst spring, (c) epikarst, (d) PM I, (e) PM II, and (f) PM III under conditions of circular conduits with radii rc = 0.2, 0.3, 0.3, and 0.5, and square-cross-section conduits with S-rc = 0.5. Subplot (c.1) shows a schematic diagram of different conduit cross-sectional shapes.

The differences in the interaction patterns of groundwater between conduit and porous media in (a) the MODFLOW CFP model and (b) the Darcy Brinkman Stokes model.

Formatted: Font: 小五, Bold

Formatted: Indent: First line: 0 ch, Line spacing: single, Widow/Orphan control

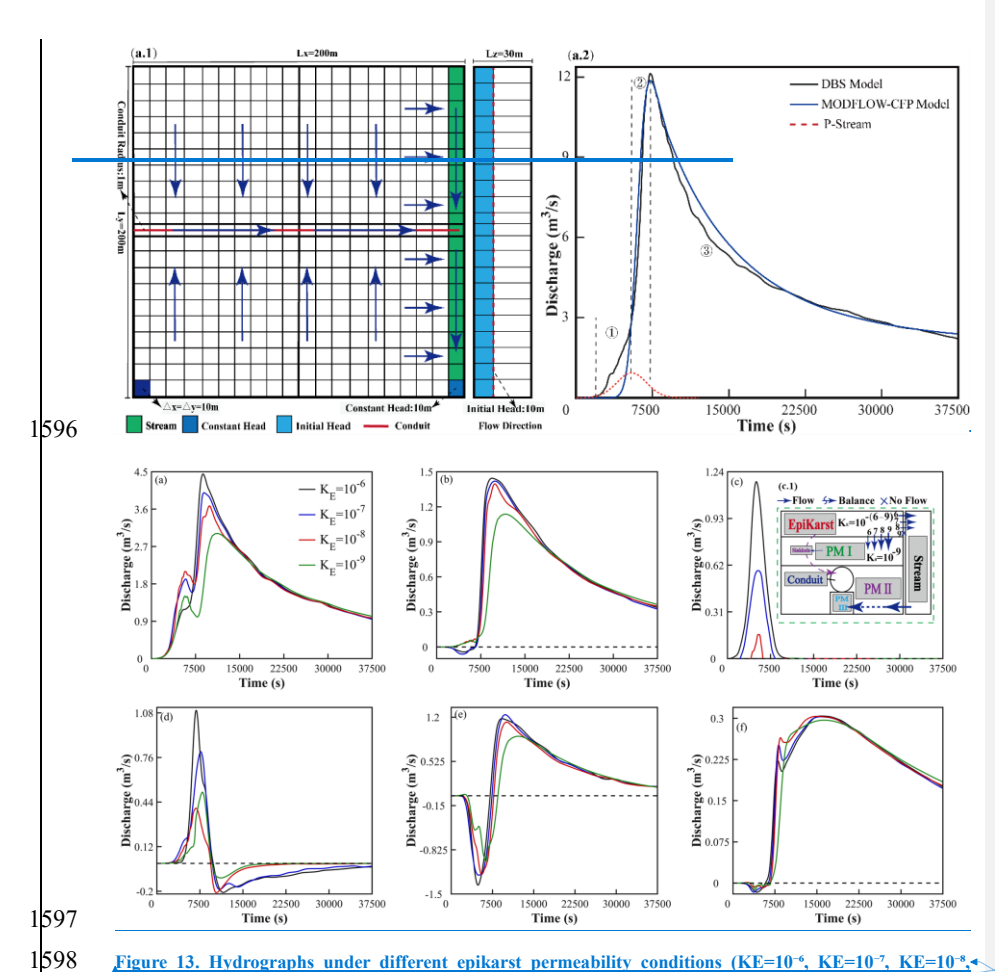


Figure 13. Hydrographs under different epikarst permeability conditions (KE=10-6, KE=10-7, KE=10-8, KE=10-9) for: (a) stream, (b) karst spring, (c) epikarst, (d) PM I, (e) PM II, (f) PM III. Subfigure (c.1) shows a schematic diagram of media interactions under varying epikarst permeability conditions. Figure 11. (a.1) Mesh division of the x-y plane and y-z plane of the MODFLOW-CFP two-dimensional model. (b.1) Comparison of the hydrographs of the stream for the MODFLOW-CFP model and the Darcy-Brinkman-Stokes model under the rainfall boundary condition when b = 5.

Formatted: Font: 小五, Bold

Formatted: Justified

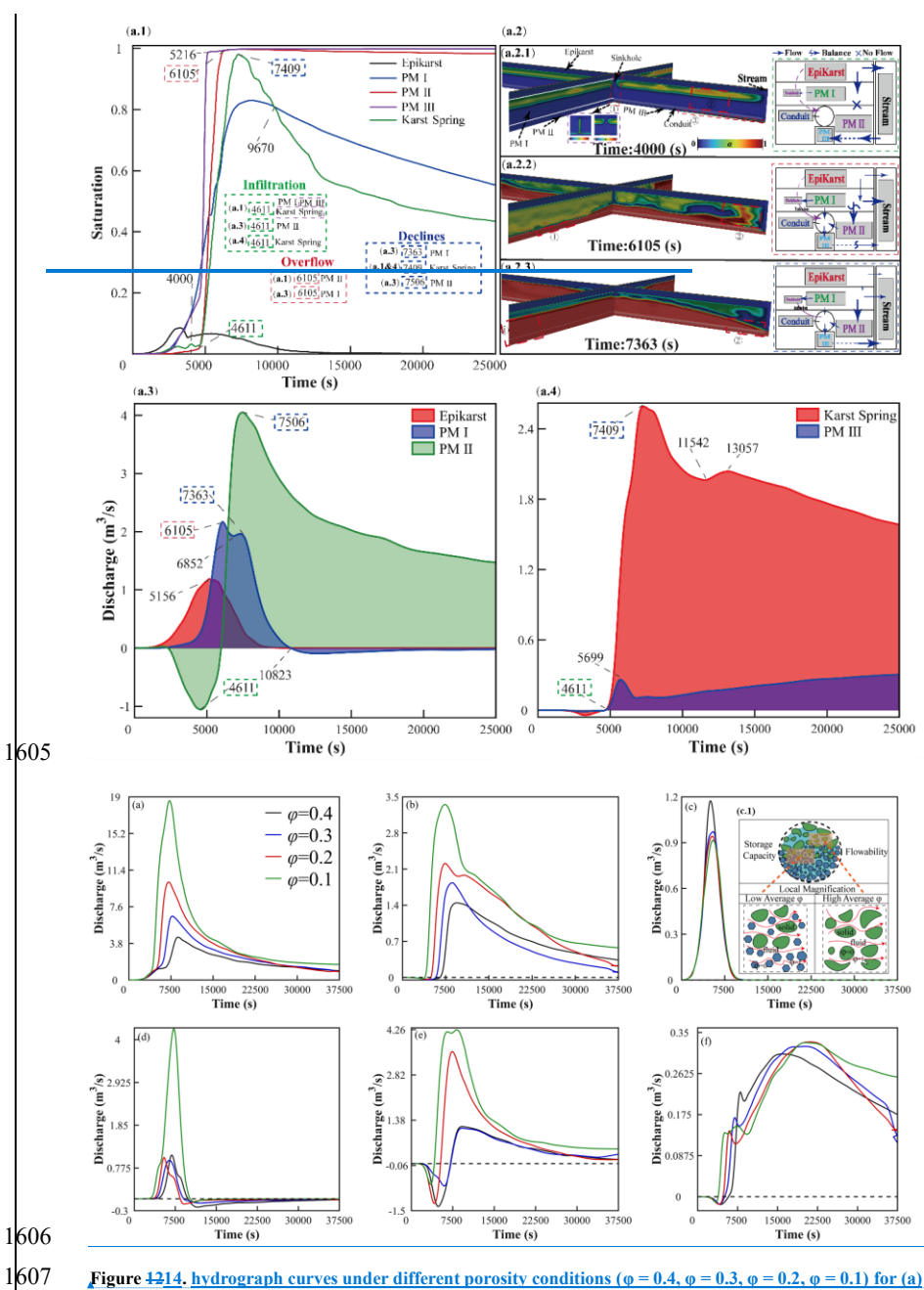


Figure 4214. hydrograph curves under different porosity conditions (φ = 0.4, φ = 0.3, φ = 0.2, φ = 0.1) for (a) stream, (b) karst spring, (c) epikarst, (d) PM II, (e) PM II, and (f) PM III. Among these, (c.1) illustrates a schematic diagram of the medium's water storage capacity and flow capacity under varying porosity conditions. For the Darcy-Brinkman-Stokes model: (a.1) Variations in the saturation levels of epikarst,

Formatted: Font: 小五, Bold

1611	various porous media, and the karst spring. (a.2) Saturation fields and the interaction among different
1612	media at 4000 s, 6105 s, and 7363 s. (a.3) Interaction volumes between epikarst, porous media I, II, and the
1613	stream. (a.4) Interaction volumes among the karst spring, porous media III, and the stream

Formatted: Default Paragraph Font, Font: (Asian) 黑体,小五, Bold, Font color: Auto, Pattern: Clear